ISSN en trámite

# Geofísica Internacional

Revista Trimestral Publicada por el Instituto de Geofísica de la Universidad Nacional Autónoma de México

México
Volume 54 Number 4
October - December
2015

# — Geofísica Internacional —

**GEOFÍSICA INTERNACIONAL**, Año 54, Vol. 54, Núm. 4, octubre - diciembre de 2015 es una publicación trimestral, editada por la Universidad Nacional Autónoma de México, Ciudad Universitaria, Alcaldía Coyoacán, C.P. 04150, Ciudad de México, a través del Instituto de Geofísica, Circuito de la Investigación Científica s/n, Ciudad Universitaria, Alcaldía Coyoacán, C.P. 04150, Ciudad de México, Tel. (55)56 22 41 15. URL: http://revistagi.geofisica.unam.mx, correo electrónico: revistagi@igeofisica.unam.mx. Editora responsable: Andrea Rostan Robledo. Certificado de Reserva de Derechos al uso Exclusivo del Título: 04-2022-081610251200-102, ISSN: en trámite, otorgados por el Instituto Nacional del Derecho de Autor (INDAUTOR). Responsable de la última actualización Saúl Armendáriz Sánchez, Editor Técnico. Fecha de la última modificación: 30 de septiembre 2015, Circuito de la Investigación Científica s/n, Ciudad Universitaria, Alcaldía Coyoacán, C.P. 04150, Ciudad de México.

Geofísica Internacional

Vol. 54, Núm. 4, octubre-diciembre de 2015

## Contents

Surface Energy Balance model for high-altitude glacial system at 19°N on Glaciar Norte, Mexico.
**Guillermo Ontiveros-González, Hugo Delgado-Granados, Jorge Cortés-Ramos**

299

Fractalness of land gravity data and residual isostatic anomalies map of Argentina, Chile and western Uruguay.
**Silvia Alicia Miranda, Alfredo Héctor Herrada, María Cristina Pacino**

315

Chapala half-graben structure inferred. A magnetometric study.
**Miguel Angel Alatorre-Zamora, José Oscar Campos-Enríquez, José Guadalupe Rosas-Elguera, Laura Peña-García, Roberto Maciel-Flores, Emilia Fregoso-Becerra**

323

Surface DC resistivity survey of contamination Beneath Ido-Osun dumpsite, southwestern Nigeria.
**Gabriel Oyelowo Bayowa, Dele Ebenezer Falebita, Raheem Olajide Adegboyesga**

342

Electrical resisitivity to detect zones of biogas accumulation in a landfill.
**César Augusto Moreira, Thais Munhoz, Fernanda Cavallari, Lívia Portes Innocenti Helene**

353

Papanoa, Mexico earthquake of 18 April 2014 (Mw7.3).
**UNAM Seismology Group**

363

Geofísica Internacional (2015) 54-4: 299-314

Original paper

# Surface Energy Balance model for high-altitude glacial system at 19°N on Glaciar Norte, Mexico

Guillermo Ontiveros-González*, Hugo Delgado-Granados and Jorge Cortés-Ramos

Received: June 27, 2013; accepted: August 04, 2015; published on line: October 01, 2015

**Resumen**

Los glaciares de México son pequeños cuerpos de hielo situados en la cima de las montañas más altas de México. Representan un indicador natural para los cambios climáticos en la latitud de 19º norte, donde no hay algún otro cuerpo de hielo en todo el mundo. El Glaciar Norte del Volcán Citlaltépetl, México, ha mostrado un fuerte retroceso igual que otros glaciares cerca de los trópicos. Siguiendo la tendencia actual de los pequeños glaciares de todo el mundo, este glaciar tal vez haya desaparecido antes de mediados de siglo y con esta desaparición se habrá perdido un importante indicador del clima en esta latitud. Por lo tanto, es importante identificar los factores que influyen en el retroceso y eventual desaparición de los glaciares. Este estudio se centra en el análisis de los flujos de energía en la superficie del Glaciar Norte, en el flanco norte del volcán Citlaltépetl, México. A partir de esto, se calcula el balance de energía para un solo punto en la superficie del glaciar. Aquí se describe el estudio glacio-meteorológico realizado a partir de datos de estaciones meteorológicas automáticas instaladas en una elevación >5100 metros y el modelo de balance de energía. Los resultados sugieren que la radiación neta es el principal componente radiativo responsable del retroceso de los glaciares mexicanos ya que este parámetro domina la variabilidad del balance energético. Este comportamiento se comparó con el régimen actual de los glaciares tropicales y de latitudes medias y fue posible establecer una primera aproximación del régimen de este tipo de glaciares basado en la variabilidad del balance energético.

Palabras clave: glaciares mexicanos, balance de energía, flujo radiativo, balance radiativo, régimen climatico.

**Abstract**

The glaciers of Mexico are very small ice bodies located on top of the highest mountains of Mexico. They represent a natural gauge for the climatic changes at the 19ºN latitude where no other ice bodies are located around the world. Glaciar Norte glacier on Citlaltépetl Volcano, Mexico, has been retreating in a huge scale, just like other glaciers close to the tropics. Following the current trend of the small glaciers around the world, this glacier will probably disappear before mid-century and with its disappearance an important climatic gauge at this latitude will be gone. Therefore, it is important to identify the factors influencing the retreat and eventual demise of the glaciers. This study focuses on the analysis of the energy fluxes of Glaciar Norte's surface on the northern flank of Citlaltépetl Volcano, Mexico. From this, it was calculated the energy balance for a single point on the glacier surface. Here, the glacio-meteorological study is described using data from automatic weather stations installed at >5100 masl with the energy balance model developed from this data. The results suggest that net radiation is the main component responsible for the retreat of Mexican glaciers since this parameter controls the energy balance variability. This situation was compared to the energy balance regime present on other tropical and mid-latitude glaciers and it was possible to establish a first approximation of the energy balance regime on glaciers near 19N latitude based on energy balance variability.

Key words: Mexican glaciers, energy balance, radiative fluxes, radiative balance, climate regime.

G. Ontiveros-González*
H. Delgado-Granados
J. Cortés-Ramos
Departamento de Vulcanología
Instituto de Geofísica
Universidad Nacional Autónoma de México
Ciudad Universitaria
Delegación Coyoacán, 04510
México D.F. México
*Corresponding autor: dremo@geofisica.unam.mx*

**Symbols Table**

$B$ surface energy balance
$R$ net radiation
$H$ turbulent sensible heat flux
$L_v E$ turbulent latent heat flux
$L_f P'$ heat flux from precipitation
$S\downarrow$ incoming shortwave radiative heat flux
$S\uparrow$ outcoming shortwave radiative heat flux
$L\downarrow$ incoming longwave radiative heat flux
$L\uparrow$ outcoming longwave radiative heat flux
$\alpha$ surface albedo

$$H_0 = \rho_a C_{pd} \left( \overline{\omega\, \theta}_v \right)_v$$

$\left( \overline{\omega\, \theta}_v \right)_v$ sensible heat flux through mechanic turbulence
$\theta'_v$ turbulent fluctuation of the virtual potential temperature
$\rho_a$ air density
$C_{pd}$ heat capacity of dry air
$K_h$ Eddy Heat Diffusivity coefficient
$\rho$ represents the air density
$c_p$ the specific heat capacity at constant pressure
$K = K_\omega\, \partial m/\partial z$ vertical flux of water vapor
$L_v$ is the specific sensible heat of evaporation
$K_\omega$ is the eddy diffusivity of water vapor
$m$ mass per unit volume of water vapor
$L_f$ represents the specific latent heat of melting
$\phi$ precipitation rate
$M_\omega$ molecular weight of water
$e$ pressure of water vapor in the atmosphere
$e_s$ saturation vapor pressure
$Ts$
$T$ air temperature
$T_s$ saturation temperature
$P$ air pressure
$M_a$ air molecular weight
$\rho$ the air density
$\tau$ shear stress of dry air on the surface
$u$ wind speed at height
$z_0$ surface roughness
$k_0$ Von Karman constant

**Introduction**

The retreat of Mexican glaciers is so strong that they could be gone before mid-century (Delgado-Granados, 2007). The glaciers at the summit of Popocatépetl have largely melted prior to late year 2000, forced by climatological conditions and accelerated by eruptions (Delgado-Granados *et al*., 2007). The glaciers that still exist on top of Iztaccíhuatl and Citlaltépetl volcanoes are shrinking quickly in spite of dormant volcanic conditions.

These Mexican glaciers at 19ºN, are special because they are some of the last tropical climate indicators in this high elevation zone that still exist around the world. So it is very important to know the main factors influencing their retreat and projected eventual demise. In this sense, the effect of radiative fluxes on the energy balance and resulting glacier retreat had not been studied, so, the only parameters published in the literature related to this glacial retreat were temperature and precipitation. Considering that its position in reference to astronomical tropics, Mexican Glaciers receive solar radiation of the same way that tropical glaciers do, but doesn't have the same variability in precipitation and temperature. These parameters and their relationship to energy balance across the glacial surface play an important role in the variability of accumulation and ablation on the glacier. This means that the retreat of glaciers at 19ºN latitude is determined not only by the annual variability of temperature and precipitation, but also strongly determined by the energy balance and radiative fluxes involved.

Glaciar Norte, on the northern flank of Citlaltépetl volcano, is the largest ice body of Mexico, although its extension has been reduced noticeably. The current volcanic activity of Citlaltépetl is not relevant as compared to Popocatépetl, but slight fumarolic activity is ongoing close to the summit. On the other hand, Citlaltépetl volcano is located distant from any large city or industrial center (it lies 200 km east of Mexico City, 100 km west of Veracruz; Figure 1) and thus, has the lowest anthropogenic influence of all Mexican glaciers. Thus, changes in Glaciar Norte most likely reflect changes in the climatic conditions (Delgado-Granados *et al*., 2007) and not recent volcanism or local air pollution sources.

There might be several meteorological variables influencing the retreat of Glaciar Norte at Citlaltépetl volcano. They can be revealed by: a) instrumentation devoted to

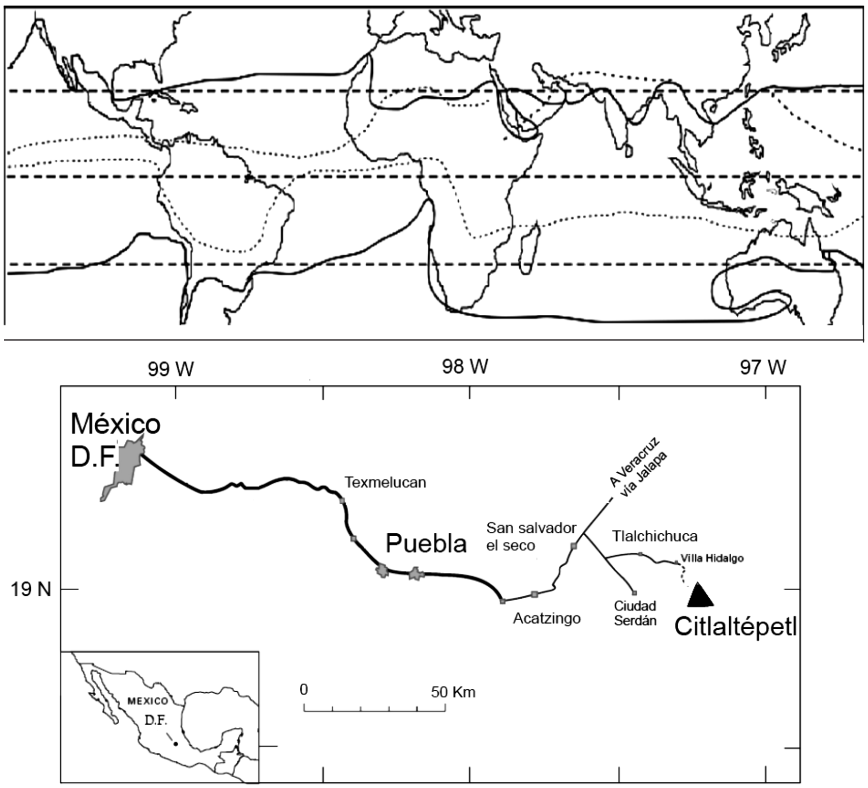


**Figure 1.** Geographic position of the Intertropical Convergence Zone (ITCZ). Modified from Kaser and Osmaston [2002]. In the figure below it is shown the volcano position respect to Mexico City.

continuous data collection in the field; b) a systematic meteorological record for the glaciated area over an extended period of time; and c) calculation of the energy balance over the surface of the glacier according to a theoretical model applied to the meteorological conditions of Glaciar Norte.

This study focuses on Citlaltépetl Volcano because it has no significant current volcanic activity and the least anthropogenic influence in the region. It is believed that the changes shown by Glaciar Norte are mainly due to climatic factors (Delgado-Granados, 2007). Then, using data acquired during 2006 to 2009 from two automatic weather stations which were installed at >5,000 masl, we demonstrate, for the first time, that net radiation is playing an important role in the demise of Mexican glaciers, because it is moderating the surface energy balance.

After this analysis it was possible to compare the behavior of surface energy exchanges on the surface of this glacier located at 19°N latitude to those of tropical glaciers, that is, those glaciers whose annual temperature variability equals the daily temperature variability, receive rainfall throughout the year and are within the astronomical tropics (spanning between 23° 26′ N and 23° 26′ S latitudes as defined by the apparent north-south journey of the sun).

This is important because Mexican glaciers do not have all the characteristics expected for tropical glaciers lying beneath the annual range of the Inter-tropical Convergence Zone (ITCZ). The discussion about similarities and differences between tropical snow and ice systems begins a new research topic on glaciers located at this latitude.

## Meteorological Data

Two controlling seasons were recognized at Popocatépetl volcano: the wet season, with dominance of accumulation, and the dry season, with dominance of ablation (Delgado-Granados *et al*., 2007). Summer is the rainy season (starting in May-June), characterized by precipitation of snow and hail. Snow can last until January-February before the ablation produces *penitents* (see for example Betterton, 2001), however, these conditions present at Popocatépetl are similar at Citlaltépetl region as shown by our data.

On September 17, 2006, two Automatic Weather Stations (AWS) began operating. One was located on the surface of Glaciar Norte (Glaciar station) at 5131 masl, and another on the lateral moraine close to the glacier at 5115 masl (Morrena station). Glaciar station was the main provider of meteorological data used in the energy balance model.

The AWS consists of temperature sensors (accuracy, ±0.5°C), a relative humidity probe (accuracy, ±5%), sensors for wind speed (accuracy, ±0.5) and direction (R.M. Young 03001-5 Wind Sentry Set), a digital barometer (accuracy, ±0.2hPa), and a NR Lite Net Radiometer (error, 3%). Daily averages of each parameter automatically calculated by the station's internal program from September 17, 2006 to October 15, 2009 are presented.

This AWS instrumentation doesn't allow obtaining the energy balance components' absolute values. However, for this study, the net radiation is compared with other data in order to recognize the main processes governing the ablation on the glacier surface.

The total radiative component was measured in the field by two sensors at Glaciar station, placed horizontally above the glacial surface. The sensor facing upwards measured the incoming direct and diffuse solar radiation, whereas the other one was facing downwards aimed towards the glacier surface. The downward aimed radiometer measured the reflected, emitted and diffused outgoing radiation. All the components were summarized in a single exiting signal: the net radiation on the glacial surface.

During times when observed wind speed was seemingly zero, these periods corresponded to low temperatures and a characteristic low valued wind direction, and thus one can interpret the data during these periods. Occasionally, some sensors were frozen, especially the moving parts of the vane and anemometer. During these periods, missing data were replaced by averages from nearby months.

No relevant gaps are present in the data, as the automatic weather station worked correctly since the startup date. However, some data gaps were replaced using daily averages and thus formed a three-year energy balance record to describe the behavior and variations of the energy balance during that period.

## The energy balance model

A theoretical model has been developed for this study based on previous work (Paterson, 1994; Oerlemans, 2001; Francou and Puoyaud, 2004). This model considers the glacier as an adiabatic thermodynamic system, marking an exception in the glacier-atmosphere interface where diabatic processes do occur. The equations for heat flow and water phase change (ice to liquid to vapor for instance) must take into consideration the atmosphere as a fluid or a system composed of gases.

The measured meteorological variables (temperature, solar radiation, humidity, precipitation, wind and atmospheric pressure) at the glacier fed the theoretical model. The model allowed estimating the energy exchange at the glacier-atmosphere interface at Glaciar Norte using the data obtained from the instrumentation already mentioned. The energy balance was estimated with an independent calculation of each component (latent heat, sensible heat and net radiation). The energy balance for the surface of Glaciar Norte could be approximated as:

$$B = R + H + LvE + Lf\phi... \qquad (1)$$

where $R$ is the net radiation, $H$ and $L_vE$ are the turbulent sensible heat flux and the turbulent latent flux respectively, $L_f\phi$ is the heat flux from precipitation, and $B$ is the total energy flux over the surface. The energy supplied by rain is assumed negligible because the glacial surface remains at melting point, but it could be significant when rain freezes on the surface (Paterson, 1994). We follow the convention to consider all fluxes towards the glacial surface as positive, while all fluxes away from the glacial surface are negative. When the surface temperature is ~0°C and the energy balance ($B$) is positive, melting processes are considered as natural processes on the glacial surface.

*Net Radiation*

The total radiative flux is the sum of the net short-wave radiation and net long-wave radiation coming from Earth and sun's emissions. Since net short-wave and long-wave radiation can be separated into incoming and outgoing radiation, the net radiation energy can be expressed by:

$$R = S\downarrow - S\uparrow + L\downarrow - L\uparrow = S\downarrow(1-\alpha) + L\downarrow - L\uparrow ... \qquad (2)$$

where $S\downarrow$ is the incoming short-wave radiation or incoming solar radiation, while $S\uparrow$ is the outgoing short-wave radiation (reflected by the Earth's surface), $L\downarrow$ is the incoming long-wave radiation emitted by the sun and the atmosphere toward the Earth's surface, $L\uparrow$ is the outgoing long-wave radiation emitted by the surface, and $\alpha$ is the surface albedo of the glacier. The net radiation measured at some point on the surface represents by itself an

energy balance of the surface in which this is measured (Francou and Pouyaud, 2004).

*The turbulent heat fluxes*

The water vapor transfer in a glacier is associated with the release and absorption of latent heat that dominates the water evaporation and condensation over the glacier.

On the other hand, the transport of sensible heat between the atmosphere and the glacier's surface is mainly through mechanic or thermal turbulence. The component of the vertical sensible heat flux can be expressed as $H_0 = \rho_a C_{pd}\left(\overline{\omega\,\theta}_v\right)_v$ where $\left(\overline{\omega\,\theta}_v\right)_v$ represents the sensible heat flux through mechanic turbulence with $\theta'_v$ being the turbulent fluctuation of the virtual potential temperature, while $\rho_a$ represents the air density and $C_{pd}$ the heat capacity of dry air (Singh and Singh, 2001).

The heat transferred by convection can be treated as conduction, so $H$ can be expressed in terms of the temperature lapse rate and as "Eddy Heat Diffusivity" ($K_h$) coefficient:

$$H = K_h \rho c_p \frac{\partial T}{\partial z} \ldots \quad (3)$$

here, $\rho$ represents the air density and $c_p$ the specific heat capacity at constant pressure. Therefore, the convective energy by the heat flux of the water vapor and the flux transferred by the precipitation are summed up to calculate the convective energy $H$, hence obtaining the total energy fluxes (Paterson, 1994). The vertical flux of water vapor is given by $E = -K_\omega \partial m/\partial z$. So, the heat flux associated to water vapor flux is:

$$L_v E = -L_v K_\omega \frac{\partial m}{\partial z} \ldots \quad (4)$$

where $L_v$ is the specific sensible heat of evaporation, $K_\omega$ is the eddy diffusivity of water vapor, and $m$ the mass per unit volume of water vapor. Finally, $L_f \phi$ is the precipitation, i.e. the vertical flux of water, while $L_f$ represents the specific latent heat of melting and $\phi$ as the precipitation rate. As stated above, the energy supplied by rain is negligible when the surface and the air temperatures are near the melting point.

*Meteorological parameterization*

The equation of state for moist air as an ideal gas is:

$$\frac{eM_\omega}{m} = RT \ldots \quad (5)$$

where $M_\omega$ is the molecular weight of water, $e$ is the pressure of water vapor in the atmosphere; while for dry air, it is given by:

$$\frac{PM_a}{\rho} = RT \ldots \quad (6)$$

with $P$ representing the air pressure, $M_a$ the air molecular weight and $\rho$ the air density. Such that, $m = \rho e M_\omega / P M_a = (0.622)\,\rho e/P$ where $\frac{M_\omega}{M_a} = (0.622)$. Substituting in equation (4) where $m$ is derived just partially respect to z because the change in other direction can be neglected and the interest in focused on the vertical direction. The result is:

$$L_v E = -LvK\omega(0.622)\frac{\rho}{P}\frac{\partial e}{\partial z} \ldots \quad (7)$$

The heat transfer by convection depends on air turbulence and it is measured through the eddy viscosity $K_m$, which means that, $\tau = K_m \rho \partial u/\partial z$, where $\tau$ is the shear stress of dry air on the surface and $u$ is the wind speed at height $z$, this equation represents the vertical flux of horizontal momentum. There is evidence, that at some height, the coefficients $K_m$, $K_h$ and $K_\omega$ are approximately equal to those of a neutral atmosphere (Paterson, 1994). Although this is possible only if the wind speed, temperature and water pressure are distributed logarithmically with height. This rule described by Paterson (1994) is also applied if the meteorological observations are within ~2m of the surface, and the surface is at melting point. Since these energy balance measurements were taken within the first 2m above the glacier surface, then this rule should apply over the melting surfaces studied here. Thus, it is assumed that: $K_m$ could replace $K_h$ and $K_\omega$. Finally, considering that $\tau$ does not change with height,

$$Km\frac{\partial u}{\partial z} = \frac{\tau}{\rho} = u_*^2 = CONSTANT \ldots \quad (8)$$

while $u_*$ represents the frictional velocity. This frictional velocity is related to the surface roughness ($z_0$), determined by two wind speed measurements at two different heights. Thus, $u_*$ and $z_0$ for neutral atmospheres can be expressed as:

$$\frac{u}{u_*} = \frac{1}{k_0} 1n \quad \frac{z}{z_0} \quad ... \tag{9}$$

$$Km \frac{\partial u}{\partial z} = \frac{\tau}{\rho} = u_*^2 = CONSTANT ... \tag{10}$$

in which $k_0$ is the Von Karman constant, in this case (0.4); $u_1$ is the wind speed at Morrena station, and $u_2$ is the wind speed at Glaciar station; $z_1$ = 1.5 m and $z_2$ = 16.5 m. Using the wind speed measured at both automatic weather stations to calculate $z_0$, then the frictional velocity ranges between 0 and 0.65 m/s, the latter value corresponds to the extreme case of Max wind speeds recorded in both weather stations. This value is higher than usual values for glacial surfaces of which the melting point is usually $k_0 \approx 0.1$ to 0.5 (Kuhn, 1979) due to the high exposure to wind that represents the topography of the glacier. Equation (9) leads to $\partial u/\partial z = u_*/k_0 z$. Inserting this result into equation (8) we obtain the expression, $K_m = u_*/k_0 z$, which can be written $K_m = K_h = K_\omega = u_*/k_0 z$. Then by substituting this with the expression $\rho = \rho_0(\mathrm{P}/\mathrm{P}_0)$obtained from the state equation of ideal gases at height $z$ and $z_0$, the resulting equation is:

$$H = c_p \rho_0 \frac{P}{P_0} u_* k_0 z \frac{\partial T}{\partial z}$$

and after integrating is obtained:

$$H = c_p \rho_0 \frac{P}{P_0} u_* k_0 \frac{T - Ts}{1n(z / z_0)} \qquad ()$$

and by substituting of (9) the final expression is:

$$H = c_p \rho_0 \frac{P}{P_0} u k_0^2 \frac{T - Ts}{1n^2(z / z_0)} ... \tag{11}$$

The equation (12) is obtained through a similar process

$$-L_v E = L_v \frac{\rho_0}{P_0} (0.622) u k_0^2 \frac{e - e_s}{1n^2(z / z_0)} ... \tag{12}$$

if the transfer coefficient is defined as:

$$C^* = \frac{k_0^2}{1n^2(z / z_0)} ... \tag{13}$$

The value of $C^*$ wills depend on measurement height and surface roughness, however previous studies have shown that the parameter depends mainly on the vertical distribution of wind speed (Paterson, 1994). Applying the acquired data sets for the wind speed at the glacial surface, it is possible to calculate the $z_0$ and $C^*$ respectively, and this yielded an average value for $C^*$ equal to 0.0017. For this study, the numerical constant values given in Paterson (1994) are used: $\rho_0$ = 1.29 $\mathrm{kgm}^{-3}$ is the corresponding normal value for air density at 0°C, measured at a sea level pressure of $P_0$ = 1.013 x $10^5$ Pa. These density and pressure values are used because they are a good reference for the ideal gases state equation. The heat capacity of air is $c_p$ = $1010 \mathrm{Jkg}^{-1}\mathrm{K}^{-1}$ at these pressure conditions, and the latent heat of water vaporization of water is $L_v$ = 2260 x $10^3$ J/kg. After substitution, the resulting equation yields:

$$H = (1.29 \text{ x } 10^{-2}) C^* P u (T - T_S) ... \tag{14}$$

$$-L_v E = 22.2 C^* u (e - e_S) ... \tag{15}$$

At this point, it is possible to reformulate the general equation (1):

$$\begin{aligned} \mathrm{B} = \mathrm{R} + &(1.29\mathrm{x}10^{-2}) C^* P u (T - T_S) \\ &+ 22.2 C^* u (e - e_S) + \mathrm{L} f \phi ... \end{aligned} \tag{16}$$

The saturation vapor pressure $e$ was calculated using the Goff and Gratch formula

$$\begin{aligned} \log_{10} e = {} & 7.90298 \quad 1 - \frac{T_S}{T} \quad + 5.02808 \log_{10} \\ & \frac{T_S}{T} \quad + 1.3816 \times 10^{-7} \quad 1 - 10^{11.344 \quad 1 - \frac{T}{T_S}} \\ & - 8.1328 \times 10^{-3} \quad 1 - 10^{3.48149 \quad 1 - \frac{T^S}{T}} \\ & + \log_{10} e_S \end{aligned}$$

where

$e$ is the saturation water vapor pressure (hPa)

$T$ is the absolute air temperature in kelvins

$T_S$ is the steam-point ( boiling point at 1 atm.) temperature (373.15 K)

$e_S$ = 611 Pa is the $e_S$ at the steam-point pressure (1 atm = 1013.25 hPa)

**Results**

Net contributions calculated with the collected data for each component of the energy balance model for the period of September 2006 to September 2009 were respectively: -40525.122 W/m$^2$ for latent heat, -12842.599 W/m$^2$ for sensible heat and 37961.148 W/m$^2$ for net radiation. At the end of the measurement period, the daily average energy balance was calculated as -14.94 W/m$^2$. Integrating for energy loss for the three-year period, yields a total energy of ≅10.73 x 10$^8$ J/m$^2$. If water for freezing is available, the computed energy loss would be enough to freeze ≅4163.5 kg/m$^2$ of water on the glacier surfaces. By assuming these energy loss processes are occurring at an average air temperature of 2.57°C (this study) and by considering the average density of glacial ice at Popocatépetl volcano is 900 kg/m$^3$ (Delgado-Granados, 2007), the total energy loss computed would be sufficient to freeze an equivalent ≅4.6 m$^3$ cubic meters of superimposed ice on a typical Mexican glacier between 2006-2009.

There are only 4 days of data gaps for temperature, net radiation, relative humidity and pressure from both automatic weather stations. Precipitation data of the automatic weather stations are not considered here for the calculation of the energy balance.

There are only 27 days with temperatures above 0°C within the first year with a maximum value of 1.6 °C, which was present on October. For the rest of the period, temperatures lay near the melting point, however a few excursions down to the -10°C were detected.

Tables 1-4 show the mean value of energy balance components and air temperature, together with the correlation matrix of all of these parameters on Glaciar Norte glacier.

Figures 2 and 5 show the variability of air temperature and energy balance components. The results demonstrate the low variability of air temperatures above the glacier throughout the year (ranging only between 0 and -10°C). Periods with relatively high temperatures (but below zero) and low subfreezing temperatures are related with hot summer and cold winter seasons respectively. Net radiation values are higher than latent and sensible heat, and the variability of net radiation clearly dominates the energy balance. Even more, figure 3 shows that the variability of net radiation and energy balance are highly positive correlated, Table 1 shows the same relationship.

**Table 1.** Correlation coefficients for energy balance components and temperature at Glaciar Norte, from September 19 2006 to October 15 2009 (n=1117).

| table 1 | EB | NR | H | LvE | T |
|---|---|---|---|---|---|
| Averag | -14.94 | 33.46 | -11.54 | -36.85 | -2.57 |
| std dev. | 66.42 | 64.06 | 13.61 | 41.39 | 1.64 |
| EB | 1 | 0.67 | 0.40 | 0.41 | 0.16 |
| NR | | 1 | -0.26 | -0.36 | -0.14 |
| H | | | 1 | 0.743 | 0.61 |
| LvE | | | | 1 | 0.29 |
| T | | | | | 1 |

Average and standard deviations for energy fluxes in W/m2 and temperature in °C. Significant correlations (p<0.05) are marked in bold.

**Table 2.** Correlation coefficients for energy balance components and temperature at Glaciar Norte, from December 2006 to May 2007 (Dry season n=150).

| table 2 | EB | NR | H | LvE | T |
|---|---|---|---|---|---|
| average | 17.32 | 68.93 | -11.91 | -39.68 | -3.15 |
| std dev. | 92.40 | 75.26 | 15.26 | 49.38 | 1.68 |
| EB | 1 | 0.74 | 0.59 | 0.54 | 0.23 |
| NR | | 1 | 0.04 | -0.13 | 0.17 |
| H | | | 1 | 0.74 | 0.36 |
| LvE | | | | 1 | 0.07 |
| T | | | | | 1 |

Average and standard deviations for energy fluxes in W/m2 and temperature in °C. Significant correlations (p<0.05) are marked in bold.

**Table 3.** Correlation coefficients for energy balance components and temperature at Glaciar Norte, from December 2007 to May 2008 (Dry season n=152).

| table 3 | EB | NR | H | LvE | T |
|---|---|---|---|---|---|
| average | -1.02 | 64.85 | -18.64 | -47.23 | -3.74 |
| std dev. | 64.03 | 67.51 | 16.11 | 41.51 | 1.63 |
| EB | 1 | 0.66 | 0.34 | 0.32 | 0.27 |
| NR | | 1 | -0.32 | -0.47 | 0.03 |
| H | | | 1 | 0.67 | 0.58 |
| LvE | | | | 1 | 0.13 |
| T | | | | | 1 |

Average and standard deviations for energy fluxes in W/m2 and temperature in °C. Significant correlations ($p<0.05$) are marked in bold.

**Table 4.** Correlation coefficients for energy balance components and temperature at Glaciar Norte, from December 2008 to May 2009 (Dry season n=150).

| table 2 | EB | NR | H | LvE | T |
|---|---|---|---|---|---|
| average | -18.82 | 61.28 | -19.01 | -61.08 | -3.30 |
| std dev. | 75.23 | 52.41 | 16.21 | 49.44 | 1.54 |
| EB | 1 | 0.56 | 0.72 | 0.68 | 0.57 |
| NR | | 1 | -0.003 | -0.20 | 0.23 |
| H | | | 1 | 0.78 | 0.74 |
| LvE | | | | 1 | 0.37 |
| T | | | | | 1 |

Average and standard deviations for energy fluxes in W/m2 and temperature in °C. Significant correlations ($p<0.05$) are marked in bold.

Results here involve three dry seasons and almost four wet seasons, comprising the 2006-2009-study period.

During this study period of 2006-2009, the net radiation shows the highest variability of all energy fluxes representing the main energy source to melt ($\sigma_R \approx \sigma_{SEB}$) which can be seen in Tables 1-4. The latent heat flux ($L_E$) is the principal sink of energy on the glacier surface due to the strong variability of sublimation, which is larger than for sensible heat flux ($H$). Sensible heat flux is also negative along all data which means a cooling of the surface and sometimes this could means that sublimation is inhibited and melting is enhanced.

Finally, it was calculated the annual cycle of the energy balance and the energy fluxes for these three years of measurements (Figure 4). The variability of the net radiation shows high values between January and March, which is the same for energy balance. For these months, latent and sensible heat fluxes show low negative values compared with the net radiation fluxes. This means the net radiation (R) controls the surface energy balance (B) as shown by the strong correlation between these variables, $r^2(R|B)$ = 0.67 (Table 1, Figure 3). Turbulent fluxes were poorly correlated to net radiation (Tables 1-4).

The behavior of air temperatures measured just over the glacier and measured in a zone nearby (but not over the glacier) is strongly correlated (Tables 1-4). The variability of temperatures observed are very similar, even though the temperatures just off the glacier margins are slightly higher than temperatures above the glacier surface. In contrast, air temperature variations outside the glacier margin have lower standard deviations than air temperatures just above the glacier. Compared with glaciers at mid and high latitudes, the temperature standard deviations at Glaciar Norte glacier were lower (see Sicart *et al*., 2008). For comparison, the work of Sicart *et al*. (2008) indicates, temperature on Zongo glacier (4900 to 6000 masl at 16°S latitude in Bolivia) is very poorly correlated with R and Surface Energy Balance. A similar situation occurs at Glaciar Norte where temperatures were not significantly correlated to R. For this glacier studied, air temperature was positively correlated with sensible heat flux, which implies a heat flux component similar to that of mid-latitude glaciers (Sicart *et al*. 2008; Zemp *et al*., 2007; Dyurgerov, 2002; Braithwaite, 1981). This relationship could mean that sensible flux is relevant when temperature rises enough to melt the glacier surface.

## Discussion

The energy balance presented in this paper is first time the energy balance variability of glaciers at 19°N latitude has been approximated with a comprehensive theoretical basis. Here,

the strong relationship between net radiation and energy balance dominates the energy exchanges on the glacier surfaces. From this, it should be possible to identify similarities and differences that link the behavior of these glaciers with others in tropics. Within this section, variability of the energy balance components is compared to temperature variations using the same parameters documented for other tropical glaciers. This comparison is based on the effect of each meteorological and energy flux to the energy and mass balance variabilities. For the case of Mexico, we only focus on the energy balance variability. In this way, patterns are established which can explain the relationship between the energy budget and how glacial retreat happens in the tropics. All of these relationships are summarized on Table 5 in order to simplify the comparison of Glaciar Norte with tropical glaciers.

*Energy balance components*

When a component of the energy balance is positive, the physical processes associated with it favor ablation. But when energy balance is negative, the associated physical processes favor accumulation if the proper temperature and precipitation conditions for accumulation are present.

In Figure 2, the components of the energy balance are plotted as independent values. The values of sensible heat are smaller than those for latent heat, although both have very similar behavior.

Latent heat is predominantly negative for the study site. This explains the presence of accumulation on the glacier. Contrary to net radiation, which is mainly considered positive, Latent heat seems to cause more ablation

**Table 5.** Comparison of Glaciar Norte response to energy fluxes and temperature versus tropical and mid-latitude glaciers.

| | Cordillera Blanca [Vuille et al., 2008] | Zongo [Francou et al., 2003] | Saint-Sorlin [Sicart et al., 2008] | Glaciar Norte |
|---|---|---|---|---|
| Temperature variability | ±6 °C | ±6 °C | > ±6 °C | ±5 °C |
| Precipitation rate | 770 mm/year | 668 mm/year | > 1100 mm/year | 454 mm/year |
| Main factor to variability of Mass balance | Precipitation | Sea temperature anomalies | Air temperature | Net radiation |
| First energy source | Net short-wave radiation | Net short-wave radiation | Incoming long-wave radiation | Net radiation |
| Second energy source radiation | Latent heat | Latent heat | Incoming short-waves | Latent heat |
| Effect of air temperature | Low | Low | High | ---- |
| Effect of sensible heat | None | None | High | ---- |
| Effect of latent heat | High | High | None | Low |
| Effect of net radiation | High | High | None | High |

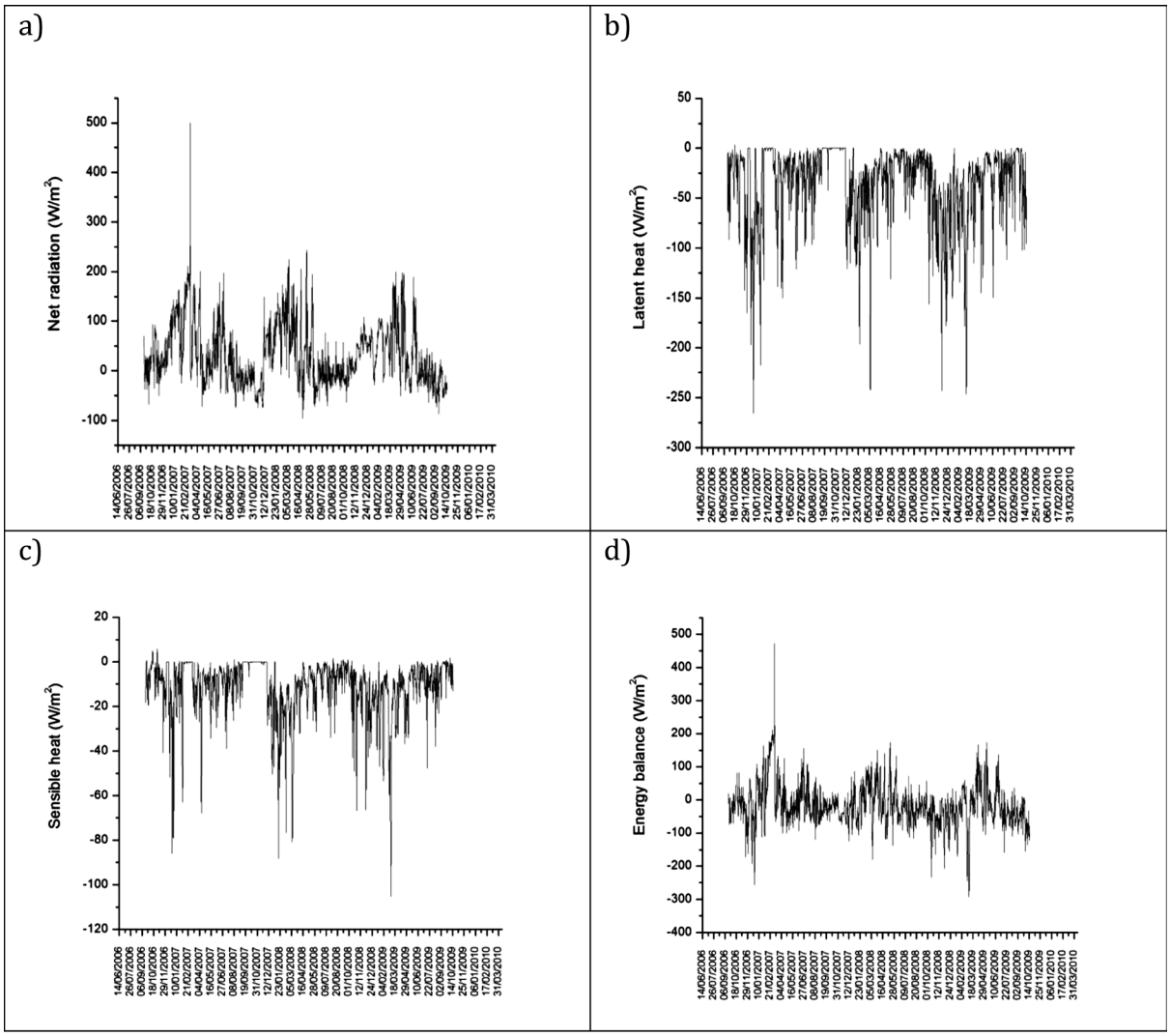


**Figure 2.** Variability of the Energy balance and its components are shown. Note how the energy balance and net radiation variations are much more similar than between Latent heat and Energy balance or between Energy balance and Sensible heat. Also it is possible to see that Latent and Sensible heat variations are similar and both have predominantly negative values, as a consequence of this, the Energy balance oscillates between positive and negative values.

on the glacier. In addition, there is a greater correspondence between the energy balance and the radiative component than between the energy balance and any other component measured on this glacier. The correspondence found between the energy balance and net radiation shows a positive correlation of about 0.67 (Figure 3). From this value it can be said that the radiative components involved in net radiation mainly determine the regularity and variability of the energy balance. After discovering that fact, it is possible to conclude that the principal factor governing energy balance variability is net radiation, however, the fluxes of sensible and latent heat are very important in terms of the magnitude of the energy balance. It is possible to compare energy balance of Mexican glaciers and more tropical glaciers because the net radiative and the latent heat fluxes dominate the energy balance of these glaciers and not the sensible heat flux (Francou *et al*., 2003; Favier *et al*., 2004).

So, the energy available for melting and sublimation (given by the energy balance) is determined by sensible and latent heat fluxes, while the energy variability is driven by net radiation. Figure 5 shows the annual variation behavior of temperature, relative humidity

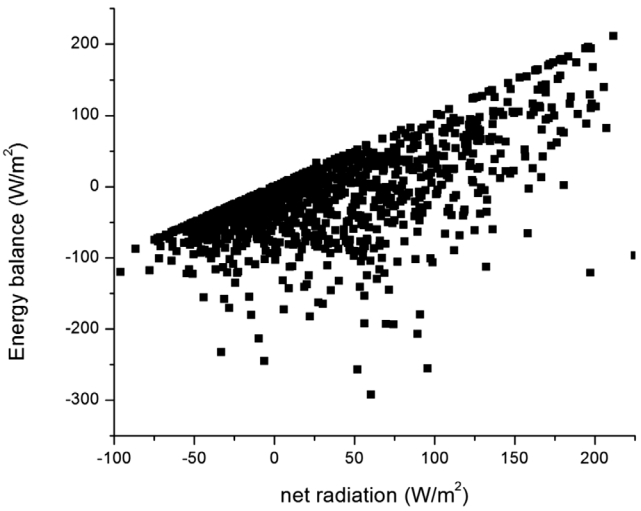


**Figure 3.** Scatter plot of Net Radiation vs. Energy Balance.

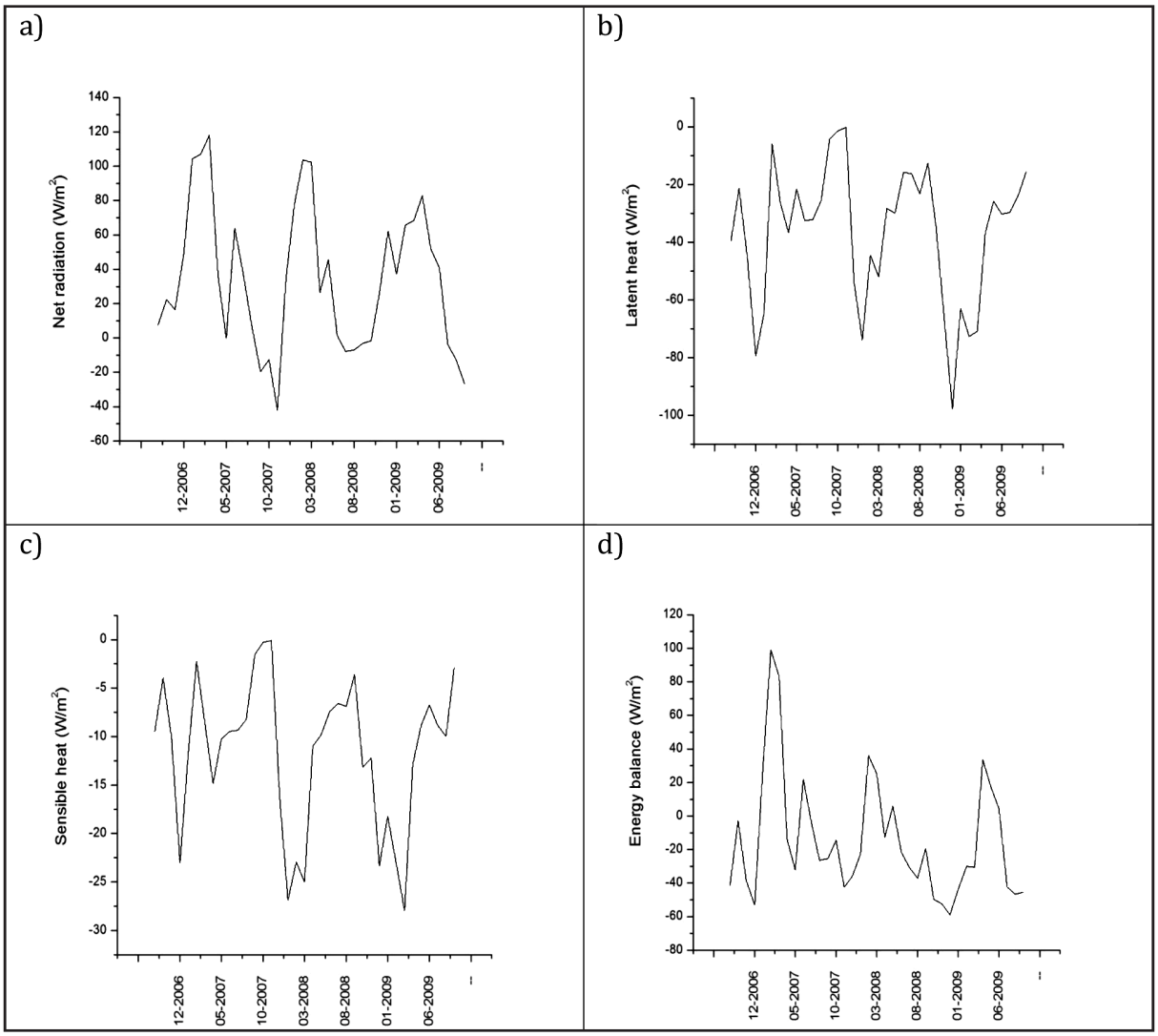


**Figure 4.** Annual variation for each component of energy balance (sept 06-oct 09). During all of these three years there is an ablation period where the values of the energy balance are high. Between January and march the net radiation is more intense than during the rest of the year. However, the components corresponding to the sensible and latent heat fluxes seems to have almost an opposite variation pattern.

and net radiation. This behavior is essential to the formation of wet and dry seasons and its alternation along the year.

Although net radiation is the principal factor driving energy balance variations, it is important to note that the sequence of maximum and minimum balance although followed by net radiation, is opposite to that followed by sensible and latent heat. Thus, the role of latent and sensible heat fluxes appear to counter balance the effects of net radiation.

*Regime and seasonality*

The annual cycle of the four energy balance components was analyzed during the three years of this study (Figure 4). During all three study years, there is observed an ablation period where the values of the energy balance are high (Figure 4, d). Nonetheless, there are some periods when the energy balance values are low, which could mean accumulation periods. However, as ablation is present during almost year, the annual variation of energy balance and the energy available for melting are driven by net radiation variability, similar to what happens at tropical glaciers (Sicart *et al*., 2008). However, from September to November the glacier experiences a strong accumulation period, and also registered the maximum annual accumulation. This phenomenon is similar to that of glaciers in the outer tropics (such as near 23° N) where the ablation is low at the end of the balance year (Francou *et al*., 2003).

Temperature and relative humidity have a similar behavior throughout the year. It is possible to observe an oscillation of annual regularity, where air temperature begins to descend at the end of October to early November causing the air to contain less steam water (Figure 5a and 5b). In addition, a decrease in relative humidity begins during the same period. As a result, two seasons are defined during the year: a humid and a dry season (Figure 5, un-shaded and shaded zones respectively).

Sometimes during the summer, severe thunderstorms may occur that momentarily deposit sleet and hail on Mexican glaciers. The deposited icy material does not usually stay long, and in most cases disappears in a few days after the intense rainfall event nearby ends. This melt is fast between summer season accumulation events, when the sky is clear and the solar radiation is intense. It is common to observe that after major precipitation events, that runoff increases and the soil becomes saturated with moisture. It is important to note that although most of the snow melts and is lost as runoff, also a certain portion percolates into the glacier and may become internal accumulation or also may become superimposed ice and thus, storms may contribute slightly to reduce the energy available for melt.

It is noticeable that during the dry season, lower temperatures are recorded when low humidity is registered (Figure 5). Therefore, during the dry season it is difficult to reach a natural freezing point, since at low temperatures lower humidities are required for saturation of an ice-water-air mix. Also, during the dry season the sensible heat flux is strongly correlated with temperature, where temperature controls the interchange of sensible heat flux between glacier and atmosphere. The net radiation contains the energy available for melting and overall ablation occurs during the dry season. It is remarkable that between December-February the annual oscillations of temperature (Figure 5a), atmospheric pressure (Figure 5c), and relative humidity (Figure 5b) reach a minimum value. The low pressure registered in these months also impedes the air saturation process and reduces the effect of latent heat to sublimation. Furthermore, the net radiation reaches a maximum during those months (Figure 5d), thus causing ablation and glacier thinning. The low pressure periods shown for the summit weather station are coincident with low atmospheric pressures reported for lower altitudes, and are attributed to the passage of cold fronts. Turbulent sensible heat flux is small and its variation is low because temperatures remain low during the dry early winter season; this is the same for glaciers like Zongo (see Sicart *et al*., 2008). However, if sublimation is strong this partly cancels out the energy gains in *H* and the sum of the turbulent fluxes remains small over the glacier. For Glaciar Norte this behavior is different because *H* is negative and can sum to the latent heat allowing sublimation of the glacial surface. Nevertheless, net radiation is stronger than turbulent fluxes and melting is more relevant than sublimation.

Between January-March the net radiation is more intense than during the rest of the year, because the weather is often cloud free over the highest Mexican summits. However, the components corresponding to the sensible heat and latent heat fluxes also present high negative values in January (Figure 4, c and d). Therefore, during this period the physical processes in connection to the sensible heat and latent heat lead to accumulation and mass

gain on the glacier, whereas the radiative processes lead to ablation and mass loss on the glacier. On the other hand, it can be observed that the energy balance during the same period is strongly positive but begins to decrease during about May. So, from December to May, ablation is dominant.

During the ablation period, the glacier receives energy that will be used to increase its temperature up to the melting point and from this point on the energy will be used to melt ice. It is important to notice that the ablation period coincides with the dry season, with a decrease of temperature and atmospheric pressure. So, it would be interesting to measure surface temperature of glacier in order to get better estimation of heat fluxes and to better estimate internal glacial processes, such as superimposed ice formation.

In general, the recorded temperature is so close to the melting point that the ice near the surface does not need to increase its temperature much to reach that point. This causes the component of sensible heat to be low; however, during the ablation period, the sensible heat flux is more negative than during the rest of the year. That is because when the air temperature decreases, the glacial surface

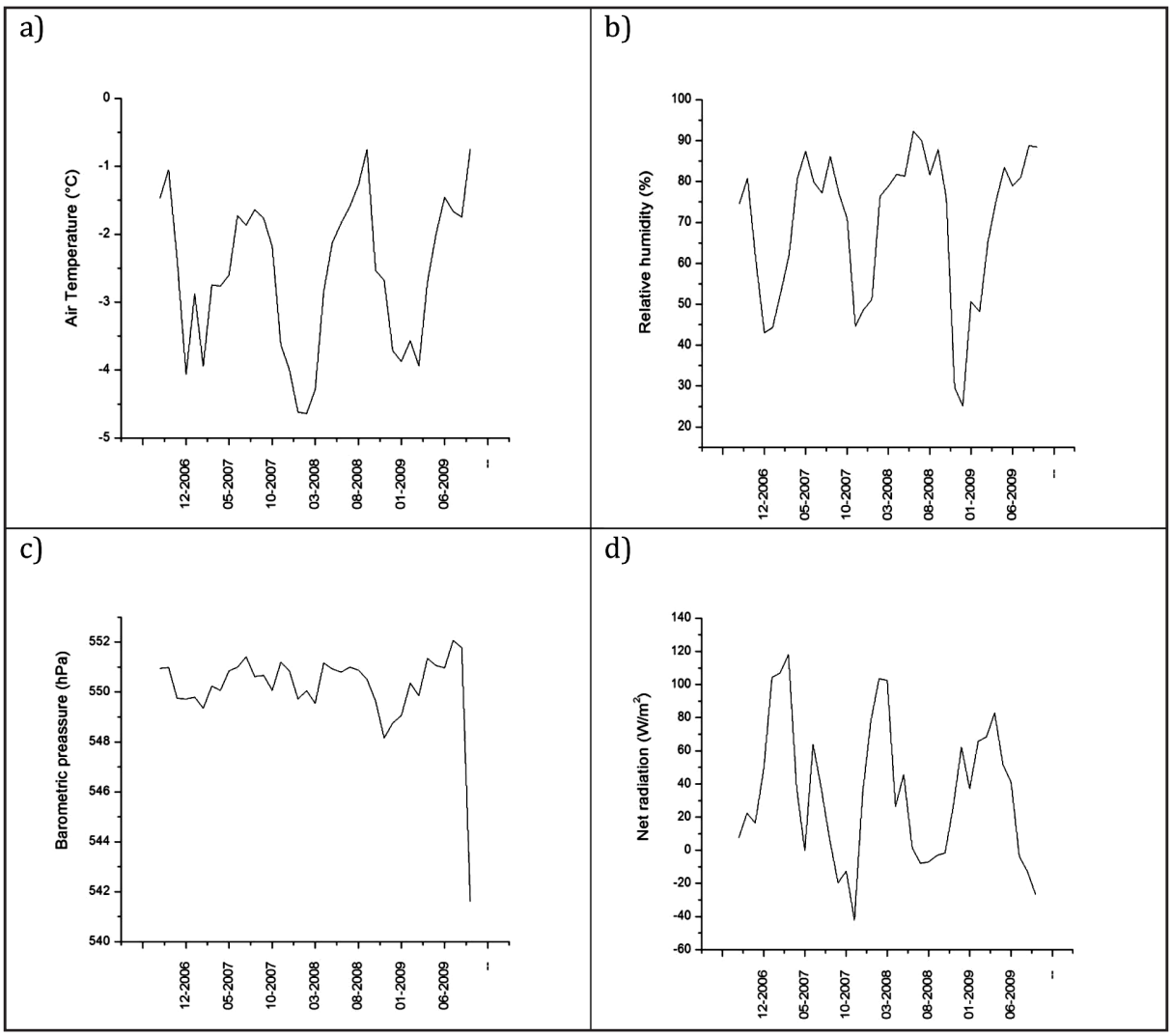


**Figure 5.** Seasonality of air temperature, relative humidity, barometric pressure and net radiation. Barometric pressure is nearly with stable values, nevertheless, It can be determined an alternation of a wet and a dry season along the year. Temperature and relative humidity have a similar behavior with an oscillation of annual regularity. When temperature is lower also air is dryer, therefore, during dry season is it difficult to reach freezing point.

needs to release energy to be in thermal equilibrium with the surrounding air.

The dry season, observed between November-May, coincides with the NH winter season when occasionally a polar air mass descends toward Mexico from the north of the continent (Jauregui, 2004). These polar-type systems can spread stronger than normal winds and may cause the temperatures to abruptly drop. This increase in wind speed is the cause of the increase (in the importance) of the latent heat flux in the energy balance, due to elevated turbulent heat flux. On the other hand, the decrease in relative humidity during these frigid patterns causes a decrease in cloud cover over the glacier's surface, which contributes to the increase in registered net radiation during the wintertime dry season.

There are occasionally rare storms during winter, however, and for these cases, the internal and surficial refreezing will occur more easily. The refreezing happens more often after storms of late fall and early winter and this refreeze is the origin of the superimposed ice is usually found on the glacier as ice layers or surface covering sheets. The effect of refreezing of the storms in the energy balance is reflected by the fact that during these seasons the energy balance reaches its minimum. So we can say that storms during all seasons play a role in recharging the glacier that in the future should be evaluated so we can quantify their importance better.

It should be noted that the first year of data collection coincided with an "El Niño" winter (2006) and the beginning of "La Niña" year in March 2007 (Centro Internacional para la investigación del fenómeno del Niño, Boletín CIIFEN April 2007, available from: http://www.ciifen-int.org/images/stories/pronostico_est/Boletn_CIIFEN_April_2007.pdf, last access: 7 August 2012). The impacts of "El Niño" during the winter can be described in general as heavy rainfall and anomalously low temperatures, especially in the northern part of Mexico due the entrance of baroclinic waves and cold fronts from the north due to amplifications of the winter circulation cycle in North America (Magaña *et al*., 1999). The winter effect of "El Niño" during the year of study is associated immediately with the possibility glacier accumulation during the winter months that still coincides with the dry season. Moreover, during November-December the lowest values in our energy balance results indicate a large accumulation of mass on the glacier during this time.

During March 2007 study period, the ocean-atmosphere climate system went into the "La Niña" phase. So, for the following months the glacier observations recorded correspond to the "La Niña" spring and summer. During "La Niña" summers, the weather tends to rain across most of Mexico. Although most rainfalls are considered normal, there are greater chances that precipitation amounts could be anomalously intense during a La Niña year. There are several factors that can result in higher rainfall than normal over southeastern Mexico, but perhaps the most important is the activity of the easterly moisture stream embedded in the ITCZ and hurricanes produced in the Caribbean and Gulf of Mexico (Magaña *et al*., 1999). During La Niña or Neutral ENSO years hurricanes are more likely to provide extra precipitation into eastern Mexico near the study site during August through November.

*Visual observations*

The *penitents* are composed of "praying" snow peaks related to superficial ablation, that mainly form during the dry season at high altitudes in the Himalayas, Andes, Rocky Mountains, sometimes southern slopes of the Cascade volcanoes and the Alps (Betterton, 2001; Corripio and Purves, 2006). During the dry season, *penitents* are present on Glaciar Norte confirming that ablation occurs during this period as a result of evaporation and/or sublimation, and not just melt.

## Conclusions

This study allows understanding of energy exchanges between a high mountain glacier and the atmosphere throughout several years at the Citlaltépetl region near 19° N latitude in Mexico.

The annual variability of energy balance in the glacier is characterized by the existence of a period of important ablation during the first half of the year during the Northern Hemisphere (NH) winter season, when, although at relatively low temperatures, the atmospheric pressures and relative humidities reach a minimum with a remarkable increase in net radiation. This ablation period during the tropical NH dry winter season is followed by a period of minimal net accumulation during the tropical NH wet summer season. Although the first year of this study coincided with the transition between "El Niño" and "La Niña", this did not have much influence on the annual variability of energy balance of the glacier, yielding similar results as compared to the years without these phenomena. The variability

of energy balance observed during this study does not correspond to normal tropical glaciers reported elsewhere because of the interruption of the ablation period. Differences may also be due to the zone of influence of the Intertropical Convergence Zone (see Figure 1) which wobbles northwards across central Mexico during the summer season.

Following current trends, the glaciers in Mexico could disappear in a few years, which is in correspondence with the published climatic projections made by Christensen *et al*. (2007). However the Mexican glaciers have already survived longer than expected, suggesting that internal refreezing of meltwater, *penitent* physics, storminess and hurricane variability may play more significant roles in modulating glacier balance than currently considered. Although the data collected and used for this study were not enough to provide a conclusion about the influence of climatic change on energy balance, the data obtained are important for future meteorological, glaciological and water supply studies.

**Acknowledgements**

This study was financially supported by DGAPA (grant IN-113914) and CONACYT (grant 83633). The authors would like to thank the government of Puebla for its collaboration with its infrastructure to install the instrumentation in the field. Field assistance from several individuals is greatly appreciated: José Manuel Alvarez, Oscar Díaz Molina, Lorenzo Ortíz Armas, Thomas Berger (IRD-Bolivia), Luis Maisincho (IRD-Ecuador). G. Ontiveros González and J. Cortés Ramos acknowledge masters and doctoral financial support from CONACYT and are grateful for support from the Posgrado en Ciencias de la Tierra at UNAM. The authors are deeply indebted with Dr. Melinda M. Brugman who thoroughly revised previous versions and her careful editing substantially improved this manuscript.

**References**

Betterton M.D., 2001, Theory of structure formation in snowfields motivated by penitentes, suncups, and dirt cones. *Phys. Rev. E*, 63, 5, 056129, doi:10.1103/PhysRevE.63.056129.

Braithwaite, R.J., 1981, On glacier energy balance, ablation, and air temperature. *J. Glaciol.,* 27, pp. 381–391.

Corripio J.G., Purves R.S., 2006, Surface Energy Balance of High Altitude Glaciers in the Central Andes: The Effect of Snow Penitentes. In: Carmen de Jong, David Collins, and Roberto Ranzi (eds.). *Climate and Hydrology in Mountain Areas.* [Online]. John Wiley & Sons, Ltd. pp. 15–27. Available from: http://onlinelibrary.wiley.com/doi/10.1002/0470858249.ch3/summary [Accessed 23 August 2012].

Christensen J.H., Hewitson B., Busuioc, A., Chen, A., Gao, X., Held, I., Jones, R., Kolli, R.K., Kwon, W.-T., Laprise, R., Magaña Rueda, V., Mearns, L., Menéndez, C.G., Räisänen, J., Rinke, A., Sarr, A. and Whetton, P., 2007, *Regional Climate Projections*. [Online]. 2007. Climate Change, 2007: The Physical Science Basis. Contribution of Working Group I to the Fourth Assessment Report of the Intergovernmental Panel on Climate Change, University Press, Cambridge, Chapter 11. Available from: http://epic.awi.de/17617/ [Accessed: 18 September 2012].

Delgado-Granados H., 2007, Climate change vs. volcanic activity: Forcing Mexican glaciers to extinguish and related hazards. In: *Instituto de Hidrología, Meteorología y Estudios Ambiantales*, *Proceedings of the First International Conference on the Impact of Climate Change on High-Mountain Systems*. Instituto de Hidrología y Estudios Ambientales, Bogotá, Colombia. pp. 153–168.

Delgado Granados H., Julio Miranda P., Huggel C., Ortega del Valle S., Alatorre Ibargüengoitia M.A., 2007, Chronicle of a death foretold: Extinction of the small-size tropical glaciers of Popocatépetl volcano (Mexico). *Global Planet. Change*, 56, 1–2, 13–22, doi:10.1016/j.gloplacha.2006.07.010.

Dyurgerov M., 2002, Glacier mass balance and regime: Data of measurements and analysis*. Occasional Paper No. 55. Boulder, CO: Institute of Arctic and Alpine Research, University of Colorado,* 268 pp.

Favier V., Wagnon P., Ribstein P., 2004, Glaciers of the outer and inner tropics : a different behavior but a common response to climatic forcing*. Geophys. Res. Lett.,* 31 (L16403), pp. 1–5.

Francou B., Pouyaud B., 2004, Metodos de Observacion de Glaciares en los Andes tropicales: Mediciones de terreno y procesamiento de datos. In *Great Ice*, *Report,* 1st ed., IRD, France. pp. 211-212.

Francou B., Vuille M., Wagnon P., Mendoza J., Sicart J.E., 2003, Tropical climate change recorded by a glacier in the central Andes during the last decades of the twentieth century: Chacaltaya, Bolivia, 16°S, *J. Geophys. Res.,* 108, D5, 4154, doi:10.1029/2002JD002959.

Jauregui E., 2004, Contrastes bioclimáticos entre el mar y la montaña en la zona central del estado de Veracruz (México). In: *El clima entre el mar y la montaña*, *Aportaciones presentadas al IV Congreso de la Asociación Española de Climatología*. Universidad de Cantabria, Santander, España. pp. 41-50.

Kaser G., Osmaston H., 2002, Tropical Glaciers. *Cambridge University Press,* Cambridge, England. 228 pp.

Kuhn M., 1979, On the computation of heat transfer coefficients from energy-balance gradients on a glacier, *J. Glaciol.*, 22, 263-272.

Magaña V.O., 1999, Los impactos de El Niño en México*. Universidad Nacional Autónoma de México*, Mexico City, Mexico.

Oerlemans J., 2001, Glaciers and Climatic Change. *A. A. Balkema Publishers, Brookfield*, Vt. 148 pp.

Paterson W.S.B., 1994, The physics of glaciers. 3rd. edition. *Pergamon, Oxford, England.* 480 pp.

Sicart J.E., Hock R., Six D., 2008, Glacier melt, air temperature, and energy balance in different climates: The Bolivian Tropics, the French Alps, and northern Sweden. *J. Geophys. Res.*, 113, D24113.

Singh P., Singh V.P., 2001, Snow and Glacier Hydrology. *Kluwen Academic Publishers*, The Netherlands.

Vuille M., Kaser G., Juen I., 2008, Glacier mass balance variability in the Cordillera Blanca, Peru and its relationship with climate and the large-scale circulation. *Global Planet. Change*, 62, 1–2, pp. 14–28, doi:10.1016/j.gloplacha.2007.11.003.

Zemp M., Hoelzle M., Haeberli W., 2007, Distributed modelling of the regional climatic equilibrium line altitude of glaciers in the European Alps. *Global Planet. Change*, 56, 1–2, pp. 83–100, doi:10.1016/j.gloplacha.2006.07.002.

Geofísica Internacional (2015) 54-4: 315-322

Original paper

# Fractalness of land gravity data and residual isostatic anomalies map of Argentina, Chile and western Uruguay

Silvia Alicia Miranda*, Alfredo Héctor Herrada, María Cristina Pacino

Received: July 15, 2014; accepted: June 30, 2015; published on line: October 01, 2015

**Resumen**

Las anomalías de gravedad suelen estar fuertemente influenciadas por la topografía, cuyo efecto es atenuado a través de adecuadas reducciones. Usualmente, ante la falta de información específica, se usa un valor estándar de 2670 kg/m$^3$ para la densidad de la topografía por encima del geoide. Hasta el presente varios métodos han sido implementados para obtener estimaciones de dicha densidad directamente a partir de los datos de gravedad mismos. Una técnica especialmente conveniente para estudios de carácter regional se basa en analizar la naturaleza fractal de las anomalías de gravedad para una región en particular.
En este trabajo se analiza la fractalidad de las anomalías de gravedad para Argentina, Chile y parte de Uruguay continentales utilizando una base de datos de gravedad actualizada. Se estimó la dimensión fractal D de los datos topográficos y de anomalías de gravedad por medio de la técnica de variograma en el dominio espacial. Como resultado de este análisis se encontró que la densidad óptima para esta región tiene un valor de 2300 kg/m$^3$. Esta densidad se usó para preparar un mapa de anomalías residuales isostáticas en el sistema de Airy-Heiskanen. Las principales anomalías reconocidas en este mapa se interpretaron con relación al grado de balance isostático y a las densidades de las rocas cercanas a la superficie.

Palabras clave: anomalías de gravedad, geometría fractal, residuos isostáticos.

**Abstract**

Gravity anomalies are often strongly influenced by topography, which effect is mitigated through appropriate reductions. Usually, a standard value of 2670 kg/m$^3$ is used for the density of topography in the absence of specific information. However, various methods have been implemented to obtain density of topography estimates directly from the gravity data. A particularly suitable technique for regional scale studies is based on analyzing the fractal nature of gravity anomalies for a particular region.
In this paper the fractalness of the onshore gravity anomalies for Argentina, Chile and part of Uruguay is analyzed by using an updated gravity database. The fractal dimensions of the topography and gravity anomaly data were estimated by means of the variogram technique in the spatial domain. As a result of this analysis, it was found that the optimum density for the studied region has a value of 2300 kg/m$^3$. This density was used to prepare a map of isostatic residual anomalies using the Airy-Heiskanen model. The main anomalies recognized on this map were interpreted in relation to the degree of isostatic balance and the densities of rocks near to the surface.

Key words: gravity anomalies, fractal geometry, isostatic residuals.

S. A. Miranda*
Departamento de Geofísica y Astronomía
FCEFN, Universidad Nacional de San Juan
Meglioli (Sur) 1160. 5400 Rivadavia
San Juan. Argentina
*Corresponding author: smiranda@unsj-cuim.edu.ar

A. Héctor Herrada
Departamento de Ingeniería en Agrimensura
FI, Universidad Nacional de San Juan
Av. Lib. San Martín (Oeste) 1109. 5400
San Juan. Argentina
aherrada@uolsinectis.com.ar

M. C. Pacino
CONICET- Facultad de Ciencias Exactas
Ingeniería y Agrimensura
Universidad Nacional de Rosario
Pellegrini 250. 2000
Rosario. Santa Fe. Argentina
mpacino@fceia.unr.edu.ar

## Introduction

Mandelbrot (1967) developed the fractal geometry that allows describing scale invariant phenomena. That is, the spatial variation of a fractal parameter often looks similar at a wide range of scales. Examples in Earth Sciences range from the geological type (e.g., rocky coast line, faulting, seismicity, volcanic eruptions) to the geophysical information such as gravity and magnetic field data, topography, among others.

The fractal nature of a variable is evident from the fact that the power spectrum P (k) is proportional to $k^b$, where k is spatial frequency and b is the scaling exponent that is in practical terms, for instance, the slope of the spectrum in a log-log space. For gravity data, β values range from -3.8 to -5 based on regional or global studies (Maus and Dimri, 1994; Chapin, 1996; Pilkington and Todoeschuck, 2004; Dimri, 2005; Pilkington and Keating, 2012). Among other applications, the fractal structure of gravity or geomagnetic information has been used in computing the optimum gridding interval (Keating, 1993; Pilkington and Keating, 2012), depth estimation (e.g., Pilkington and Todoeschuck, 2004; Gregotski *et al*. 1991; Maus and Dimri, 1996; Quarta *et al*. 2000), inversion of potential field data (Pilkington and Todoeschuck, 1993), determining the optimal Bouguer density to be used for topography reduction of gravity data (Thorarinsson and Magnusson, 1990; Chapin, 1996; Caratori Tontini *et al*., 2007).

Chapin (1996) computed an isostatic residual gravity map for South America based on both the fractal nature and correlation of regional gravity anomalies and topography. The use of these maps in exploration is widespread because they would clearly depict the distribution of densities in the upper part of the crust (Simpson *et al*., 1986; Jachens *et al*., 1996). However, the magnitude of these residual gravity anomalies is dependent on the assumed density values for terrain, lower crust and upper mantle. In his work, Chapin (1996) estimated the optimum density of topography by analyzing the changes in fractal dimension (D) of simple Bouguer anomalies (without terrain correction) calculated with varying densities. As a result, he found a minimum curve superimposed on a regional trend when plotting the curve of fractal dimension versus density. In contrast, Thorarinsson and Magnusson (1990) for Iceland gravity data and later Caratori Tontini *et al*. (2007) for a Mediterranean Sea gravity database, determined simple minimum D versus density curves (U-shaped). This particular feature of D versus density curve for South American data has been attributed to either a long wavelength component (Chapin, 1996) or the use of simple Bouguer anomalies (slab formula reduction), neglecting terrain corrections (Caratori Tontini *et al*., 2007).

Herein, we investigate the fractal nature of onshore gravity anomalies for Chile, Argentina and part of Uruguay, and present a new map of isostatic residual anomalies. Unlike Chapin (1996), who used the power spectral method, the fractal dimension estimation is carried out using the variogram technique for the terrain-corrected Bouguer anomalies. For this study, a more detailed gravity database, which provides a better resolution in regions such as Chile and some Argentine sedimentary basins, was available.

## Topographic and gravity database

The study area ranges from 21° S to 55° S in latitude and 75° W to 55° W in longitude. The gravity database is part of the South American Gravity Project (SAGP) and the Anglo Brazilian Gravity Project (ABGP), carried out under the umbrella of the International Association of Geodesy (Pacino, 2007). The gravity data points were provided by different sources: national and international academic institutions, oil and mining companies and the Geographic National Institute of Argentina (IGN). The data were homogenized and linked to the IGSN 71 gravity datum and referred to the Geodetic Reference System 1980 (GRS80). Data errors are assumed to be less than $0.5 \times 10^{-5}$ m/s² (0.5 mGal). The dataset of the land free-air gravity anomalies is depicted in Figure 1.

The topographic data used for gravity terrain reductions calculations are based on the SRTM_30 PLUS digital elevation model data (Becker *et al*., 2009).

## Fractal dimension of gravity anomalies and topography

The fractal dimension of gravity anomalies has been estimated using spectral methods (Chapin, 1996; Caratori Tontini *et al*., 2007) or variogram techniques (Maus, 1999; Thorarinsson and Magnusson, 1990). Maus (1999) pointed out that the advantage of using this last approach is that it avoids the distortion and loss of information inherent to the computation of Fourier-domain spectra. Thus, variograms in the spatial domain replace spectra in the transformed domain.

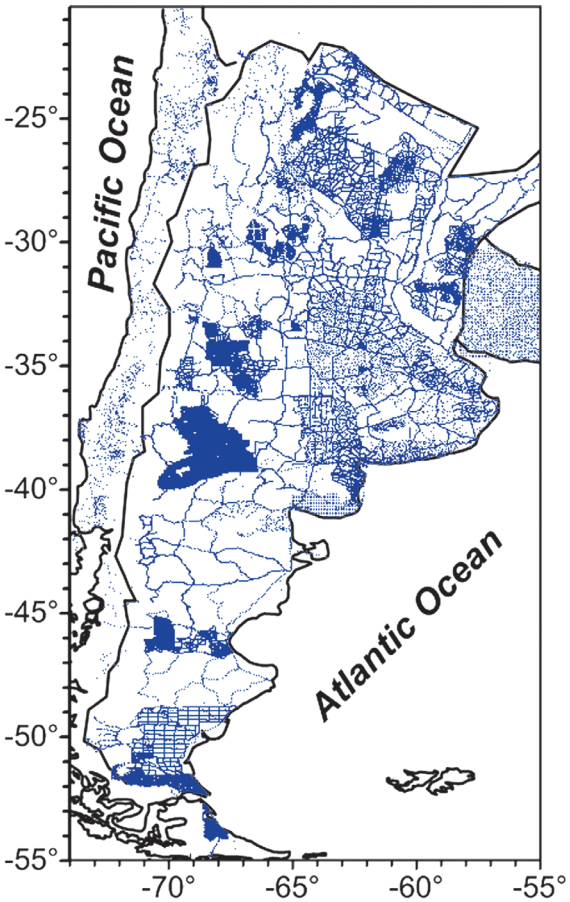


**Figure 1.** Geographical distribution of free air gravity anomalies data over the studied area (point station in blue).

According to Thorarinsson and Magnusson (1990), the fractal dimension of gravitational surfaces can be estimated using a method based on the variogram of a surface whose expected value E is given by:

$$E = [(Z_P - Z_q)^2] = k\,(d_{pq})^{2H},$$

where $Z_p$ and $Z_q$ are values of the surface at points p and q, $d_{pq}$ is the horizontal distance between points, k is a constant and H is a parameter in the range of 0 to 1, which is related to the fractal dimension D as H= 3-D. These kind of surfaces are used as a method of simulating topographic surfaces (Goodchild and Mark, 1987).

Making log-log plots of the variances of surface relief differences versus distances between points, results in a straight line over some range on which the physical phenomenon is fractal. The slope (b) of the plot is proportional to the fractal dimension for that range:

$$D = 3 - \frac{b}{2}$$

It is important to note that the fractal dimension of a data set (e.g., topography) is a number which acquires meaning when compared with the fractal dimension of another variable (e.g., gravity anomalies), obtained using the same method (Chapin 1996). In this context, the fractal dimensions for gravity anomalies and topography here determined are not directly comparables with those calculated by Chapin (1996) who used a spectral approach.

Figure 2a shows the variogram of topography data from the continental Argentina, Chile and western Uruguay database (see station points in figure 1). The best linear trend shows a fractal dimension of 2.479 ± 0.007 for all distances, according to the recognized fractal nature of topography (Turcotte, 1997). Deviation from linearity is observed at the longest distances because of the small number of pair points.

It has been pointed out (Chapin, 1996) that gravity anomalies are a combination of two components: one related to the topography, which is scale-independent (or fractal), and a second one, which is scale-dependent, due to the distributions of density. For instance, in the case of regions where isostatic balance prevails, the long wavelength free air anomalies are scale-dependent while the short wavelength free air anomalies show a fractal nature. Figure 2b displays the variogram plot for the free air gravity data of the studied area. Note that the data fall on a straight line between approximately 5 km and ~80 km indicating a fractal surface (D= 2.469 ± 0.001). Thus, in this range the fractal dimension of free air anomalies are nearly the same as that for topography (Figure 2a). At larger distances (> 80 km) the linearity disappears suggesting a non-fractal behavior and thus the topographic load must be supported by isostatic compensation.

## Determining the optimum Bouguer density

The central idea of the fractal method to estimate a Bouguer density is based on the classical Nettleton's technique (Nettleton, 1939): the optimum Bouguer density should reduce in short wavelengths the correlation between free air gravity anomalies and topography. These crustally supported anomalies would

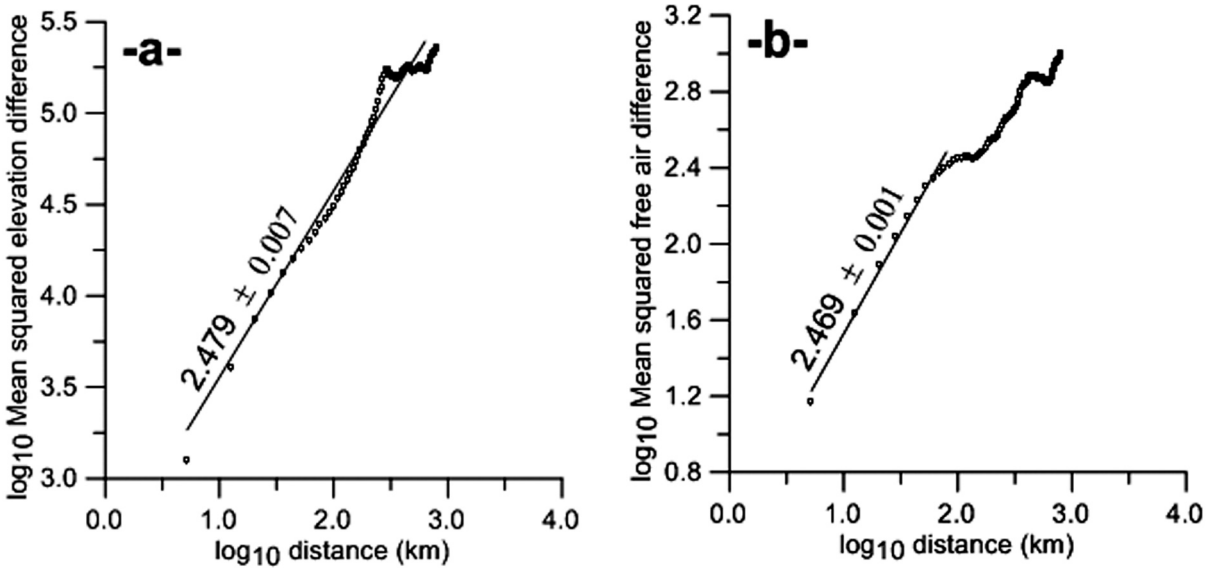


**Figure 2.** a) Variogram of the topography data over the study area ($R^2$= 0,97). b) Variogram of free air gravity anomaly data set for the Chile, Argentina and western Uruguay ($R^2$= 0,99). An estimate of the fractal dimension D is derived from the slope of the linear range of these plots. Note that fractal dimensions for topography and free air gravity anomalies are very close to each other. This demonstrates the relationship between topography and free air anomalies at wavelengths shorter than 80 km.

be represented in the first (on the left) part of the variogram (figure 2b) where the gravity anomalies are scale independent and its fractal dimension could be used to estimate a topographic density (Thorarinsson and Magnusson, 1990). Amongst all reasonable topographic densities, we should find the one that reduces the roughness of the Bouguer anomaly data. Minimizing the roughness of a surface is equivalent to reducing the fractal dimension of that surface.

Thus, variograms were computed for the complete Bouguer anomalies calculated for topographic densities ranging from 0 through 4000 kg/m$^3$. Terrain reductions were calculated using the detailed digital elevation model SRTM_30 PLUS (Becker *et al*., 2009) and a combination of the methods described by Nagy (1966) and Kane (1962). A simple Bouguer correction by a spherical cap, computed to a radial distance of 166.7 km, was also applied. Fractal dimensions, in a range of 2.469 to 2.425, were estimated from 12 km to the distance class of 80 km.

Figure 3b depicts a plot of the fractal dimensions versus the corresponding reduction density. It results in a parabolic or U-shaped curve. A least square fit gives the optimal density value ~2300 kg/m$^3$. This optimum density for continental Argentina-Chile and part of Uruguay is lower than the value of 2600 kg/m$^3$ estimated by Chapin (1996) for all South America. In our case, we use an improved database, a terrain corrected Bouguer anomalies data set and a different methodology for estimating the fractal dimension.

**Map of isostatic residual gravity**

Figure 4 shows the map of isostatic residual anomalies for Chile, Argentina, and part of Uruguay. The isostatic crustal thicknesses (M) in the Heiskanen-Airy system were sized from the topography (H) as follows (Simpson *et al*., 1986):

$$M = T + \frac{\sigma_t}{\sigma_m - \sigma_c} H,$$

where $\sigma_t$ = 2300 kg/m$^3$ is the fractal derived Bouguer density, $\sigma_c$ = 2900 kg/m$^3$ is the lower crust density, $\sigma_m$ = 3300 kg/m$^3$ is the upper mantle density and T= 36 km is the reference crust (Fromm *et al*., 2004). A crust-mantle density contrast of 400 kg/m$^3$ is typically assumed at these latitudes (e.g., Introcaso *et al*., 1992). The gravity effect of the isostatic crust-mantle interface was calculated by the Parker's method (Parker, 1972). Then, it was subtracted from the terrain corrected Bouguer anomalies ($\sigma_t$= 2300 kg/m$^3$) and thus, the resulting anomaly in figure 4 serves as a residual field. Our results are consistent with

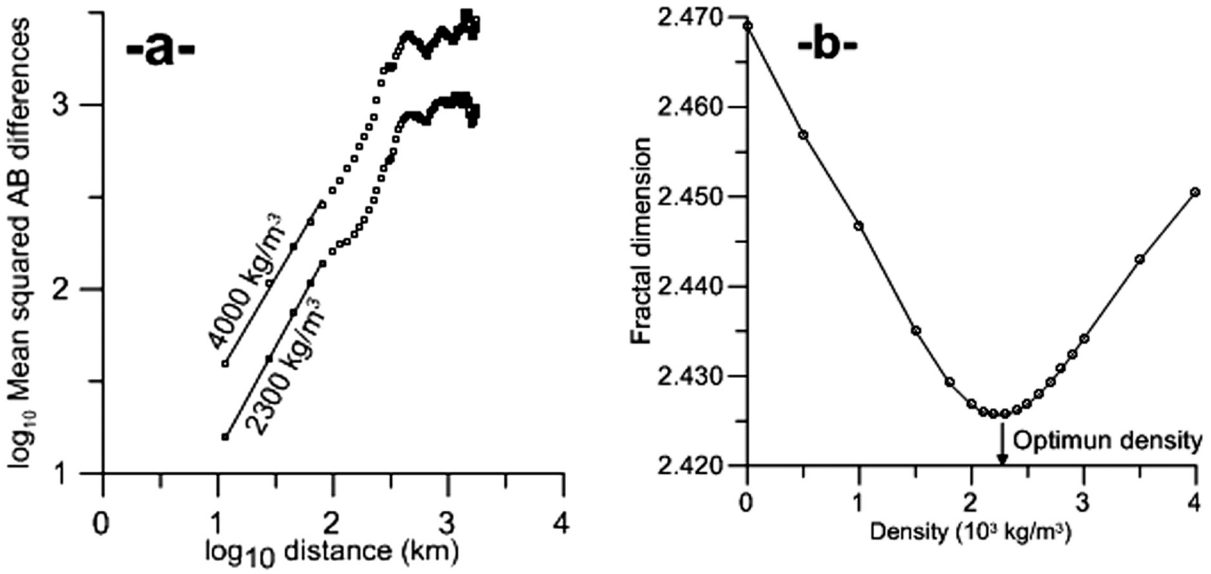


**Figure 3.** a) Variograms of the complete Bouguer anomalies computed for two selected densities for continental Argentina, Chile and western Uruguay. The straight segment in each curve shows the distance range from 12 km to 80 km that has been used to calculate the fractal exponent. The fractal dimensions are 2.450 and 2.425 for densities 4000 kg/m$^3$ and 2300 kg/m$^3$, respectively. b) Plot of fractal dimension versus density. The U-shaped curve shows a minimum at 2300 kg/m$^3$, that is the best density to minimize the gravity effect of topography.

previous residual isostatic maps carried out for this region (e.g., Schmidt and Götze, 2006).

On this map (Figure 4) some main residual anomaly patterns are recognized. In the following, they are interpreted in terms of their wavelength. Thus, long wavelength (regional) anomalies are mainly related to isostatic effects (for instance, crust-mantle interface density variations) while short (local) wavelength anomalies are attributed to geologic bodies in the middle or upper crust, which can be associated with surface or near surface geology and justified by deviations of the actual rock density from the constant topographic density here considered ($\sigma_t$= 2300 kg/m$^3$). The aim of this qualitative interpretation is to explain the isostatic residual gravity field in a very general way, thus providing a basis for further geological o tectonic investigations. The anomalies are labelled (A) to (F) in figure 4.

In the region identified as (A) on the western side of the map in Figure 4, there is a predominance of negative isostatic anomalies over the Cordillera de Los Andes, that would indicate a slight unbalance. Positive anomalies westwards would be linked to both the high density of the oceanic subducting Nazca plate that lies close to the surface and the intermediate-to-basic igneous rocks outcropping along the Andean Coastal Cordillera of Chile (Tassara *et al*., 2006; Prezzi and Götze, 2009).

The broad isostatic residual gravity high (B) centered over the Chaco-Paranaense basin probably does match a slightly thinned crust consistent with results from studies of seismic refraction, receiver function and surface waves (Assumpção *et al*., 2013).

Positive values (C) in the region of the Eastern Pampean Ranges is interpreted in relation with unbalanced isostatic state at crustal level. This Range, despite their topographic expression, has a no pronounced crustal root (Miranda e Introcaso, 1999). This result is supported by seismological studies of receiver function for local (Perarnau *et al*., 2012) and teleseismic events (Gans *et al*., 2011), who found out thicknesses of ~35-40 km for a relatively flat Moho.

Positive residual isostatic anomalies (D) occur mainly over the Rio de La Plata Craton in Argentina which are interpreted in relation to the Precambrian metamorphic basement (i.e., Dalla Salda, 1999). A positive anomaly with approximate ONO course highlights over the Salado basin on the northeast flank of the Buenos Aires Province. This anomaly has been associated either excess of crustal thinning (isostatic unbalance) or a combination of

crustal thinning and positive density contrasts attributed to the intrusive basalts present in the subsurface of the basin (Crovetto *et al*., 2007). Furthermore, a negative residual anomaly is observed to the southward of Buenos Aires, on the Claromecó basin. Gravimetric studies have shown that this basin exhibits crustal thinning with isostatic balance (Ruiz and Introcaso, 2011). Thus, the negative residual isostatic anomaly is related to the powerful infilling sediments (Tankard *et al*., 1995).

Positive residual anomalies (E) on the southwest of Uruguay would be due to the metamorphic basement of the Piedra Alta terrane (Sánchez Bettucci *et al*. , 2010). The association of residual isostatic anomalies with the structural features of the basement of Uruguay has already been pointed out by Oyhantçabal *et al*. (2011), although using different crustal parameters.

In the southern region (F), where gravity data are more sparse, it has not been possible to identify anomalies associated with geological or tectonic features.

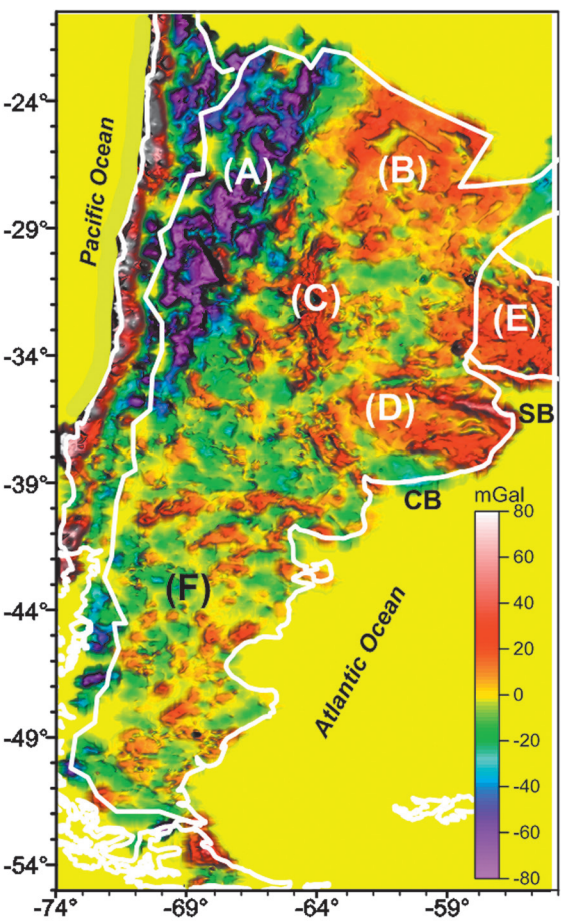


## Conclusions

The fractalness of onshore gravity anomalies for Argentina, Chile and part of Uruguay is analyzed using an updated gravity database. The fractal dimensions of topography and gravity anomaly data were estimated in the spatial domain by means of the variogram technique. Our results point out that for distances up to 80 km: 1- free air anomalies for this region are scale independent (D= 2,469 ± 0,001) and correlate well with the topography, 2- fractal dimensions of the complete Bouguer anomalies in the range of wavelength from 12 km to 80 km, were calculated by using different $\sigma_t$ densities. The fractal dimension versus density curve shows a parabolic trend with a minimum at a density of $\sigma_t$ = 2300 kg/m$^{3}$. This density would minimize the effects of topography and therefore, it would be the optimum density to compute the complete Bouguer anomalies for the study area.

3- This ideal density was used to prepare a new isostatic residual anomaly map (Figure 4) for this region applying the concept of Airy-Heiskanen isostasy. Generally speaking, the Airy isostatic roots lead to a high-degree of compensation, but the residuals show deviations ranging ± 80 mGal. An intriguing feature on this map is that the mean level of isostatic gravity anomaly is negative. This long wavelength anomaly could be attributed to the mantle. We proceed with a general interpretation of some interesting anomalies. A regional minimum (A) along the southern Andes and a high (C) over the Eastern Pampean Ranges, both do reflect isostatic disequilibrium in a region characterized by its active tectonic. Other positive isostatic residual anomalies such as along Coastal Cordillera of Chile, the Piedra Alta terrane of Uruguay (E) and the Rio de La Plata craton (D), can be attributed to geological bodies near the surface. South of 40° S latitude, mainly less positive anomalies in patches of short wavelengths can be seen.

**Figure 4.** Map of onshore isostatic residual gravity of Chile, Argentina and western Uruguay based on an Airy-Heiskanen model of local compensation with parameters: density of topographic load 2300 kg/m$^3$; density contrast across bottom of root, 400 kg/m$^3$; thickness of reference crust, 36 km. Labels identifying the main isostatic residual anomalies zones (A)-(F) are shown. CB: Claromecó Basin, SB: Salado Basin. International boundaries are shown in white line.

**Acknowledgments**

We wish to thank the South American Gravity Project (SAGP) and the Anglo Brazilian Gravity Project (ABGP) for providing the gravity database. We sincerely acknowledge Sabine Schmidt for thoughtful comments and two anonymous reviewers for critical review that improved the manuscript. This work was supported by UNSJ grant 21E98.

**References**

Assumpção M., Feng M., Tassara A., Julià J., 2013, Models of crustal thickness for South America from seismic refraction, receiver functions and surface wave tomography. *Tectonophysics 609, 82-96.*

Becker J.J., Sandwell D.T., Smith W.H.F., Braud J., Binder B., Depner J., Fabre D., Factor J., Ingalls S., Kim S-H., Lander R., Marks K., Nelson S., Pharaoh A., Trimmer R., Von Rosenberg J., Wallace G., Weatherall P., 2009, Global Bathymetry and Elevation Data at 30 Arcs Seconds Resolution: SRTM30_ PLUS. *Marine Geodesy,* 32, 4, 335-371.

Caratori Tontini F., Graziano F., Cocchi L., Carmisciano C., Stefanelli P., 2007, Determining the optimal Bouguer density for a gravity data set: implications for the isostatic setting of the Mediterranean Sea. *Geophys. J. Int.,* 169, 2, 380-388.

Chapin, D., 1996, A deterministic approach toward isostatic gravity residuals—A case study from South America. *Geophysics, 61(4), 1022–1033.*

Crovetto C., Novara I., Introcaso A., 2007, A stretching model to explain the Salado Basin (Argentina). *Boletín del Instituto de Fisiografía y Geología 77, 1-10.*

Dalla Salda L., 1999, Cratón del Río de La Plata. 1. Basamento granítico metamórfico de Tandilia y Martín García, in Caminos, R. (ed.) Geología Argentina (SEGEMAR). Anales 29, 4, 97-100.

Dimri V.P., 2005, Fractals in Geophysics and Seismology: An Introduction. Fractal behavior of the earth system. Chapter 1. Ed.: V.P. Dimri. Springer, 208 pp.

Fromm R., Zandt G., Beck S.L., 2004, Crustal thickness beneath the Andes and Sierras Pampeanas at 30° S inferred from Pn apparent phase velocities. *Geophys. Res. Lett.,* 31, L006625, doi: 10.1029/2003GL019231.

Gans C.R., Beck S.L., Zandt G., Gilbert H., Alvarado P., Anderson M., Linkimer L., 2011, Continental and oceanic crustal structure of the Pampean flat slab region, western Argentina, using receiver function analysis: new high-resolution results. *Geophys. J. Int.,* 186, 45–58.

Goodchild M.F., Mark D.M., 1987, The fractal nature of geographic phenomena. Annals of the Association of American Geographers 77, 2, 265-278.

Gregotski M.E., Jensen O.G., Arkani-Hamed J., 1991, Fractal stochastic modeling of aeromagnetic data. *Geophysics,* 56, 1706-1715.

Introcaso A., Pacino M.C., Fraga H., 1992, Gravity, isostasy and crustal shortening between latitudes 30° and 35° S. Tectonophysics 205, 31-48.

Jachens R.C., Moring B.C., Schruben P.G., 1996, Chapter 2: Thickness of Cenozoic deposits and the isostatic residual gravity over basement of Nevada. Nevada Bureau of Mines and Geology. Geological Survey (U.S.). Nevada Bureau of Mines and Geology, 96-2, 10 pp.

Kane M.F., 1962, A comprehensive system of terrain corrections using a digital computer. *Geophysics,* 27, 4, 455–462.

Keating P., 1993, The fractal dimension of gravity data sets and its implication for gridding. *Geophysical Prospecting. 41, 983-993.*

Mandelbrot B.B., 1967, How long is the coast of Britain? Statistical self-similarity and fractional dimension. *Science,* 156, 1967, 636-638.

Maus S., 1999, Variogram analysis of magnetic and gravity data. *Geophysics,* 64, 776-784.

Maus S., Dimri V.P., 1994, Fractal properties of potential fields caused by fractal sources. *Geophys. Res. Lett.,* 21, 891-894.

Maus S., Dimri V.P., 1996, Depth estimation from the scaling power spectrum of potential fields?, *Geophys. J. Int.,* 124, 113-120.

Miranda S., Introcaso A., 1999, Cartas gravimétricas de la Provincia de Córdoba.

Interpretación de la estructura profunda de la Sierra de Córdoba. *Temas de Geociencia 1.* Publicación UNR Editora, Universidad Nacional de Rosario, Argentina, 47 pp.

Nagy D., 1966, The gravitational attraction of a right rectangular prism. *Geophysics,* 31, 2), 362-371.

Nettleton L.L., 1939, Determination of density for the reduction of gravimeter observations. *Geophysics,* 4, 176-183.

Oyhantçabal P., Siegesmund S., Wemmer K., 2011, The Río de la Plata Craton: a review of units, boundaries, ages and isotopic signature. *Int. J. Earth Sci. (Geol Rundsch)* 100, 201–220.

Pacino M.C., 2007, Absolute Gravity Measurements and Gravity Networks in South America. *Nordic Journal of Surveying and Real Estate Research,* 4, 2, 59-69.

Parker R.L., 1972, The rapid calculation of potential anomalies. *Geophysical Journal of the Royal Astronomical Society,* 31, 447-55.

Perarnau M., Gilbert H., Alvarado P., Martino R., Anderson M., 2012, Crustal structure of the Eastern Sierras Pampeanas of Argentina using high frequency local receiver functions. *Tectonophysics,* 580, 208-2017.

Pilkington M., Keating P., 2012, Grid preparation for magnetic and gravity data using fractal fields. *Nonlin. Processes Geophys.,* 19, 291–296.

Pilkington M., Todoeschuck J.P., 2004, Power-law scaling behavior of crustal density and gravity, *Geophys. Res. Lett.,* 31, L09606, doi:10.1029/2004GL019883.

Pilkington M., Todoeschuck J.P., 1993, Fractal magnetization of continental crust. *Geophys. Res. Lett.,* 20, 627-630.

Prezzi C.B., Götze H.J., 2009, Estructura litosférica de los Andes centrales a partir de un modelo gravimétrico 3D. *Rev. Asoc. Geol. Argent.*, 65, 1 , 081-096.

Quarta T., Fedi M., Santis A.D., 2000, Source ambiguity from an estimation of the scaling exponent of potential field power spectra. *Geophys. J. Int.,* 140, 311-323.

Ruiz F., Introcaso A., 2011, Study of the Claromecó basin from gravity, magnetic and geoid undulation charts. Boletín del Instituto de Fisiografía y Geología, UNR, 79-81, 95-106.

Sánchez Bettucci L., Peel E., Oyhantçabal P., 2010, Precambrian geotectonic units of the Río de La Plata craton. *Int. Geol. Rev.,* 52, 32–50.

Simpson R.W., Jachens R.C., Blakely R.J., 1986, A new isostatic residual gravity map of the conterminous United States with a discussion on the significance of isostatic residual anomalies. *J. Geophys. Res.,* 91, 8348-8372.

Schmidt S., Götze H.J., 2006, Bouguer and Isostatic Maps of the Central Andes. In Oncken, O. ; Chong, G. ; Franz, G. ; Giese, P. ; Götze, H.-J. ; Ramos, V. ; Strecker, M.; Wigger, P. (Ed.): The Andes - Active Subduction Orogeny . Berlin : Springer, 2006, (Frontiers in Earth Sciences Bd. 1), 559:562.

Tankard A.J., Uliana M.A., Welsink H.J., Ramos V.A., Turic M., Franca A.F., Milani E.J., Neves B.B. de B., Eyles N., Skarmeta J., Ana H.S., Wiens F., Cirbían M., Paulsen O.L., Germs G.J.B., Wit M.J.D., Machacha, T., Miller R.M., 1995, Structural and tectonic controls of basin evolution in southwestern Gondwana during the Phanerozoic. In: Tankard, A.J., Soruco, R.S., Welsink, H.J. (Eds.), Petroleum basins of South America. The American Association of Petroleum Geologists Memoir 62, 5–52.

Tassara A., Götze H.J., Schmidt S., Hackney R., 2006. Three-dimensional density model of the Nazca plate and the Andean continental margin. .*J. Geophys. Res.,* 111, B9, B09404, doi10.1029/2005JB003976.

Thorarinsson F., Magnusson S.G., 1990, Bouguer density determination by fractal analysis. *Geophysics,* 55/7, 932-935.

Turcotte D.L., 1997, Fractals and chaos in Geology and Geophysics. 2nd. Edition. Cambridge University press, 398 pp.

Geofísica Internacional (2015) 54-4: 323-342

Original paper

# Chapala half-graben structure inferred. A magnetometric study

Miguel Angel Alatorre-Zamora*, José Oscar Campos-Enríquez, José Guadalupe Rosas-Elguera, Laura Peña-García, Roberto Maciel-Flores and Emilia Fregoso-Becerra

Received: September 16, 2014; accepted: July 29, 2015; published on line: October 01, 2015

**Resumen**

El Lago de Chapala se ubica en una gran depresión topográfica rodeada de amplias mesetas volcánicas del Mioceno medio al tardío. Muchos estudios geológicos y tectónico-estructurales se refieren a la estructura interna de esta depresión topográfica como un graben o genéricamente como rift, aunque su estructura interna no ha sido formalmente establecida. Para este fin se realizó un levantamiento magnético constituido por cinco líneas norte-sur que cruzan al Lago de Chapala. Un perfil se extiende hacia el sur sobre caminos transitables. Las anomalías magnéticas son principalmente suaves y de carácter regional, lo que se debe al relleno sedimentario; anomalías de carácter local son debidas a bloques someros inclinados de composición basáltica y andesítica, y amplitudes altas debidas a flujos de lavas basálticas expuestas en las islas de Los Alacranes y Mezcala. Los modelados indican la presencia de un alto estructural que separa dos bajos estructurales. Los bajos estructurales constituyen estructuras tipo semi-graben. A través de las fallas que delimitan este alto estructural se emplazaron los flujos basálticos de las Islas de Los Alacranes y Mezcala. La presencia de estructuras tipo semi-graben implican que la corteza ha estado sometida a una tectónica de extensión. Una extensión profunda que adelgazó la corteza podría estar en el origen de las estructuras de tipo semi-graben que caracterizan a la depresión Chapala.

Palabras clave: Rift, graben, semi-graben, depresión, Lago de Chapala, perfiles magnéticos, modelado 2D, islas basálticas, Bloque Michoacán.

**Abstract**

Many geologic and tectonic-structural studies refer to the Chapala lake structure in general terms as a graben (or more generally as rift). However, no formal study has addressed its structure. The Chapala Lake is located in a major topographic depression surrounded by broad middle to late Miocene volcanic-capped plateaus. We conducted a magnetic survey comprising five S-N lines crossing the Chapala Lake. One profile comprises a land extension (southwards along roads). Magnetic anomalies obtained are mainly smooth and large scale features associated to the sedimentary infill, local and high amplitude anomalies are due to shallow basaltic and andesitic tilted blocks, and highest amplitudes due to the outcropped basaltic flows of the Los Alacranes and Mezcala islands. The models obtained point to a large structural high located at the central depression portion that separates two structural lows. The structural lows correspond to half-graben type structures. Through the faults delimiting it were emplaced the basaltic flows of the Mezcala and Los Alacranes islands. The presence of half-graben type structures indicates that the crust has been subject to an extensional tectonic.

Key words: Rift, graben, half-graben, depression, Chapala Lake, magnetic profiles, 2D modeling, basaltic islands, Michoacán Block.

M. A. Alatorre-Zamora*
Departamento de Ingeniería Civil y Topografía
Universidad de Guadalajara
*Corresponding author: alatorre2004@hotmail.com*

L. Peña-García
R. Maciel-Flores
Departamento de Ciencias Ambientales
Universidad de Guadalajara

J. Rosas-Elguera
Centro Universitario de los Valles
Universidad de Guadalajara

O. Campos-Enríquez
Instituto de Geofísica
Universidad Nacional Autónoma de México

E. Fregoso-Becerra
Departamento de Matemáticas
Universidad de Guadalajara

## Introduction

Western continental Mexico is characterized by three rift systems intersecting some 50 km south of Guadalajara city (Figure 1) (e.g., Demant, 1981; DeMets and Stein, 1990; Pacheco *et al*., 1999). Some studies suggest that the formation and evolution of these rifts are associated to slow subduction of the Rivera Plate and some faster subduction of the adjacent Cocos Plate beneath the North American Plate (e.g., Luhr *et al*., 1985; Johnson and Harrison, 1989; Serpa *et al*., 1989; DeMets and Stein, 1990), occurring between 14.5 and 9 Ma (Miocene), although some authors (Allan, 1986; Delgado-Granados, 1993; Ferrari and Rosas-Elguera, 2000) concluded that a major Pliocenic tectonic evolution occurred between 6 and 4 Ma. The rifts are the N-S Colima Rift, the NW-SE Tepic-Zacoalco Rift, Tepic-Chapala Rift after DeMets and Stein (1990), and the E-W Chapala Rift (Nixon, 1982; Luhr *et al*., 1985; Allan 1986; Delgado and Urrutia, 1985; Allan *et al*., 1991). These rifts also controlled the volcanic activity at this region (Garduño-Monroy *et al*., 1993).

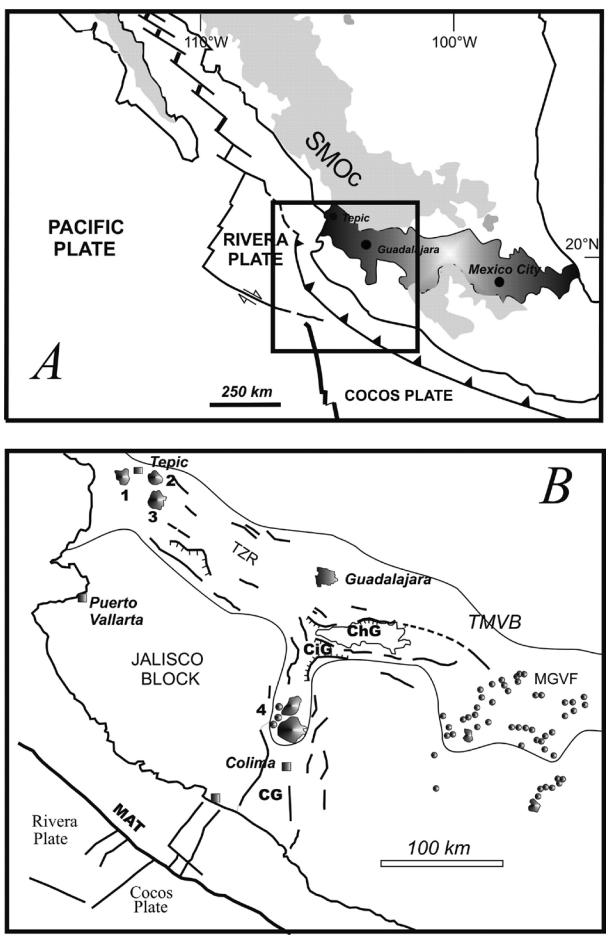


These structures act as a limit between the Sierra Madre Occidental (SMOc), made of middle Tertiary volcanic rocks (located to the north), the Mesozoic Michoacan and Jalisco Blocks (MB and JB, respectively) (located to the south), and in between the TMVB (Johnson and Harrison, 1989; DeMets and Stein, 1990; Allan *et al*., 1991; Rosas-Elguera *et al*., 1996; Campos-Enríquez and Alatorre-Zamora, 1998). Several studies report these tectonic systems as currently active (Allan *et al*., 1991; Delgado, 1992a; Michaud *et al*., 1994; Moore *et al*., 1994; Urrutia-Fucugauchi and Rosas-Elguera, 1994; Campos-Enríquez and Alatorre-Zamora, 1998), with some seismic events occurring recently (Pacheco *et al*., 1999), representing a risk factor, even if these seismic events have occurred in the NE extreme of the JB. Seismic investigations indicated the need to understand the crustal structure for the area (Pacheco *et al*., 1999), in order to have reliable understanding of the tectonic evolution of western Mexico.

The Tepic-Zacoalco rift (TZR) is constituted by a group of NNW en-echelon depressions with some lateral displacements (Demant, 1981; Luhr *et al*., 1985; Barrier *et al*., 1990; Allan *et al*., 1991; Rosas-Elguera *et al*., 1997; Campos-Enríquez and Alatorre-Zamora, 1998), with a longitude of more than 200 km (Figure 1) (Luhr and Carmichael, 1990). The Colima rift forms the eastern boundary of the JB, separating it from the Michoacan Block. Some studies extend this rift offshore, in the so-called Manzanillo Trough (Bandy *et al*., 1995). In its early stages of extensional tectonic evolution, the Colima rift could have been related to the Rivera subduction zone in the Middle America Trench (MAT, Nixon, 1982) (Figure 1).

Gastil *et al*. (1979) and Ferrari (1995) suggested that late Miocene volcanism represent the product of an important tectonic event related to the opening of the Gulf of California. Ferrari (1995) explained this volcanism in the Guadalajara region due to the WNW motion of the JB in a right-lateral transtensional zone along the boundary between the North American Plate and the JB. This WNW motion could have originated the TZR.

**Figure 1.** *A*: Tectonics and volcanics of Mexico. Dark region is the TMVB; SMOc is the Sierra Madre Occidental. Main tectonic structures are indicated. *B*: Volcanic features other than the Michoacan-Guanajuato Volcanic Field (MGVF) are: 1) San Juan Volcano; 2) Las Navajas volcano; 3) Sangangüey volcano; 4) Colima Volcanic Complex. TZR- Tepic-Zacoalco Rift; MAT- Middle America Trench; ChG- Chapala Lake; CiG- Citala Graben; CG – Colima Graben.

Studies reporting the structure of the Chapala depression are unknown. Geophysical studies have addressed the Colima rift, from its southern portion (Serpa *et al*., 1992; Urrutia-Fucugauchi and Molina-Garza, 1992; Bandy *et al*., 1993, 1995) to its central and northernmost parts (Allan, 1985; Campos-Enríquez *et al*., 1990). A gravity study made in the triple point junction area indicated the approximately depth of the basement west of the Chapala graben, and indicated sediments 800 meters thick in the Citala graben (Campos-Enríquez and Alatorre-Zamora, 1998).

The Chapala Lake is located at a wide depression that has evolved since late Miocene time (Rosas-Elguera and Urrutia-Fucugauchi, 1998); it has a length of 100 km after Luhr and Carmichael (1990), 115 km according to Rosas-Elguera and Urrutia-Fucugauchi (1998). The Pajacuaran (to the south) and the Ixtlan faults (to the north) (Figure 2) bound the eastward continuation of the Chapala depression (Figure2) (Rosas-Elguera and Urrutia-Fucugauchi, 1998; Pacheco *et al*., 1999). Its total length would then amount to almost 270 km.

Other authors consider a 400 km extension along the Chapala-Tula fault zone (Pacheco *et al*., 1999). Some studies have considered that the Chapala graben is in (or is part of) a large rift system along with the Citala graben (Delgado and Urrutia, 1985; Delgado, 1992a; Michaud *et al*., 1994). Mendoza-Cervantes *et al*. (2002) modeled a gravity profile across the Citala graben, showing possible crustal thinning in its central part. However, the complete

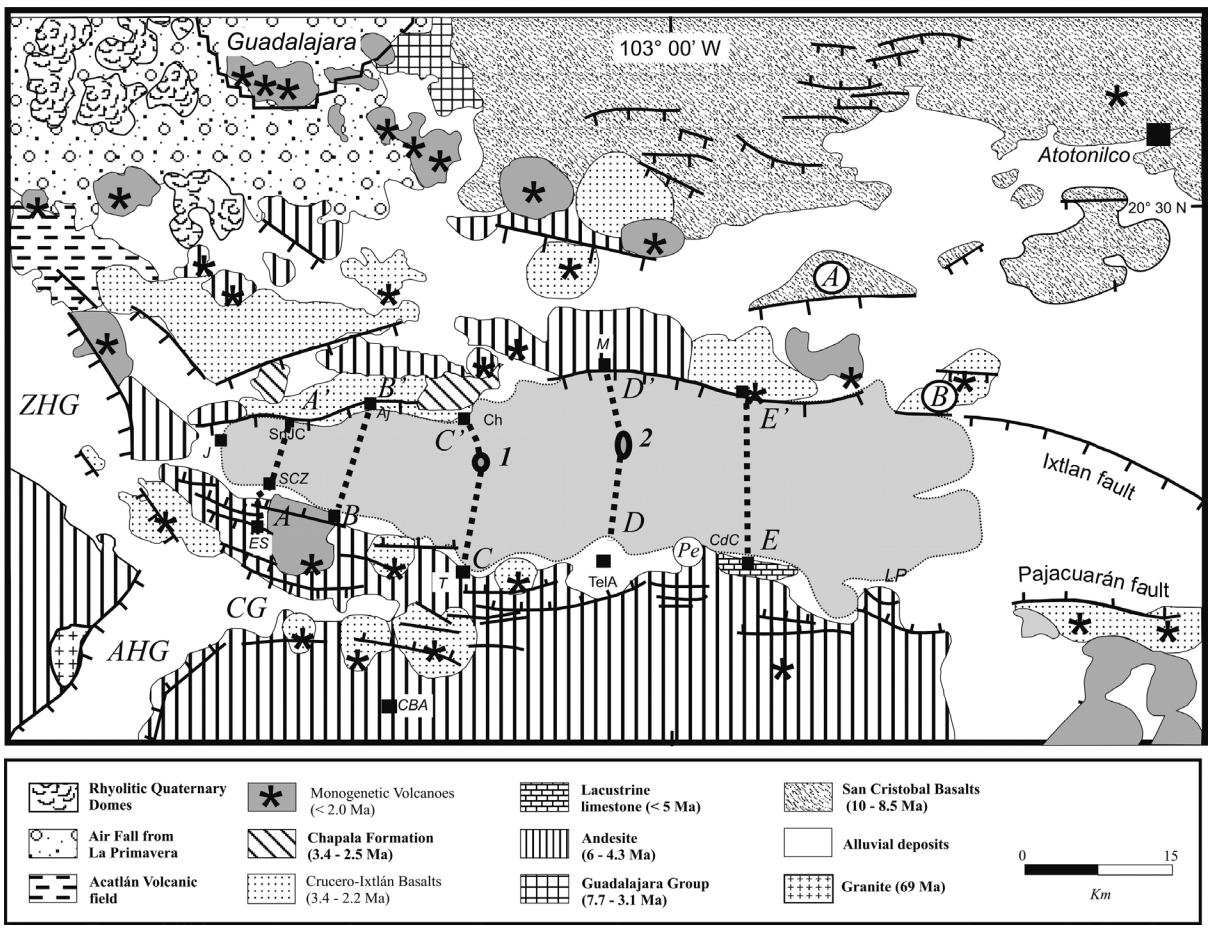


**Figure 2.** Geology of the study area. Guadalajara urban area is showed to the NW. Other villages showed with small closed black boxes and abbreviations are: SnJC - San Juan Cosalá; Ch - Chapala Village; Ch is also the magnetic base station location; TelA - Tizapán el Alto; CBA - Concepción de los Buenos Aires; T - Tuxcueca town; J – Jocotepec; M – Mezcala town; CdC – Callejón de Calera; LP – La Palma; Aj – Ajijic; ES – El Sauz; SCZ – San Cristobal Zapotitlán. ZHG- Zacoalco Half-Graben; AHG – Amacueca Half-Graben; CG – Citala Graben. *Pe* enclosed in a circle is the PEMEX exploratory oil well location. A and B are sampling points from Rosas-Elguera and Urrutia-Fucugauchi (1998). Crossing from south to north the modeled profiles are indicated. 1 and 2 indicate the Los Alacranes and Mezcala Islands, respectively (Modified from Rosas-Elguera and Urrutia-Fucugauchi, 1998).

inner structure and the crustal structure of the Chapala graben have not been established yet. A study of landward deformation could be relevant for a better definition of the Rivera–North America boundary (DeMets and Stein, 1990). In this work we analyzed five N-S magnetic profiles that were modeled to define the shallow structure of the Chapala depression, constituting a contribution for future seismic and risk studies. We use palaeomagnetic and stratigraphic information to support the magnetic models to avoid (or to decrease) their non-uniqueness and ambiguity.

As no formal study of the structure of the Chapala depression has been reported, most authors consider it in general terms as a graben (or more generally to as a rift). The knowledge of its structure is important because it provides information about the extension mechanisms operating during its formation (i.e., pure shear, or normal shear). This study was undertaken to infer the shallow crustal structure beneath the Chapala Lake. This lake is the major lake in Mexico, and is located 30 k to the southeast of Guadalajara City, at almost 1,527 meters above sea level.

**Geologic setting**

The oldest rocks around the Chapala Lake are basalts belonging to the Oligocenic SMOc, that are exposed at the NE-corner of the study area, about 30 km southwest of Atotonilco Village (site indicated with "*A*" in a circle in Figure 2) (Rosas-Elguera and Urrutia-Fucugauchi, 1998). At this site a sequence of basaltic lava flows interlayered with rhyolite and an ash-flow tuff is observed. Seven samples of these basalts and rhyolites were dated by the K-Ar method (Rosas-Elguera and Urrutia-Fucugauchi, 1998). The oldest unit yielded an isotopic age range from 13.5 to 10.8 Ma. This unit is a 400 m thick succession of basalts which overlays the SMOc ignimbrites. Several basaltic dikes trending 57° cut the basalts (Rosas-Elguera and Urrutia-Fucugauchi, 1998). An ash-flow tuff with reworked material and lacustrine sediments at its bottom overlay the basalts. A sample of the bottom of the ash-flow tuff yielded an age of 10.3 Ma.

Most common rocks are those related to the Plio-Quaternary TMVB that include basaltic breccias and basaltic andesites exposed also towards the Rio Grande de Santiago Canyon NE portion (Campos-Enriquez and Alatorre-Zamora, 1998). At the Chapala rift, together with other volcanic products, these rocks are referred as the Chapala Breccias (Garduño *et al*., 1993; Rosas-Elguera and Urrutia-Fucugauchi, 1998), comprising a succession of 500 m of volcanic breccias exposed along a fault plane dipping to the south, at the northern shore of the Chapala Lake. The absolute age of this unit is unknown but to the west of the Chapala village an andesitic lava flow dated at 3.4 Ma K-Ar rests on the volcanic breccias (Rosas-Elguera and Urrutia-Fucugauchi, 1998). The thickness of these breccias is uncertain, but an exploratory oil well (which location is indicated with "*Pe*" in a circle in the Figure 2) drilled by PEMEX, found 500 m of Pliocene basalts and andesites, after which it cut 1,848 m of volcanic breccias and agglomerates with scarce intercalated lava flows (López-Ramos, 1979). These thicknesses suggest 1,000 m of vertical offset for post-3.4 Ma breccias (Rosas-Elguera and Urrutia-Fucugauchi, 1998).

Possibly the first geologic study in the Chapala area was made by Palmer (1926), who described two basalts in the Chapala depression. The older Tizapan basalt (Palmer, 1926) is exposed on the southern edge of the lake (Figure 2). This basalt was considered Tertiary (possibly Miocene) in age. Palmer (1926) reported that lacustrine beds rest on the Tizapan basalt and that these beds are overlain by the Pleistocene Estancia basalt at Concepción de los Buenos Aires (Figure 2), near Las Caleras (Palmer, 1926).

Although most of the surroundings of the Chapala depression are dominated by volcanic features, lacustrine sediments are widespread. Palmer (1926) referred to the sediments as the Chapala beds, basing the name on the extensive exposures around the town of Chapala on the northern shore of the present lake. Within this designation he includes the beds at Chapala and elevated lake-and-swamp deposits at Tizapan, Callejon de Calera and La Palma, along the southern of the lake, and at Concepcion de los Buenos Aires, c. 40 km south of the lake (Figure 2). The beds near Chapala town were described as slightly consolidated, very light-gray and white clays, marls and fine sands, together with an occasional bed of coarse sandstone and fine arkose conglomerate (Palmer, 1926). There are also extensive beds of white, diatomaceous earth. In this locality the section is several hundred meters thick, and has a 20 degrees general dip to the northeast. There is no consistent trend in clast size from the bottom to top of the deposits, but volcanic ash is more common in the upper part of the section.

Downs (1958) referred to these beds as the Chapala Formation, and Clements (1962) expanded the definition to include lacustrine

sediments which outcrop on the Chapala – Guadalajara highway, north of the volcanic ridge which forms the present northern limit of the Chapala depression. Palmer (1926) reported the presence of fluvial sediments at the western edge of Chapala Lake. The site, denominated as Jocotepec Quarry by Smith (1980), is a sand and gravel pit about 5 km W of the town of Jocotepec (Figure 2). Both Palmer (1926) and Clements (1962) referred to deposits of tuff and pumice in their descriptions of the Chapala Formation, thereby including deposits of fluviatile sediments at Jocotepec Quarry (Smith, 1980). Clements (1962) described a thick conglomerate overlain by ash and pumice north of the lake. His description matches the upper exposures at Jocotepec Quarry.

The Chapala Formation is composed of dipping lacustrine beds exposed about 4 km N of the town of Chapala. The beds have yielded a variety of vertebrate remains (Downs, 1958) including mammals which indicate an Early Pleistocene or Late Pliocene age. Rosas-Elguera and Urrutia-Fucugauchi (1998) redefined the Chapala Formation as an N-NE tilted succession composed of an alternation of lacustrine sediments and pyroclastic units (ash and pumice), which are exposed at western and central portions of the northern lakeshore (Figure 2).

Around the Chapala depression and Chapala lakeshore a rock succession of highly varying composition occurs, being the older basaltic-andesites, calc-alkaline, and alkaline rocks dated between 6.2 to 3.5 Ma (late Miocene-early Pliocene) (Rosas-Elguera *et al*., 1997). Delgado-Granados (1992) grouped these volcanic rocks with the volcano-sedimentary deposits of the Chapala Formation (Downs, 1958; Clements, 1962) and he defined them as the Chapala Group. Rosas-Elguera *et al*. (1997) designated as Chapala Group a volcanic succession intercalated with some lacustrine deposits.

Delgado-Granados *et al*. (1995) reported a K-Ar age of 2.5 Ma for a volcano, at the northeastern corner of the Chapala Lake (site indicated with a "*B*" in a circle in Figure 2), which is correlative with the upper portion of the volcano-sedimentary sequence. Thus, the age of the Chapala Formation is bracketed between 3.5 and 2.5 Ma, and consists of almost NE-tilted volcano-sedimentary blocks.

During late Pliocene, shield and lava cones were emplaced, mainly at the southwestern and northwestern sectors of the Chapala depression (Figure 2). These volcanoes are basically composed of basaltic lavas with calc-alkaline affinity (Rosas-Elguera *et al*., 1989; Delgado-Granados, 1992), whose products, which were erupted between 3.3 and 2.5 Ma, are denominated as Crucero-Ixtlán basalts (Rosas-Elguera *et al*., 1997). At the western side, the Crucero-Ixtlan basalts overlain the Chapala breccias and underlain the Chapala Formation, but at the northeastern side, they rest on lacustrine sediments (Figure 2) (Rosas-Elguera *et al*., 1989). During this Pliocene volcanic activity, the deformation was transferred to the south and concentrated along the southern flank of the Chapala depression (Rosas-Elguera and Urrutia-Fucugauchi, 1998). The Citala graben (Delgado and Urrutia, 1985) then developed in the western axial zone.

The Quaternary is represented by widespread monogenetic volcanoes and particular volcanic fields. One of these is the Acatlan volcanic field, located to the north of the Zacoalco-half graben (Figure 2). This volcanic field is composed of several calc-alkaline rhyolitic-dacitic domes and andesitic cones and lava flows younger than 1.0 Ma (Rosas-Elguera *et al*., 1997).

The oldest Quaternary rocks of the Acatlan volcanic field are dacitic domes dated in 1.07 Ma (Delgado-Granados, 1992), which rest on the basalts of the Chapala group (Figure 2); at that time a cinder cone and associated lava flow (0.99 Ma, Venegas and Ruy, 1981) were emplaced along the main fault plane (Figure 2) indicating that the Zacoalco half graben was completely developed by this time. The Acatlán Volcanic Field is also the source of the widely known Acatlán Ignimbrite, which show evidence of mingling between a silicic and an andesitic magma (Wright and Walker, 1981; Branney and Kokellar, 2002).

**Structures and tectonics**

According to Garduño-Monroy *et al*. (1993) the Chapala tectonic depression is an aulacogen and belongs to an intra-arc regional graben and half-graben system that extend roughly E-W across central Mexico, along the Trans-Mexican Volcanic Belt (TMVB) (Figure 1). This graben and horst system has been considered as a regional structure, referred to as the Chapala-Tula fault zone (Johnson and Harrison, 1990). Regional tectonic stress patterns have evolved during late Cenozoic, and have changed from dominant left-lateral strike-slip to normal faulting (e.g., Pasquaré el al., 1988; Johnson and Harrison, 1990; Garduño-Monroy *et al*., 1993; Ferrari *et al*., 1994; Urrutia-Fucugauchi and Rosas-Elguera, 1994).

Southwest of the Chapala Lake is located the Citala graben, which extends eastward from the triple junction zone and narrows within some 30 km (Delgado-Granados and Urrutia-Fucugauchi, 1986). It is characterized by recent faulting and may represent the most active structure in the region (Pacheco *et al*., 1999).

Other faults characterize the complex Chapala-Citala grabens; especially to the north and eastern parts, are located longer faults named as Pajacuaran and Ixtlan. In these faults are located several thermal manifestations. Along the northern lake border there are three long E-W faults, one of which is Ixtlan Fault. The southern part, by the other way, especially the southwestern part, has several parallel faults oriented west-east, mainly located between Citala and Chapala tectonic depressions. A great deformation would be concentrated here.

Other factors that indicate recent tectonic activity in the Chapala depression are: a) the ~600 m of the lacustrine sequence of Chapala Formation (Delgado-Granados, 1992); b) the 900 to 1,000 m thick volcano-lacustrine sequence (Rosas-Elguera and Urrutia-Fucugauchi, 1998), which is particularly well exposed in the northern sector of the Chapala Lake; c) and the 1,848 m of volcanic breccias and agglomerates with scarce intercalated lava flows (López-Ramos, 1979) cutted by the PEMEX exploratory well that suggest a post-3.4 Ma 1,000 meters vertical offset, as was mentioned in the geology section. Campos-Enriquez *et al*. (1990) also estimated 1,000 meters of normal faulting from spectral analysis of an aeromagnetic profile oriented NNE-SSW across the Chapala Lake.

Campos-Enríquez *et al*. (1990) analyzed the shallow crustal structure in the southern Zacoalco half-graben and along the Chapala-Tula fault zone suggesting a series of large tilted blocks supporting the structural interpretation of the Zacoalco depression as a half-graben.

Rosas-Elguera and Urrutia-Fucugauchi (1998) postulated that the extensional tectonics took over and migrated progressively to the south, to form the present tectonic depression during the past 3.4 Ma.

## Data acquisition and processing

*Magnetic survey*

We conducted a marine magnetic survey in 2006 using a precession proton magnetometer G856 from Geometrics with a precision of 0.01 nT, mounted on a fiber glass boat (Figure 3). The periods were March 15, 16, and 23, and April 1. The survey comprised five roughly north-south lines (Figure 2) with measurements every 200 m approximately. The diurnal variation was monitored using a similar precession proton magnetometer in a base station settled to the south of the Chapala Village (closed black square with Ch in Figure 2), where cultural magnetic noise was avoided. Additional measurements obtained on a road, with distances between stations of almost 200 m and measuring 50 meters away from the transporting vehicle to avoid its magnetic noise (Slater and Jacyna, 2012), extended profile A-A' 4 km to the south. To obtain the total magnetic field anomaly, the D2010 International Geomagnetic Reference Field was removed. The coordinates of stations, both on land and in water, were controlled with


**Figure 3.** Surveying with the G856 precession proton magnetometer placed in the bow of a fiberglass boat.

a GPS navigator with a horizontal precision of 1 m. The measurements in the lake water body were obtained mainly in the first day half, when the windy conditions were minimum or scarce. Corrections due to the boat motor magnetic effect were not necessary, because of the measurements were performed with the engine off. Besides, the distance engine-magnetometer and the intrinsic materials of the engine (mainly cover, pistons, and propeller made of aluminum) do not give rise to an important magnetic effect. Nevertheless, we made several proofs to measure the magnetic motor effect. The maximum effect disappears at 4 m from the motor (see ADDENDUM).

The data acquired during the survey showed that the magnetic conditions were stable (or do not seem to show unstable magnetic conditions). This was verified by consulting records of solar flares and magnetic storms for the time periods of data measurements (Christian, 2008; AEG, 2015). There were neither magnetic storms nor solar flares at those periods. Magnetic measurements in Chapala Village base station to control diurnal variation also confirm this last statement (Figure 4).

The sensor was oriented in each station to the north with the help of a Brunton compass.

*Models obtained with Talwani's technique*

The modeling was made with the GM-SYS magnetic software that applies Talwani's classic method (Talwani, 1965). To constrain our models we taken magnetic susceptibilies and magnetizations from literature, and own palaeomagnetic data. Table I shows data used for the rock bodies in the models.

**Table 1.** Magnetic susceptibilities (CGS units) used for the rocks of the models.

| ROCKS | Range of Magnetic Susceptibility |
|---|---|
| Lacustrine Sediments | $1x10^{-5}$ |
| Basaltic flows | $1x10^{-3}$ to $1x10^{-2}$ |
| Chapala Group | $3x10^{-3}$ to $7x10^{-3}$ |
| Andesites | $2.5x10^{-3}$ to $1x10^{-2}$ |
| Rhyolitic breccias | $1x10^{-3}$ to $3x10^{-3}$ |
| Upper Crust | $1x10^{-4}$ |

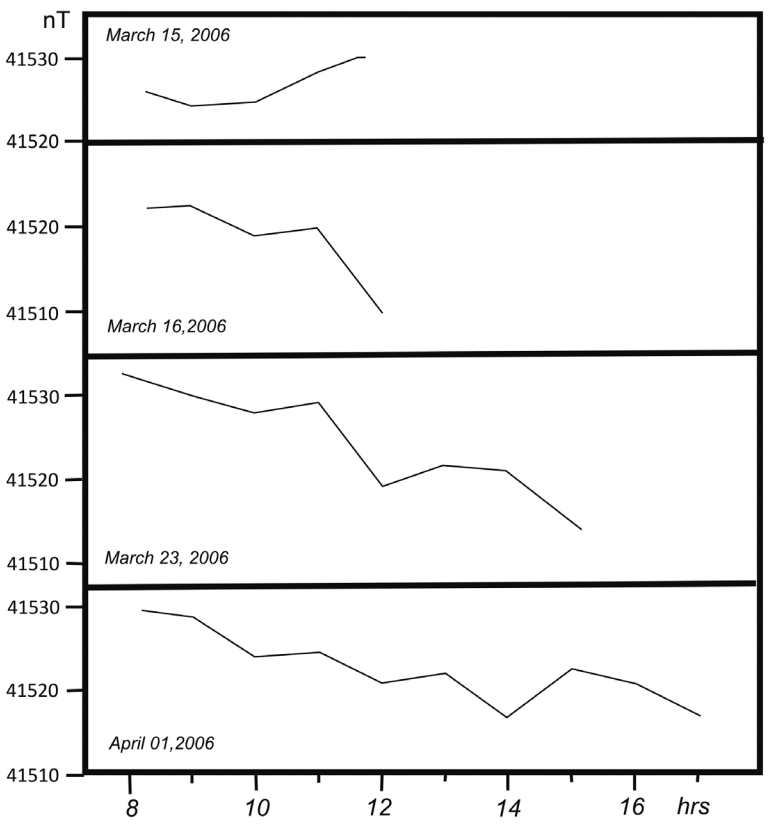


**Figure 4.** Base station magnetic data measured each hour to control the diurnal variation. This base station is located to the south of the Chapala Village (indicated with a small closed box and the letters Ch in the Figure 2).

## Results and discussion

*Magnetic anomalies*

Along the south-to-north profiles the magnetic anomaly behavior changes from west to east across the Chapala Lake. Conspicuous high amplitude small-scale magnetic anomalies are associated with the basaltic andesites that outcrops along the southernmost 4 km of the profile A-A', and to the Mezcala and los Alacranes basaltic Island (profiles C-C' and D-D') (Figures 5c, 5d, and 5a, respectively). Profile B-B' is smooth over a major portion (Figure 5b). Profile E-E' has small-scale anomalies mounted on a regional component (Figure 5e).

Several major features appear in the magnetic anomalies across the Chapala Lake. From west to east these are: a) large smooth anomalies dominate at the northwestern part of the lake; b) small-scale-high-amplitude anomalies are associated with basaltic flows of Los Alacranes and Mezcala Islands (Figures 5c and 5d). The Los Alacranes Island is associated with a positive anomaly (profile C-C') whereas the anomaly in Mezcala Island (profile D-D') is totally negative.

In particular, we observe that: a) profile A-A' shows amplitude near to 300 nT, with a minimum of approximately -100 nT inside the Lake (Figure 5a). This profile includes approximately 4 km of measurements on land along a road, over outcropping basaltic rocks. These small-scale anomalies are of local character since they are not observed in the contiguous profile B-B'; b) profile B-B' is composed of a large amplitude negative anomaly to the south and a large amplitude positive anomaly to the north. The total amplitude change is about 500 nT (Figure 5b); c) Profile C-C', that crosses the Los Alacranes Island, is basically high frequency in nature, with an amplitude of 500 nT as well (Figure 5c); d) Profile D-D' shows the largest amplitude, with a minimum near to -2500 nT and a maximum near to 1000 nT, for a total amplitude of 3500 nT; this is due to the basaltic spill of the Mezcala Island (Figure 5d); e) Profile E-E' is similar to profile B-B', with a negative anomaly at its southern portion (Figure 5e).

*Modeled profiles*

Traditionally normal faults have been considered as straight structures; however, seismic evidences do not support this idea.

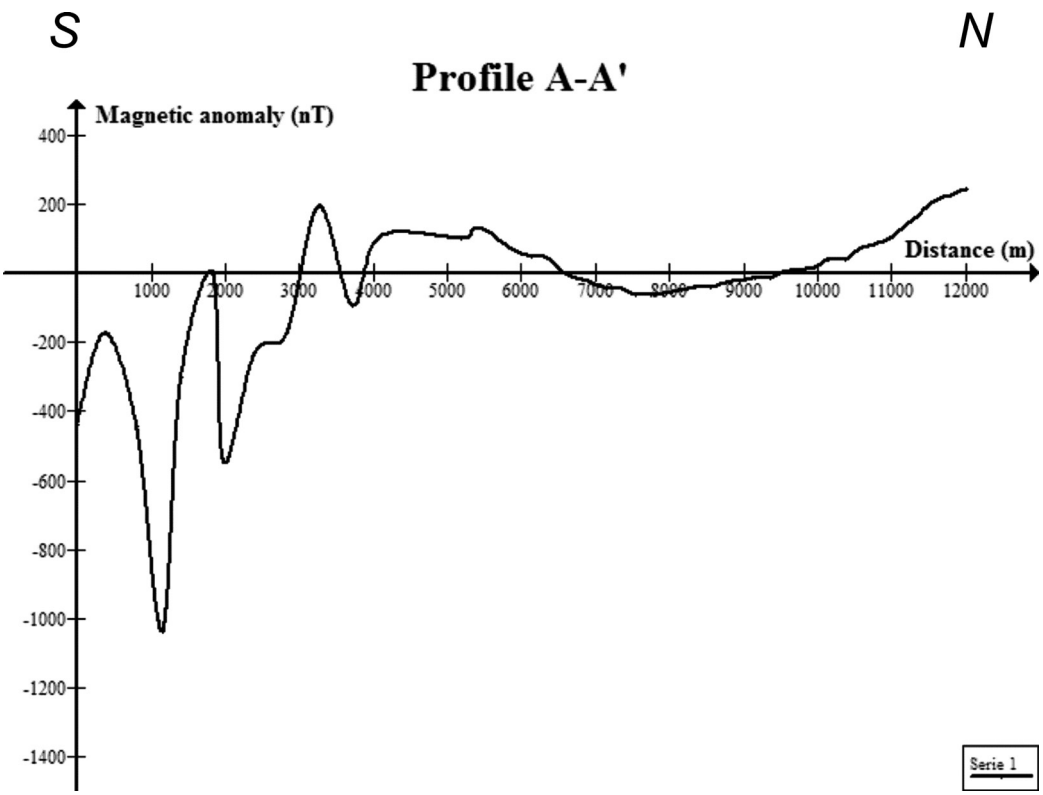


**Figure 5A.** Magnetic anomalies along profile A-A'. Location is indicated in the Figure 2.

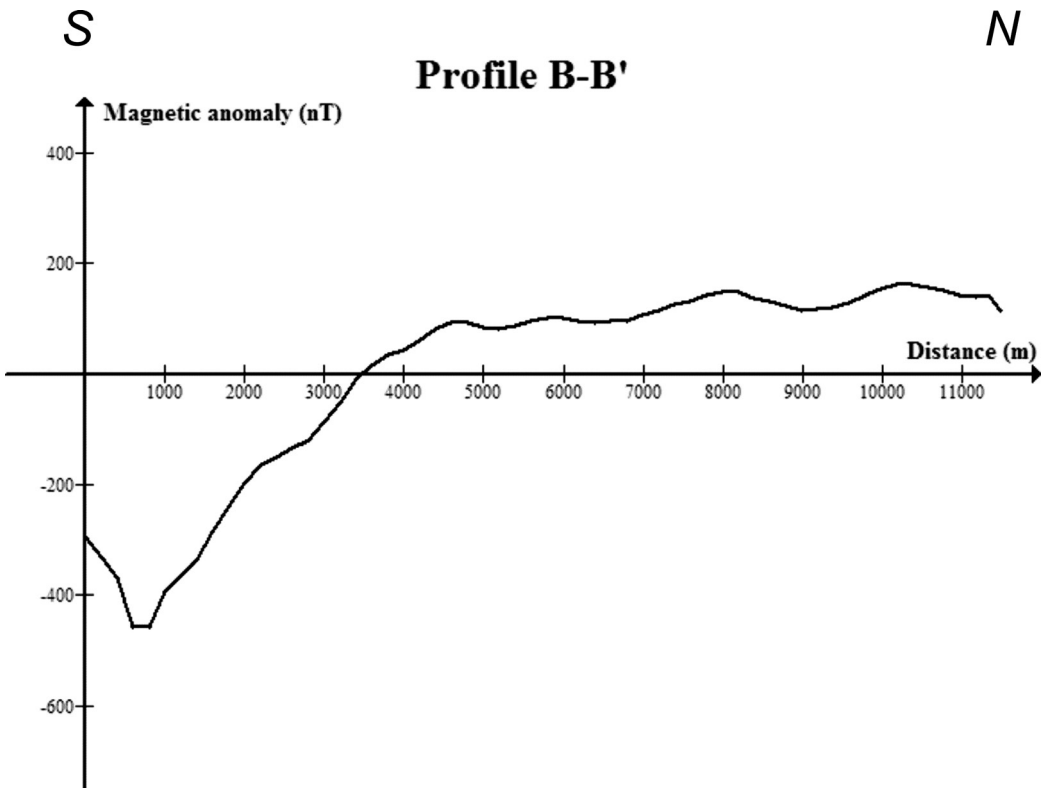


**Figure 5B.** Magnetic anomalies along profile B-B'. Location is outlined in the Figure 2.

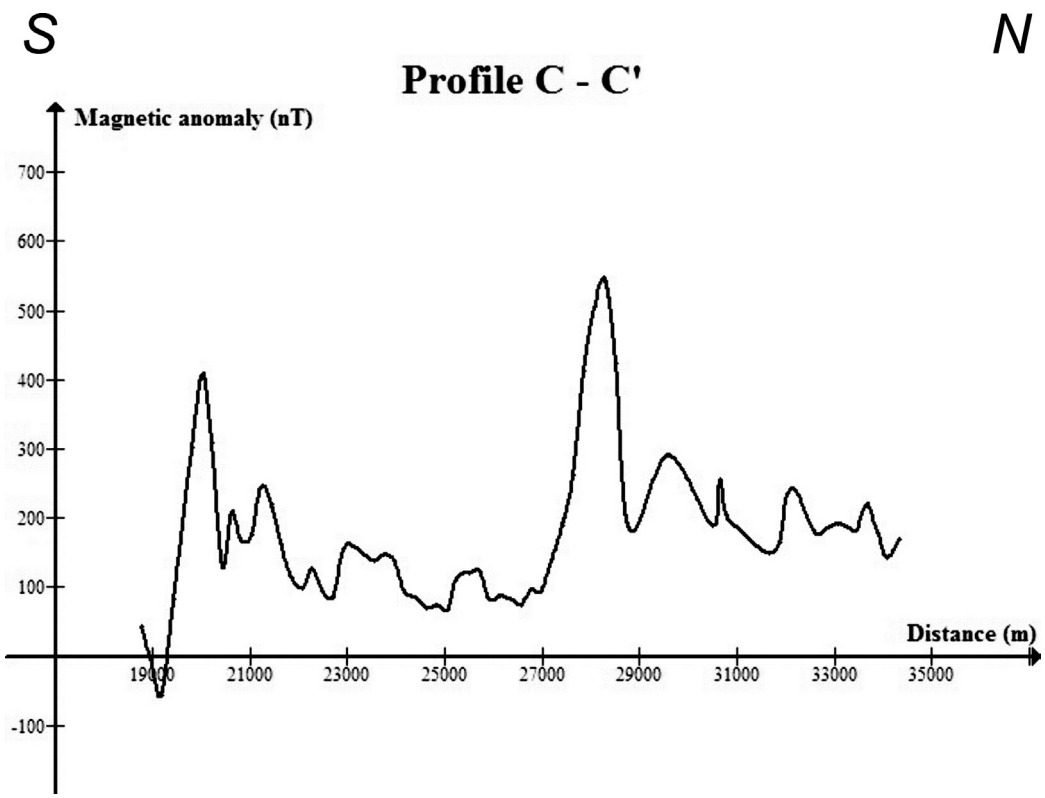


**Figure 5C.** Magnetic anomalies along profile C-C'. Position indicated in the Figure 2.

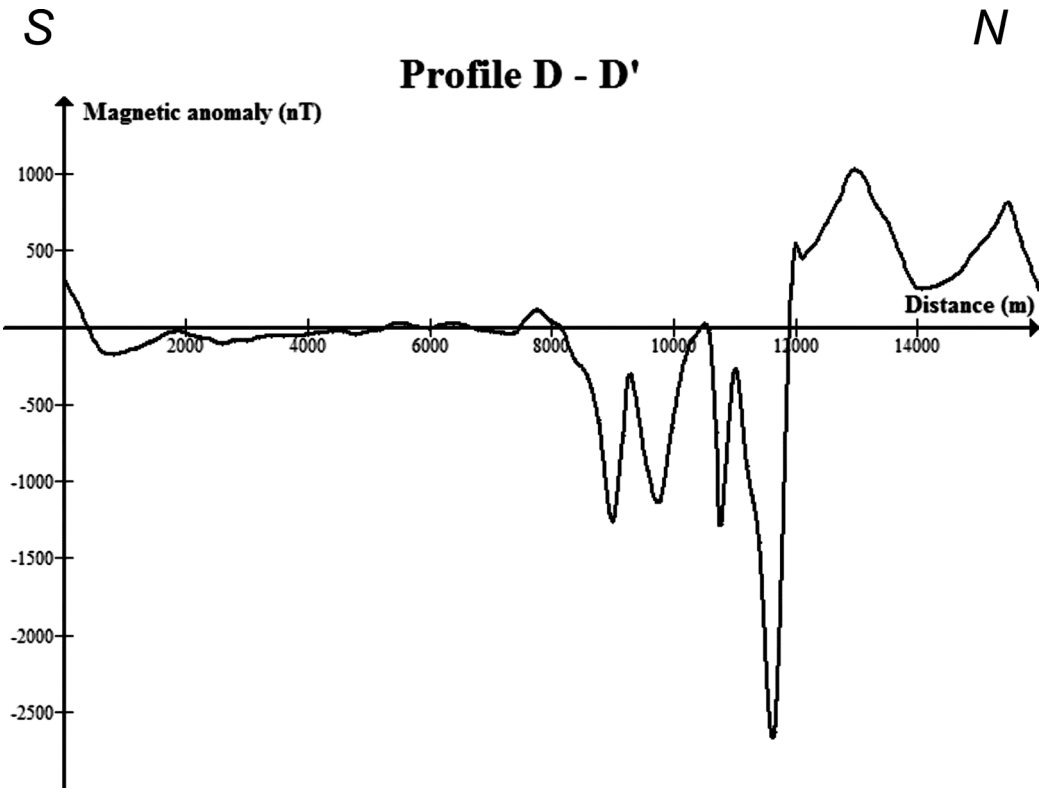


**Figure 5D.** Magnetic anomalies along profile D-D'. Location outlined in the Figure 2.

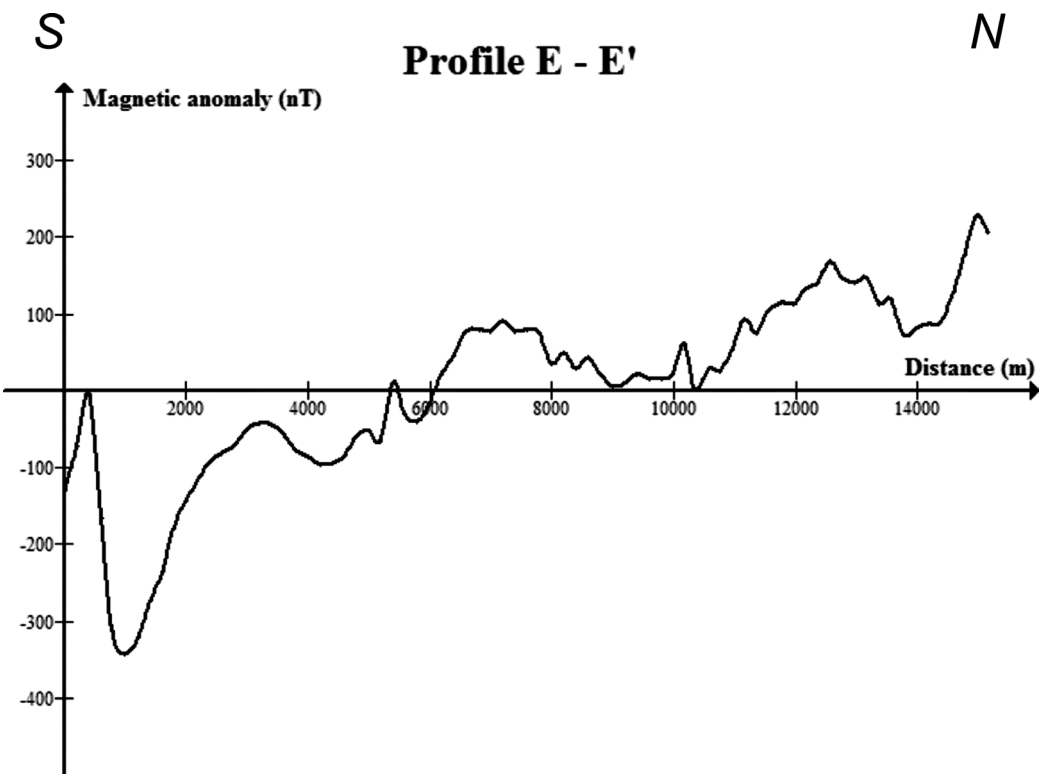


**Figure 5E.** Magnetic anomalies along profile E-E'. Position indicated in the Figure 2.

At present it is evident that straight faults are relatively rare. Listric faulting and rotated faults associated with systems of tilted blocks are more common. The rotation of blocks in extensional areas requires either a curved fault or substantial internal deformation of the hanging wall block (Wernicke and Burchfiel, 1982). Scale-experiments has shown that ratio between rates of sedimentation and deformation lead fault curvature, thus listric faulting could be explained by combination of domino-sedimentation processes, initial curvature, progressive compaction, and deformation of the fault plane due to salt or shale diapirism (Vandeville and Cobbold, 1988). However, domino-sedimentation processes needs a plastic bed or internal deformation at gaps-detachment. Because plastic beds or internal deformation could be absent in Chapala area, modeling assumes that fault shapes are listric in nature.

In general, all models present a similar stratigraphy, with four layers and some local basaltic flows and bodies. The basement is formed of Cretaceous granite (Michoacan Block), covered by SMOc rhyolitic breccias (Miocene-Oligocene), TMVB basaltic andesites (Pliocene) and lacustrine sediments (Quaternary). Susceptibilities and magnetizations used for each body were taken from the literature and other palaeomagnetic studies (Campos-Enríquez *et al*., 1990; Rosas-Elguera and Urrutia-Fucugauchi, 1998) (Table I). The thicknesses for all the geologic units, except for the granitic basement, were obtained from the PEMEX exploratory well (Figure 2), and considered for all the models. In almost all cases lateral variability of susceptibilities was considered, mainly for the rocks of the SMOc and the TMVB. Models obtained from these five profiles are described below:

**Model A-A'**. The magnetic model runs from El Sauz town, in the south, crossing San Cristobal Zapotitlán in the southern shorelake, through the lake western portion, up to the San Juan Cosalá town (Figure 6). A

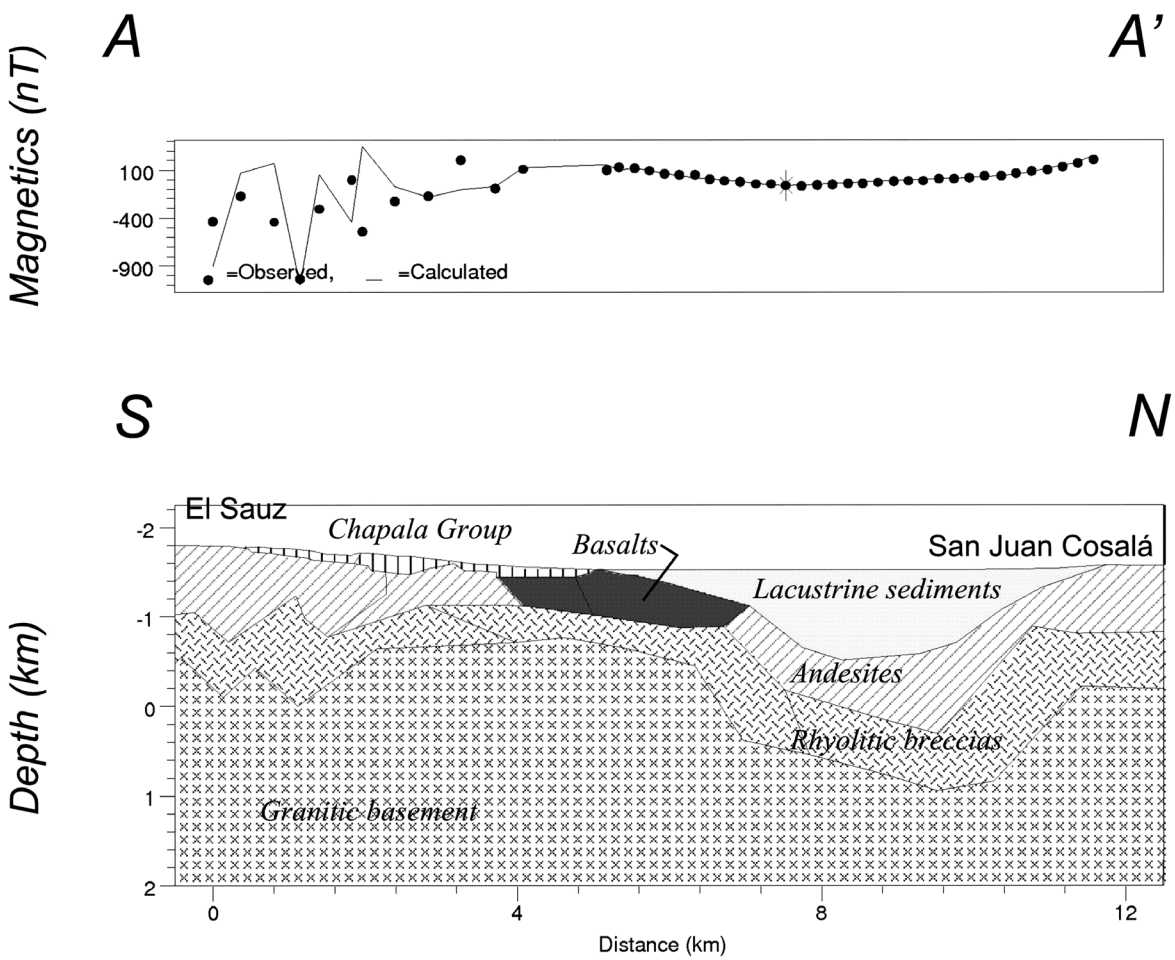


**Figure 6.** Magnetic profile A-A' and its model. Its position is marked in Figure 2.

symmetric depression is observed in the centre of the model. The structure of this modeled section approaches a symmetric graben type structure. The volcano-sedimentary infill has a thickness of almost 1,200 meters, coincident with results in other studies (e.g., Campos-Enriquez *et al*., 1990). To the south, on the profile land part, faulted basalts of the Chapala Group rest directly on rhyolitic breccias. These basalts might have been emplaced through the southern depression master fault. Faults downward displace the granitic basement. The upper granitic crust on the southern side is shallower than in the northwest (Figure 6).

**Model B-B'**. This model starts at San Luis Soyatlán at the southern shore ending at Ajijic in the north shore (Figure 7). The model shows a clearly asymmetric depression, with a depocenter located to the south. This depression is offset some 6 km to south with respect to that of the previous model. The basement has a very gentle slope in the northern model portion, and then a slope break marks the beginning of a listric fault featuring the southern depression filled with SMOc rhyolitic breccias, with the Chapala Group basaltic rocks and with approximately 2.2 km of sediments. The model shows an average thickness of 800 m of lacustrine sediments along the northern portion. The granitic basement is located about 4,500 m beneath the sea level. The northern master fault changes in attitude (i.e., in dip).

**Model C-C'.** This profile crosses the lake from Tuxcueca at the southern shore, to Chapala Village in the north, and includes the basaltic Los Alacranes Island (Figure 8). The existence of a graben or half-graben type structure is not so clear. A relative structural high is observed beneath Los Alacranes Island. To the north and south of this structural high there are two

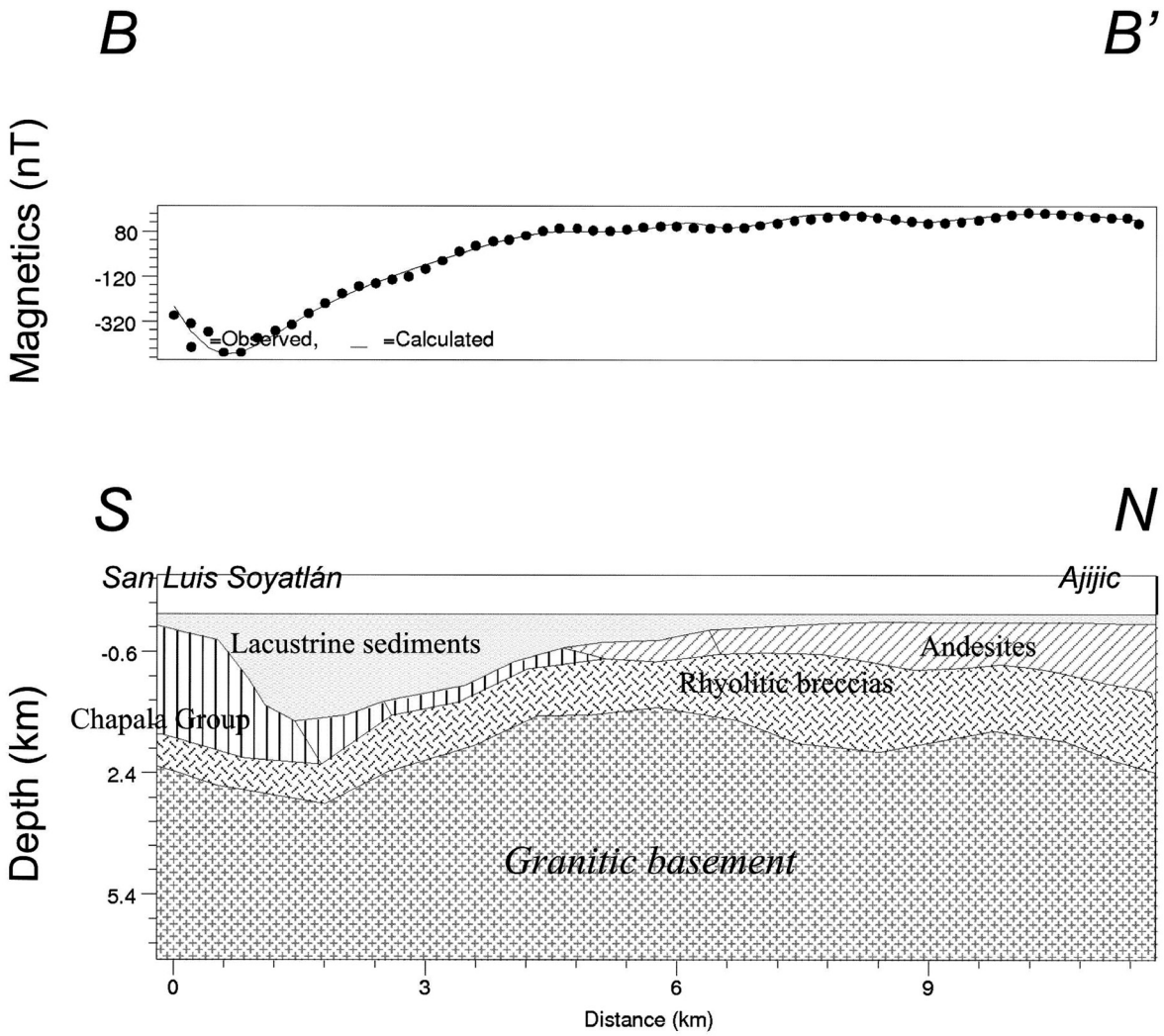


**Figure 7.** Magnetic profile B-B' and its model. Position of profile is indicated in Figure 2.

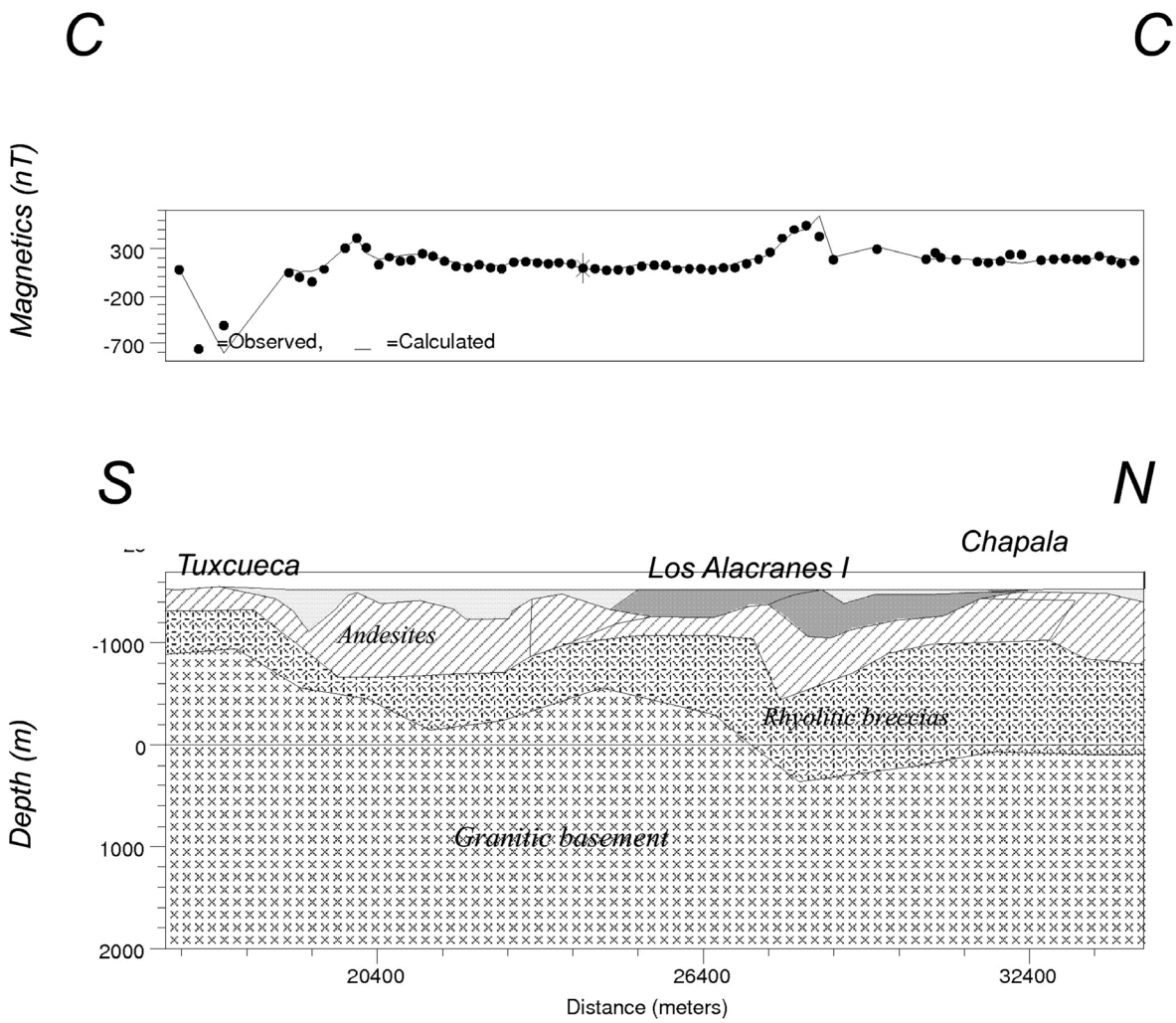


**Figure 8.** Magnetic profile C-C′ and its model. Location is indicated in the Figure 2.

shallow depressions. The sediment infill in the northern depression is very thin. Contrastingly, the thickness of the SMOc rhyolites is larger pointing to the existence of a paleo-depression. The lacustrine Quaternary deposits in the southern depression reaches 400 meters in average. The basalts forming the Los Alacranes Island might be emplaced through the northern fault delimiting this structural high. The granitic basement deepens northwards.

**Model D-D'**. This magnetic model stretches from Tizapán el Alto, to the south, up to the Mezcala Village to the north (Figure 9). It cuts, in the middle part, the basalts of the Mezcala Island. This model is featured by a structural high (to the north) and a large depression (to the south). The lacustrine sediments reach a thickness of almost 1100 m. The structural high is decomposed into two relative structural highs, being clearer in the granitic basement: one in the centre of the model and the other one in the northern part. The north-dipping fault delimiting to the north the central structural high might have controlled the emplacement of the Mezcala Island basaltic spill. The dip of this fault is subvertical (Figure 9) and contrasts with the subhorizontal attitude in the previous and following profiles (i.e., south of the los Alacranes Island; Figures 8 and 10).

**Model E-E'.** The easternmost profile crosses the water body from Callejón de Calera at the southern lake limit to La Zapotera, at the northern shore (Figure 10). The model approaches a half-graben, with the major depocenter to the south. The lake bottom deeps southwards. However, its topography is not even. Two slight depressions are observed along the lake bottom: one near to the north

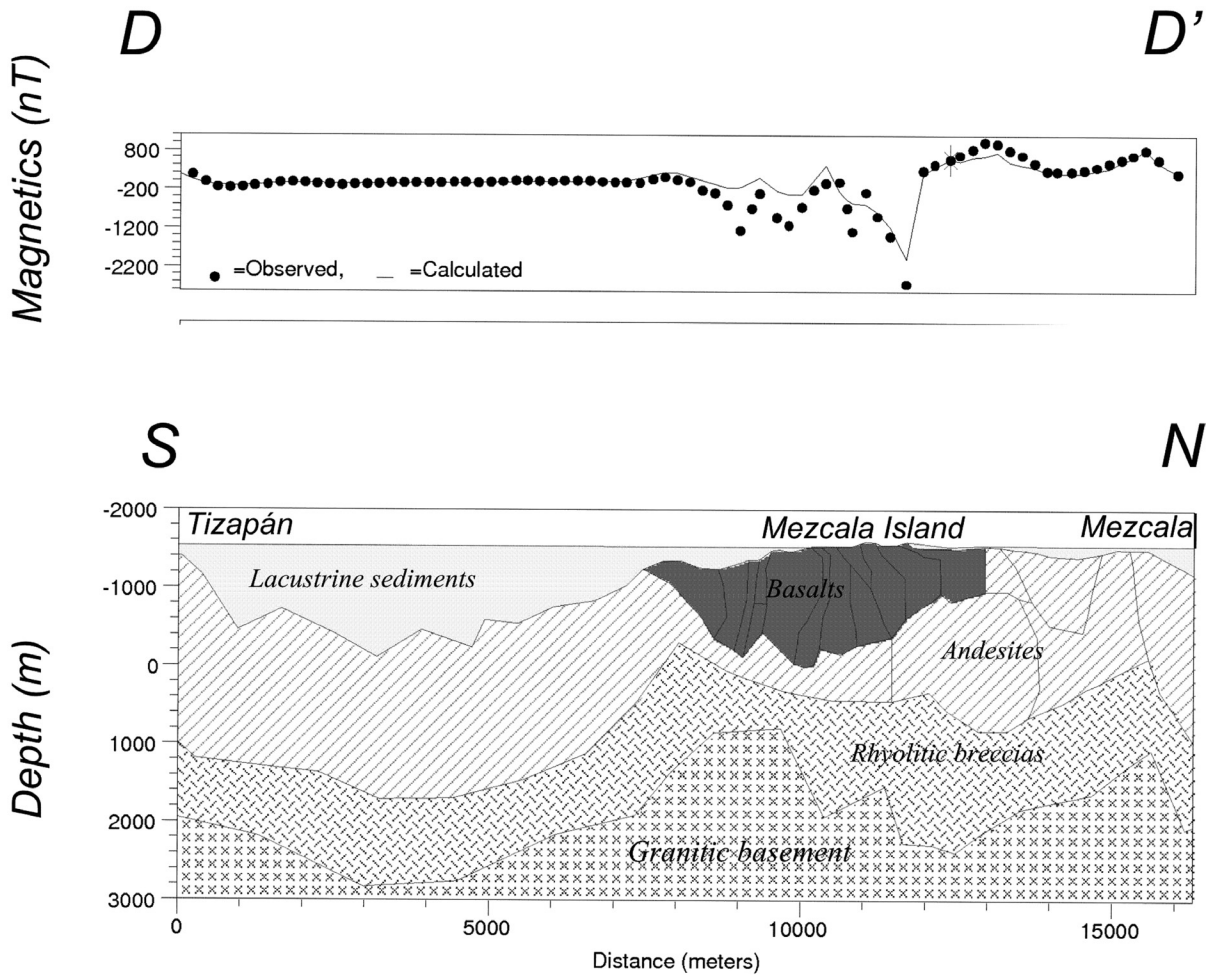


**Figure 9.** Magnetic profile D-D' and its model. Location of this model is indicated in Figure 2.

of the major depression, and a second one being the northernmost of the model (Figure 10). These small depressions indicate the presence of faults. Basaltic andesites and rhyolitic breccias fill this depression. The lacustrine sedimentary thickness reaches 400 meters in average. An andesitic deposit fills the depression along all the profile; therefore, the depression is older than the andesitic volcanic emission.

*Interpretation of modeled profiles*

The five models show differences in structural style. According to the models the Chapala lake depression is complex (Figure 11). There is a depression which is not continuous, there are two structural lows separated by a structural high in the middle portion (comprising profiles B-B', C-C', and D-D', i.e., the Los Alacranes and Mezcala islands).

The outlined depression is filled with SMOc and TMVB products. In general, the lacustrine sediments get thicker from east to west.

It is clear that the two depressions do not correspond to a graben type structure but they approximate more to a half-graben type structures. As can be observed in the geologic map, south and north of the middle lake portion, where the structural high was inferred, the faults are not continuous but interrupted.

The depression disappears to the west, where the master faults tend to join together.

It seems that the western portion of the Chapala depression is affected by NW-SE faults of the Tepic-Zacoalco rift. The structural high might correspond to an accommodation zone, to the east of which effects of NW-SE tectonic system are lesser. Half-graben structures imply

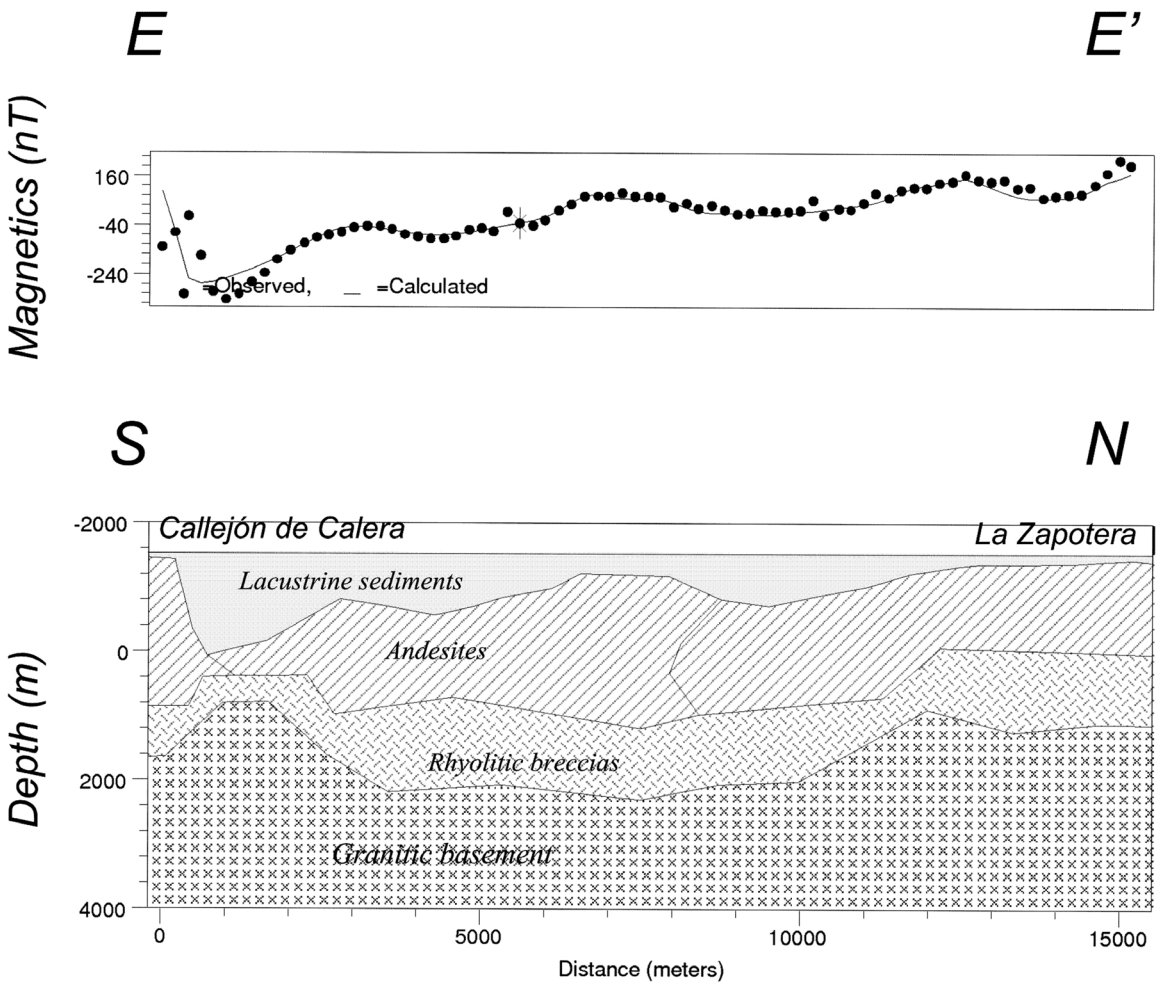


**Figure 10.** Magnetic profile E-E' and its model. Location of profile indicated in Figure 2.

that the crust was subject to an extensional tectonics that thins the crust. Campos-Enriquez and Garduño-Monroy (1995) already indicated that western TMVB has a thinned crust.

## Conclusions

The models indicate in general a complex structure. In general, listric faults conforms the northwestern shoulder, whereas normal faults constitute its southern limit. These faults are roughly E-W oriented. In detail, the models show at each sector changes of structural types. For example, there is an approximately symmetric graben at the western sector (profile A-A') that changes to a half-graben type structure to the east (profile B-B'), then a structural high (profiles B-B', C-C', and D-D'), and then a wider depression (profiles D-D' and E-E').

The western and eastern depressions are deeper to the south. In the southern part, these depocenters are limited by normal north dipping faults. At its northern limit, the Chapala depression is delimited by north-tilted andesitic blocks. The basaltic lavas of the Los Alacranes and Mezcala Islands might have been emplaced through the faults delimiting the central structural high. The existence of half-graben type structures indicates that the crust was subject to an extensional tectonics.

A deep-seated extension (i.e., Wernicke *et al*., 1982) that thinned the crust might be at the origin of the half-graben type structures featuring the Chapala depression.

## Acknowledgements

The authors are indebted to Universidad de Guadalajara Limnology Institute, for a strong support to conduct the magnetic survey at the Chapala Lake.

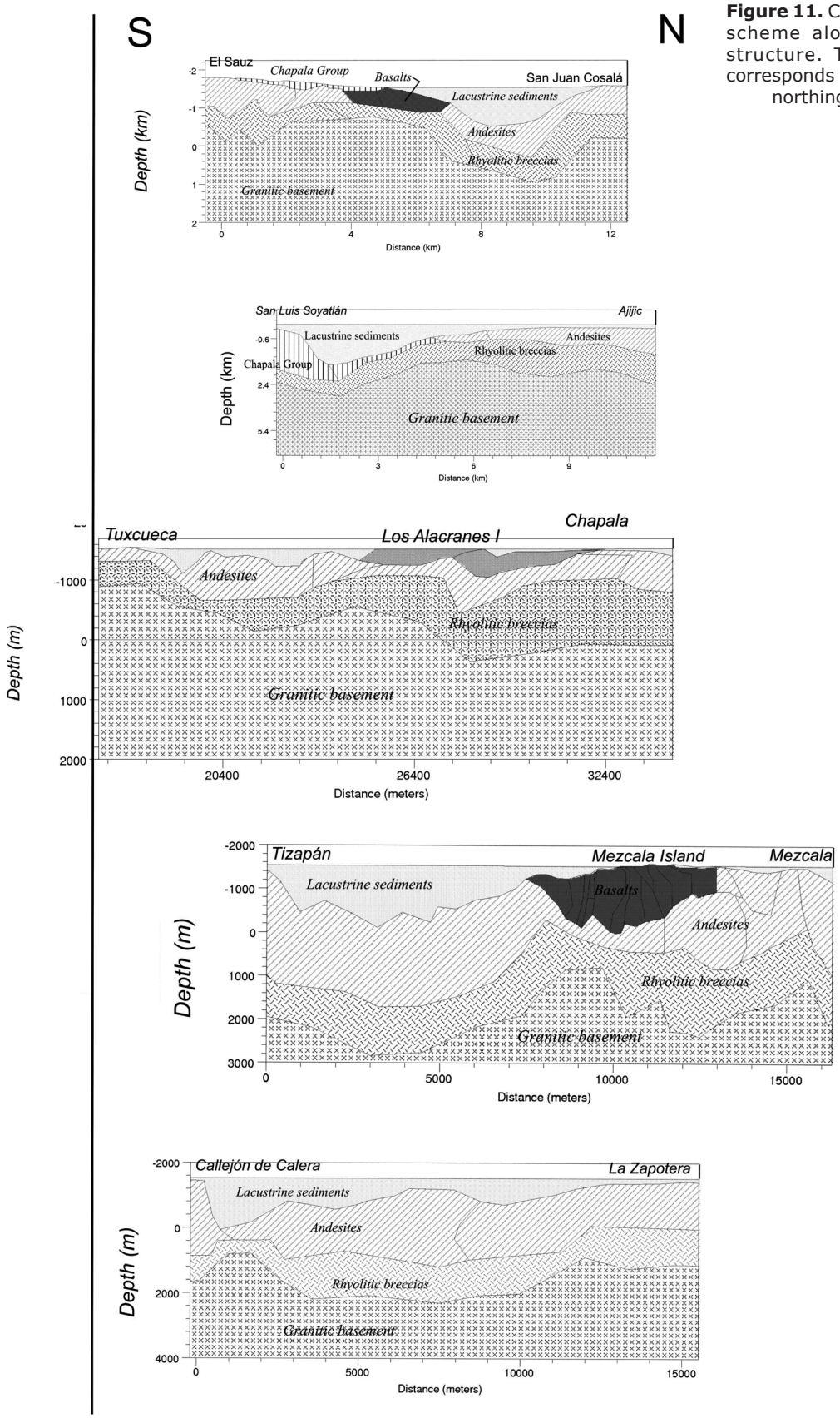


**Figure 11.** Composite modeled scheme along the Chapala structure. The vertical line corresponds to the 2228500 m northing coordinate.

## References


Allan J.F., 1985, Sediment depth in the northern Colima graben from 3-D interpretation of gravity. *Geofísica Int*ernacional, 24, 1, p. 21-30.

Allan J.F., 1986, Geology of the Colima and Zacoalco grabens, SW Mexico: Late Cenozoic rifting in the Mexican Volcanic, *Bol. Geol. Soc. Amer. Bull*.

Allan J.F., Nelson S.A., Luhr J.F., Carmichael I.S.E., Wopat M., Wallace P.J., 1991, Pliocene-Recent rifting in SW Mexico and associated volcanism: An exotic terrane in the making, in Dauphin, P.J., and Simoneit, B.R.T., eds., The Gulf and peninsular province of the Californias: *Amer. Assoc. Petrol. Geol. Mem*., 47, p. 425-445.

Astro Event Group, 2015, Top 50 geomagnetic storms. http://www.spaceweatherlive.com/en/auroral-activity/top-50-geomagnetic-storms.

Bandy W., Mortera-Gutierrez C., Urrutia-Fucugauchi J., 1993, Gravity field of the southern Colima graben, Mexico. *Geofísica Internacional*, 32, p. 561-567.

Bandy W., Mortera-Gutierrez C., Urrutia-Fucugauchi J., Hilde T.W.C., 1995, The subducted Rivera-Cocos plate boundary: where is it, what is it, and what is its relationship to the Colima rift. *Geophys. Res. Lett*., 22, p. 3075-3078.

Barrier E., Bourgois J., Michaud F., 1990, Le système de rifts actifs du point triple de Jalisco: vers un proto-golfe de Jalisco, C.R. *Acad. Sci. Paris*, t 310, Sèrie II. p. 1513-1520.

Branney M., Kokelaar P., 2002, Pyroclastic density currents and the sedimentation of ignimbrites. *Geological Society of London, memoirs*, 27, pp. 152.

Campos-Enríquez J.O., Arroyo-Esquivel M.A., Urrutia-Fucugauchi J., 1990, Basement, Curie isotherm and shallow-crust structure of the Trans-Mexican Volcanic Belt, from aeromagnetic data, *Tectonophysics*, 172, p.77-90.

Campos-Enríquez O., Garduño-Monroy V.H., 1995, Los Azufres silicic center (Mexico)-inference of caldera structural elements from gravity, aeromagnetic and geoelectric data: *Journal of Volcanology and Geothermal research*, 67, p. 123-152.

Campos-Enríquez J.O., Alatorre-Zamora M.A., 1998, Shallow crustal structure of the junctions of the grabens of Chapala, Tepic-Zacoalco and Colima, Mexico. *Geofísica Internacional*, 37, p. 263-282.

Christian E.R., 2008, COSMICOPIA, an abundance of cosmic rays. http://helios.gsfc.nasa.gov/flarenews.html#2006.

Clements T.D., 1959, Chapala formation, Jalisco, Mexico [abs.]: *Geol. Soc. Amer. Bull*., 70, p. 1713.

Clements T.D., 1962, Pleistocene history of Lake Chapala, Jalisco, Mexico: *Geol. Soc. Amer. Spec. Pap*., 68, p. 15.

Delgado G.H., Urrutia J., 1985. Estructura del graben de Chapala. Memorias de la Reunión Anual de la Unión Geof. Mex., pp. 252-260.

Delgado-Granados H., Urrutia-Fucugauchi J., 1986, Tectónica cuaternaria del Lago de Chapala. VIII Convención Geológica Nacional. Resúmenes, 18-19.

Delgado G.H., 1992a, Importancia de los estudios estratigráficos en la FVT para la comprensión de su evolución y origen: el caso del grupo Chapala. *GEOS, Bol. UGM*, 12, 5-13.

Delgado-Granados H., 1992, Geology of the Chapala rift, Mexico, PhD. Thesis, Inst. Geol. Paleontology, Tohoku Uni., Japan.

Delgado-Granados H., 1993, Late Cenozoic tectonics off-shore western Mexico and its relation to the structure and volcanic activity in the western Trans-Mexican Volcanic Belt. *Geofísica Internacional*, 32, p. 543-559.

Delgado-Granados H., Urrutia-Fucugauchi J., Hasenaka T., Ban M., 1995, Southwestward volcanic migration in the western Trans-Mexican Volcanic Belt during the last 2 Ma: *Geofísica Internacional*, 34, p. 341-352.

Demant A., 1981, L'axe néo-volcanique transmexicain. Etude volcanologique et petrographique. Signification géodynamique. Thèse Doctorat d'Etat, Univ. Aix. Marseille, 203 pp.

De Mets C., Stein S., 1990, Present-day kinematics of the Rivera Plate and implications for tectonics in southwestern Mexico, *J. Geophys. Res*., 95, p. 21931-21948.

Downs T., 1958, Fossil vertebrates from Lago de Chapala, Jalisco, Mexico. XX Inter. Geol. Cong. Mexico, 73-77.

Ferrari L., Pasquaré G., Venegas S., Castillo D., Romero F., 1994, Regional tectonics of western Mexico and its implications for the northern boundary of the Jalisco Block: *Geofísica Internacional*, 33, p. 139-151.

Ferrari L., 1995, Miocene shearing along the northern boundary of the Jalisco block and the opening of the southern Gulf of California: *Geology*, 23, p. 751–754.

Ferrari L., Rosas-Elguera J., 2000, Late Miocene to Quaternary extension at the northern boundary of the Jalisco block western Mexico: the Tepic-Zacoalco rift revised, Boulder CO, *Geol. Soc. of Amer.,* Special Paper 334, Chapter 3, p. 41-64.

Garduño-Monroy V.H., Spinnler J., Ceragioli E., 1993, Geological and structural study of the Chapala rift, State of Jalisco, Mexico. *Geofísica Internacional*, 32, p. 487-499.

Gastil R.G., Morgan G.J., Krummenacher D., 1979, Mesozoic history of peninsular California and related areas east of the Gulf of California, in Howell, D. G., and McDougall, K. A., eds., Mesozoic paleogeography of the western United States: Pacific Section, Society of Economic Paleontologists and Mineralogists, Pacific Coast Paleogeography Symposium 2, p. 107–115.

Johnson C.A., Harrison C.G.A., 1989, Tectonics and volcanism in central Mexico: A Landsat Thematic Mapper perspective, Remote Sens. Envir., 28, 273-286.

Johnson C.A., Harrison C.G.A., 1990, Neotectonics in Central Mexico, *Phys. Earth Planet Inter.*, 64, p. 187-210.

Lopez-Ramos E., 1979, Geología de México, Tomo III, 2nd ed.: Mexico City, Secretaría de Educación Pública, 446 p.

Luhr J.F., Nelson S.A., Allan J.F., Carmichael I.S.E., 1985, Active rifting in southwestern Mexico: manifestations of an incipient eastward spreading-ridge jump. *Geology*, 13, 54-57.

Luhr J.F., Carmichael I.S.E., 1990, Geology of Volcán de Colima, Universidad Nacional Autónoma de México, Instituto de Geología, Boletín 107, 101 p.

Mendoza-Cervantes K., Mortera-Gutiérrez C.A., Bandy W.L., Urrutia-Fucugauchi J., 2002, Modelos gravimétrico de la estructura del graben de Citala, Jalisco, México. *GEOS*, 22, p. 148.

Michaud F., Bourgois J., Parrot J.F., Taud H., Kasser M., 1994, Le point triple de Jalisco (Mexique): evolution tectonique á partir du traitement do données MNT-SPOT. C. R. *Acad. Sci*. Paris, 318, 1117-1124.

Moore G., Marone C., Carmichael I.S.E., Renne P., 1994, Basaltic volcanism and extension near the intersection of the Sierra Madre volcanic province and the Mexican Volcanic Belt. *Geol. Soc. Amer. Bull*., 106, p. 383-394.

Nixon G.T., 1982, The relationship between Quaternary volcanism in Central Mexico and the seismicity and structure of subducted oceanic lithosphere. *Geol. Soc. Am. Bull*., 93, 514-523.

Pacheco J.F., Mortera-Gutiérrez C.A., Delgado H., Singh S.K., Valenzuela R.W., Shapiro N.M., Santoyo M.A., Hurtado A., Barron R., Gutiérrez-Moguel E., 1999, Tectonic significance of an earthquake sequence in the Zacoalco half-graben, Jalisco, Mexico. *Jour. of South Amer. Earth Sci*., 12, 557-565.

Palmer R.H., 1926, Tectonic Setting of Lago de Chapala, *Pan American Geol*., 45, 125-134.

Pasquaré G., Garduño V.H., Tibaldi A., Ferrari M., 1988, Stress pattern evolution in the central sector of the Mexican Volcanic Belt: *Tectonophysics*, 146, p. 353-364.

Rosas-Elguera J., Urrutia-Fucugauchi J., Maciel R., 1989, Geología del Extremo Oriental del Graben de Chapala; breve discusión sobre su edad - Zonas geotérmicas de Ixtlán de los Hervores-Los Negritos, México, Geotermia, 5, p. 3-18.

Rosas-Elguera J., Ferrari L., Garduño-Monroy V.H., Urrutia-Fucugauchi J., 1996, Continental boundaries of the Jalisco Block and their influence in the Pliocene-Quaternary kinematics of western Mexico. *Geology*, 24, p. 921-924.

Rosas-Elguera J., Ferrari L., López-Martínez M., Urrutia-Fucugauchi J., 1997, Stratigraphy and Tectonics of the Guadalajara Region and Triple Junction Area, Western Mexico: *International Geology Review*, 39, p. 125-140.

Rosas-Elguera J., Urrutia-Fucugauchi J., 1998, Tectonic control of the volcano-sedimentary sequence of the Chapala graben, western Mexico. *Int. Geol. Rev*., 40, p. 350-362.

Serpa L., Katz C., Skidmore C., 1989, The southeastern boundary of the Jalisco Block in west-central Mexico (abs) EOS Transactions, *American Geophysical Union*, 43, p. 1319.

Serpa L., Smith S., Katz C., Skidmore C., Sloan R., Pavlis T., 1992, A geophysical investigation of the southern Jalisco Block in the State of Colima, Mexico. *Geofisica Internacional*, 31, p. 475-492.

Slater D.M., Jacyna G.M., 2012, Evaluating detection and estimation capabilities of magnetometer-based vehicle sensors, MITRE Technical Report. 19 pp.

Smith M.L., 1980, The evolutionary and ecological history of the fish fauna of therio Lerma basin, Mexico. Ph. D. Thesis, University of Michigan, 201 pp.

Talwani M., 1965, Computation with the help of a digital computer of magnetic anomalies caused by bodies of arbitrary shape. *Geophysics*, 30, 797.

Urrutia-Fucugacuhi J., Molina-Garza R.S., 1992, Gravity modelling os a regional crustal and upper mantle structure of the Guerrero terrane - 1. Colima graben and southern Sierra Madre Occidental, western Mexico, *Geofísica Internacional*, 31, 4, p. 493-507.

Urrutia-Fucugauchi J., Rosas-Elguera J., 1994, Paleomagnetic study of the eastern sector of Chapala Lake and implications for the tectonics of west-central Mexico. *Tectonophysics*, 239, p. 61-71.

Vandeville B., Cobbold P.R., 1988, How normal faulting and sediments interact to produce listric fault profiles and stratigraphic wedges. *J. Struct. Geol*., 10, p. 649-659.

Venegas S., Ruy C., 1981, Estudio Geológico Regional de las Planillas, Jalisco. Comisión Federal de Electricidad. Internal Report, 61 pp.

Wernicke B., Burchfiel B.C., 1982, Modes of extensional tectonics, *J. Str. Geol.*, 4, 105-115.

Wright J.V., Walker G.P.L., 1981, Eruption, transport and deposition of ignimbrite: a case study from Mexico. *Journal of Volcanology and Geothermal Research*, 9, p. 111-131.

## Addendum

To control the quality marine magnetic data we conduct a field experiment, consisting in measure total magnetic field along an E-W line with a G856 magnetometer fixed in the western extreme as a base station, and displacing an outboard 104 lbs engine each meter along the line. The line was located approximately 100 meters away from agricultural iron fences of the Centro Universitario de Ciencias Biologico Agropecuarias, NW from Guadalajara City. The resulting measurements show that the magnetic effect of the engine reaches near 2 nanoTeslas in 4 meters, disappearing completely away this distance (Figure A1). Actually the length of the fiberglass boat is near to 5 meters (not clear in the Figure 3 as the boat is not completely normal to the photographer).

This was expected because of the intrinsic components of the motor. A great percentage of the dry motor weight is due to aluminum and copper. The main magnetic effect (almost 150 nT) is considered from magnets and other iron elements as the motor shaft.

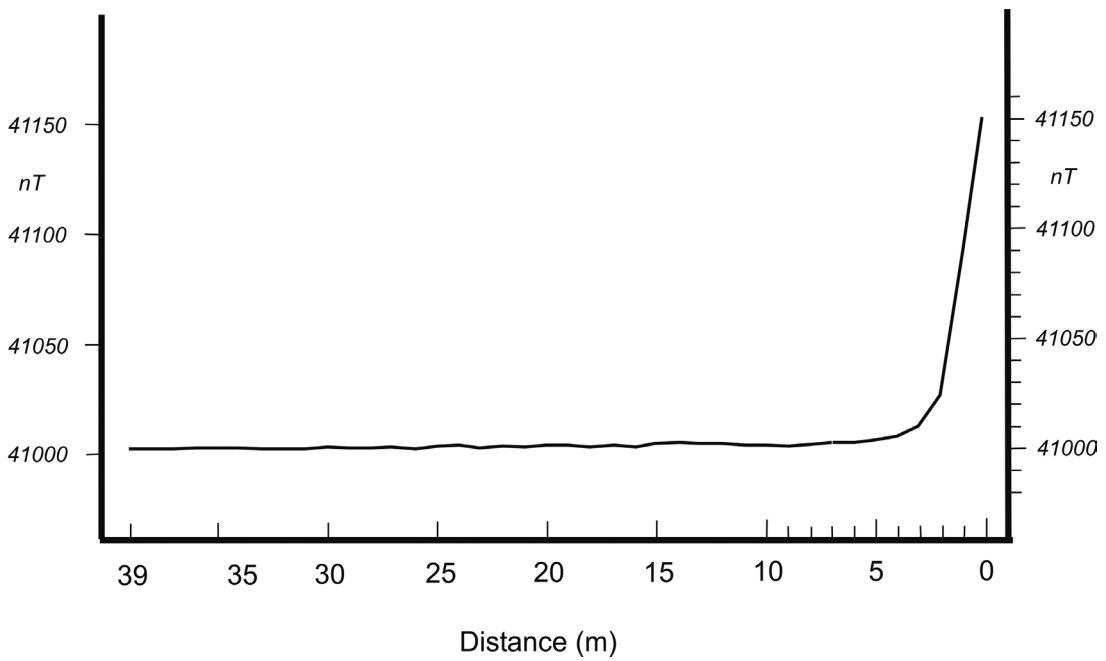


**Figure A1.** Magnetic effect of the outboard motor of the boat used in this study; the measurements were made displacing the motor and setting the magnetometer at the 0 coordinate.

Geofísica Internacional (2015) 54-4: 343-352

Original paper

# Surface DC resistivity survey of contamination Beneath Ido-Osun dumpsite, southwestern Nigeria

Gabriel Oyelowo Bayowa, Dele Ebenezer Falebita and Raheem Olajide Adegboyesga

Received: November 07, 2014; accepted: June 23, 2015; published on line: October 01, 2015

**Resumen**

DC resistividad superficial las técnicas se han utilizado para investigar las características del subsuelo torno un abandonado vertedero en Ido-Osun, suroeste de Nigeria. El objetivo es delinear contaminación de las aguas subterráneas, identificar las capas litológicas, localizar posibles lixiviados penachos de humo y evaluar el riesgo de contaminación de las aguas subterráneas. Sondeo eléctrico vertical Schlumberger (VES) y dipolo-dipolo resistividad perfiles de datos fueron adquiridos en 20 m y 10 m, respectivamente a lo largo de tres intervalos noroeste-sureste geofísicos recorre. La geoelï secciones reveló cuatro probables las capas subsuperficiales geoeléctricos que se consideraban de superior del suelo, laterita, capeado y roca fracturada y competente/roca con base en trabajos previos. La roca fracturada constituye la reserva de agua subterránea en la zona interpretado a partir del más del 98% de H, KH geoelï tipos de curva. El dipolo-dipolo secciones mostro zonas de baja resistividad que se extiende en el capeado/roca fracturada. Estos fueron interpretados como probable contaminante plume por debajo del vertedero.

Palabras clave: DC superficial, las aguas subterráneas, vertedero, contaminación, Nigeria.

**Abstract**

Surface DC resistivity techniques have been used to investigate the subsoil characteristics around an abandoned dumpsite in Ido Osun, Southwestern Nigeria. The aim was to delineate groundwater contamination, identify lithologic layers, locate possible leachate plumes, and assess the risk of groundwater pollution. Schlumberger vertical electrical sounding (VES) and Dipole–dipole resistivity profiling data were acquired at 20 m and 10 m intervals respectively along three northwest-southeast geophysical traverses. The geoelectric sections revealed four probable subsurface geoelectric layers which were considered to be topsoil, laterite, weathered/fractured bedrock and competent/fresh bedrock based on previous works. The weathered/fractured bedrock forms the groundwater reservoir in the area as interpreted from the over 98% occurrence of H, KH geoelectric curve types. The dipole-dipole sections showed several distinct low resistivity zones which extends into the weathered/fractured bedrock. These were interpreted as probable contamination plumes beneath the dumpsite.

Key words: Surface DC, groundwater, dumpsite, contamination, Nigeria.

O. G. Bayowa
O. R. Adegboyega
Department of Earth Sciences
Ladoke Akintola University of Technology
Ogbomoso, Nigeria
Email: *oyebayowa@yahoo.com*
*accessrahool@yahoo.com*

D. E. Falebita
Department of Geology
Obafemi Awolowo University
Ile-Ife, Nigeria
*Corresponding author: delefalebita@gmail.com*

## Introduction

Solid waste is a non-liquid and non-gaseous product of human activities which could pose threat to both surface and groundwater systems. The environment of disposal is referred to as dumpsite and is defined as a place where refuse or other discarded materials are dumped (Ariyo and Enikanoselu, 2007). In Nigeria and other developing countries worldwide, wastes are mostly dumped on open grounds, landfills and in water bodies, constituting serious environmental and health problems and posing a major problem on groundwater. Contamination from solid wastes begins with the release of leachates into land surface and ends with the water reaching groundwater. Precipitation on the refuse dumpsite will either infiltrate the refuse or run off as over land flow (Ariyo and Enikanoselu, 2007). During the vertical percolation process (with rain water) the water leaches both organic and inorganic constituents from refuse and becomes part of the groundwater flow system when they reach the water table (Langer, 1998; Baba and Tokogoz, 1999; Christoph and Dermietzel, 2000; Rao *et al*., 2001; Baba, 2003). "The most common approach for investigating leachate plume migration from a dumpsite is to drill a network of monitoring wells around the site. However, these wells are expensive to construct and maintain" (Zume *et al*., 2006). "Additionally, limited information on subsurface hydrogeology and/or budget limitations frequently compels the citing of monitoring wells at random. This approach is both technically and economically inefficient because monitoring wells give point measurements, whereas leachate plumes tend to migrate along preferential pathways, determined by subsurface heterogeneity" (Zume *et al*., 2006). Therefore, even with a network of closely spaced monitoring wells, the risk that some contaminants could go undetected remains high. For these reasons, there is widespread interest in applying noninvasive and relatively inexpensive geophysical techniques, such as electrical resistivity imaging (ERI), electromagnetic methods, electrical conductivity (EC) logging, and seismic surveys, as means for mapping the occurrence and movement of leachate and for facilitating decision making regarding the location of monitoring wells (Bernstone and Dahlin, 1997; Butler *et al*., 1999; Buselli and Lu, 2001). These geophysical methods have been used prior to waste disposal installations and for evaluation of possible leachate flow after dumping of waste because they generate nearly continuous image of the subsurface that can significantly reduce the risk of undetected contaminants (Zume *et al*., 2006; Olorunfemi and Mesida, 1987; Sharma, 1997; Schulmeister *et al*., 2003; Abu-Zeid *et al*., 2004; Naudet *et al*., 2004; Bayowa *et al*., 2012).

This article reports the application of the electrical geophysical method involving the vertical electrical sounding (VES) and 2D profiling (Dipole-Dipole) techniques to map possible leachate distribution and migration processes from the abandoned Ido Osun landfill site, Osun State, southwestern, Nigeria. The two techniques are based on the response of underground geologic features to a current flow field and are capable of detecting different subsurface units on the basis of the contrasts in electrical resistivity of earth materials (Telford *et al*., 1990). They are fast and cost effective. The former measures the vertical variations in resistivity of the subsurface earth while the latter involves the measurement of lateral and vertical variations of the apparent resistivity of the subsurface earth. The specific objectives of this study, therefore, were to delineate groundwater contamination, identify lithologic layers, locate possible leachate plumes, and assess the risk of groundwater pollution as a result of the dumpsite. This is with the view of assessing the risk associated with the groundwater abstraction in the area. The outcomes of this study will help appropriate decision-making on how and where to abstract underground water and remediation methods to adopt.

## Study area

The study area, Onibuaje dumpsite, is located in Ido-Osun, Osun State, Southwestern Nigeria within Latitude $7^0$ $47.575^1$ and $7^0$ $47.875^1$ and Longitude $4^0$ $29.359^1$ and $4^0$ $29.957^1$ (Figure 1). The dumpsite used to be active and covered an area of (360 m by 220 m) with height that varied between 0.5 m to 3 m. It was abandoned in the year 2003 due to the government policy to salvage the area from further environmental pollution. A southward bound network of streams has given rise to marshy environment located west of the dumpsite. Several construction sites have begun to develop and other human activities have increased around the area since 2007. The only hand dug well in the vicinity of the area is seasonal in term of water content and it is only being used for construction purposes. Human activities will increase in this area and there will be need for potable groundwater for drinking, cooking and bathing in the future. The question is to what extent will the developing community be affected by the abandoned dumpsite since the safety and well-being of the people who will

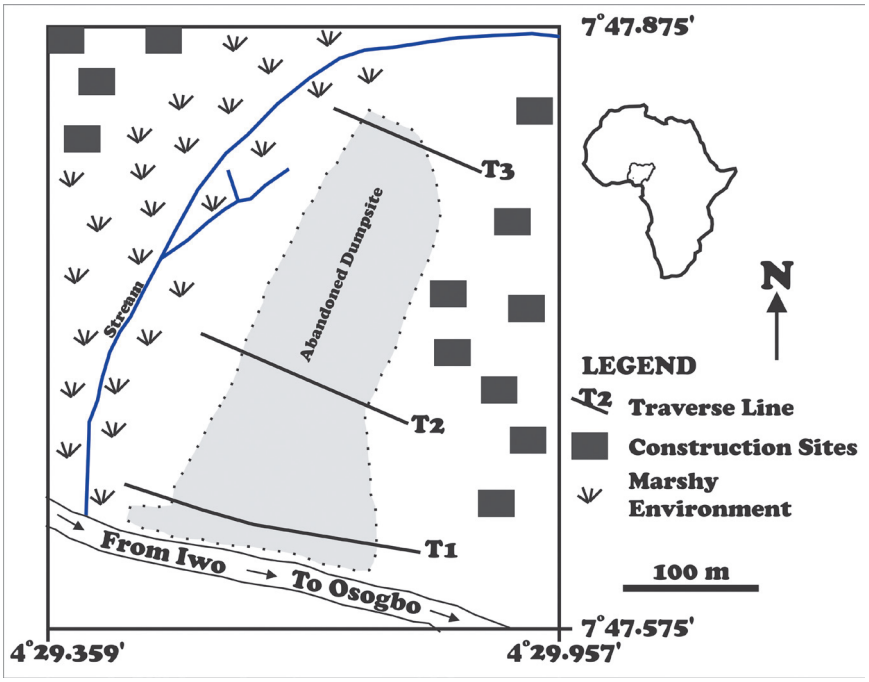


**Figure 1.** Base map of the study area showing the dump site and the geophysical traverses.

live in the area will depend on the abstraction of quality groundwater. Regionally, the area is underlain by quartzite which is a member of the Precambrian Basement Complex rocks of Southwestern Nigeria (Rahaman, 1988). The Basement Complex rocks have been classified into (1) Migmatite gneiss-quartzite complex, (2) slightly migmatized to non-migmatized metasedimentary and metaigneous rocks, and (3) members of the Older Granite Suite (Rahaman, 1988). These rocks constitute the prominent outcrops and inselbergs that define the topographic highlands in the area (Adediji and Ajibade, 2008). The area is characterized by tropical rain forest and has humid climate with an average temperature of between 21.1°C and 31.1°C and annual rainfall of about 1000 mm with the rainy season covering eight months; beginning in April and ending in November (OSSADEP, 1997).

## Data collection and analysis

The survey which was carried out in 2012 involved the electrical resistivity techniques. Electrical resistivity surveys are usually designed to measure the electrical resistivity of subsurface materials by making measurements on or within the earth (Van Nostrand and Cook, 1966; Ebraheem *et al*., 1997; Zonge *et al*., 2005; Lowrie, 2007). An electrical current (*I*) is imposed on the ground by a pair of electrodes at varying spacing expanding symmetrically from a central point for VES while measuring the surface expression of the resulting electric potential (ΔV) with an additional pair of electrodes at appropriate spacing. The apparent resistivity ($\rho_a$) is given by:

$$\rho_a = \frac{\Delta V}{I} \cdot K \qquad (1)$$

Where $\rho_a$ is the apparent resistivity and *K* is the geometric factor which takes into account the geometric spread of the electrode array. In this study, the vertical electrical sounding (VES) and 2-D imaging technique were adopted on three traverses established in NW-SE direction around the accessible parts of the dumpsite. The Schlumberger array was adopted for the VES while the dipole-dipole array was adopted for the 2-D imaging technique.

### *The Schlumberger Technique*

The Schlumberger array is one of the most commonly used arrays and it is used mainly for resistivity sounding in a layered environment where it provides excellent vertical resolution. The depth of investigation of the electrode array is 0.125AB, where AB is the total current electrode separation (Roy and Apparao, 1971). It employs a four electrode system, two current electrodes C1 and C2 and two potential electrodes P1 and P2. The apparent resistivity ($\rho_a$) values were calculated from equation (1) and the results are presented as sounding curves and geoelectric sections. For Schlumberger array (1) take the form

$$\rho_a = \frac{\Delta V}{I} \bullet \frac{\pi L^2}{2l} \qquad (2)$$

Where $\Delta V/I$ is the ground resistance (measured in ohms), $L$ (m) is half the current-current electrode spacing (AB/2), $l$ (m) is half the potential-potential electrode spacing and π is a constant (3.142 or 22/7).

Twenty-Six (26) VES data points were acquired on three traverses, namely, Traverse I, Traverse II and Traverse III (Figure 1) with ABEM Terrameter SAS 1000 using station interval of 20 m and half current electrode spacing varied from 1 to 65 m. The VES data were plotted on log-log graph while adopting partial curve matching technique to generate initial inputs for the 1-D forward modeling using InterpretVES™ software. The final VES layer parameters were used to produce 2-D geoelectric images along each traverse. The depth sounding curves obtained in the study area are grouped on the basis of layer resistivity combination into H, KH and A types (Table 1) and Figure 2.

*Dipole-Dipole Technique*

The Dipole-Dipole array is a 2-D imaging technique that involves the measurement of lateral and vertical variations in apparent resistivity of the subsurface earth (Roy and Apparao, 1971). The apparent resistivity is calculated from equation (3),

$$\rho_a = \frac{\Delta V}{I} \bullet \frac{\pi}{a^2}\left(L\left(L^2 - a^2\right)\right) \qquad (3)$$

The $\Delta V/I = R$ (the ground resistance (ohms)) and spacing of the electrodes in each pair is *a (m)*, while the distance between their mid-points is *L (m)*, which is generally much larger than *a*. The measured resistivity values are plotted against the points of intersection of two $45^0$ inclined lines from the mid – points of the current and potential dipoles. The interpretation usually involves the construction of geoelectric sections and inversion into 2D resistivity images.

Fifty-Two (52) dipole-dipole data points were acquired using 10 m station interval on the three traverses altogether. In the field, the expansion factor, *n* (distance between the leading potential and trailing current electrodes), was varied from 1 to 5 with a depth range of 2.9 – 6.8 m (Roy and Apparao, 1971). The data were processed using the DIPROfWin™ Version 4 software to generate 2-D resistivity images of the subsurface beneath the dumpsite

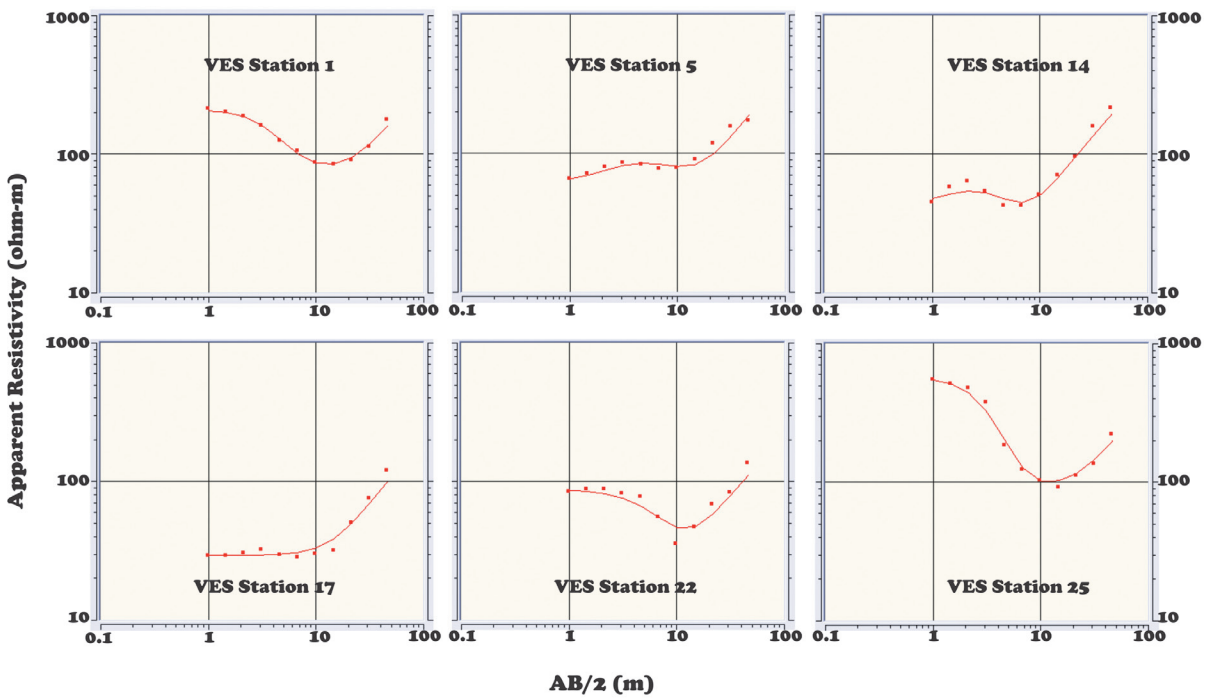


**Figure 2.** Selected field and computed VES curves types from the study area.

below each of the three traverses after iterating 10 times. The inversion using the DIPROfWin software was based on FEM modelling. The absolute RMS Errors for the traverse 1, traverse 2 and traverse 3 are 0.311904, 0.385059 and 0.357008 respectively. The two survey techniques were carried out within three days with the same equipment. The combination of the geoelectric sections derived from the VES points on each traverse and the inverted 2D resistivity models were used to delineate possible subsurface resistivity layers, aquifer system and the quality of the aquifer fluid.

## Results and discussion

*Traverse I ($T_1$)*

Figure 3 shows the VES and 2D imaging results obtained on Traverse I. Table 1 reveals that H and KH curve types are predominant beneath this traverse. These curve types are usual pointers to the possibility of the occurrence of groundwater in the basement complex of Nigeria (Olorunfemi and Olorunniwo, 1985; Ako and Olorunfemi, 1989; Olayinka and Olorunfemi, 1992; Olorunfemi and Fasuyi,

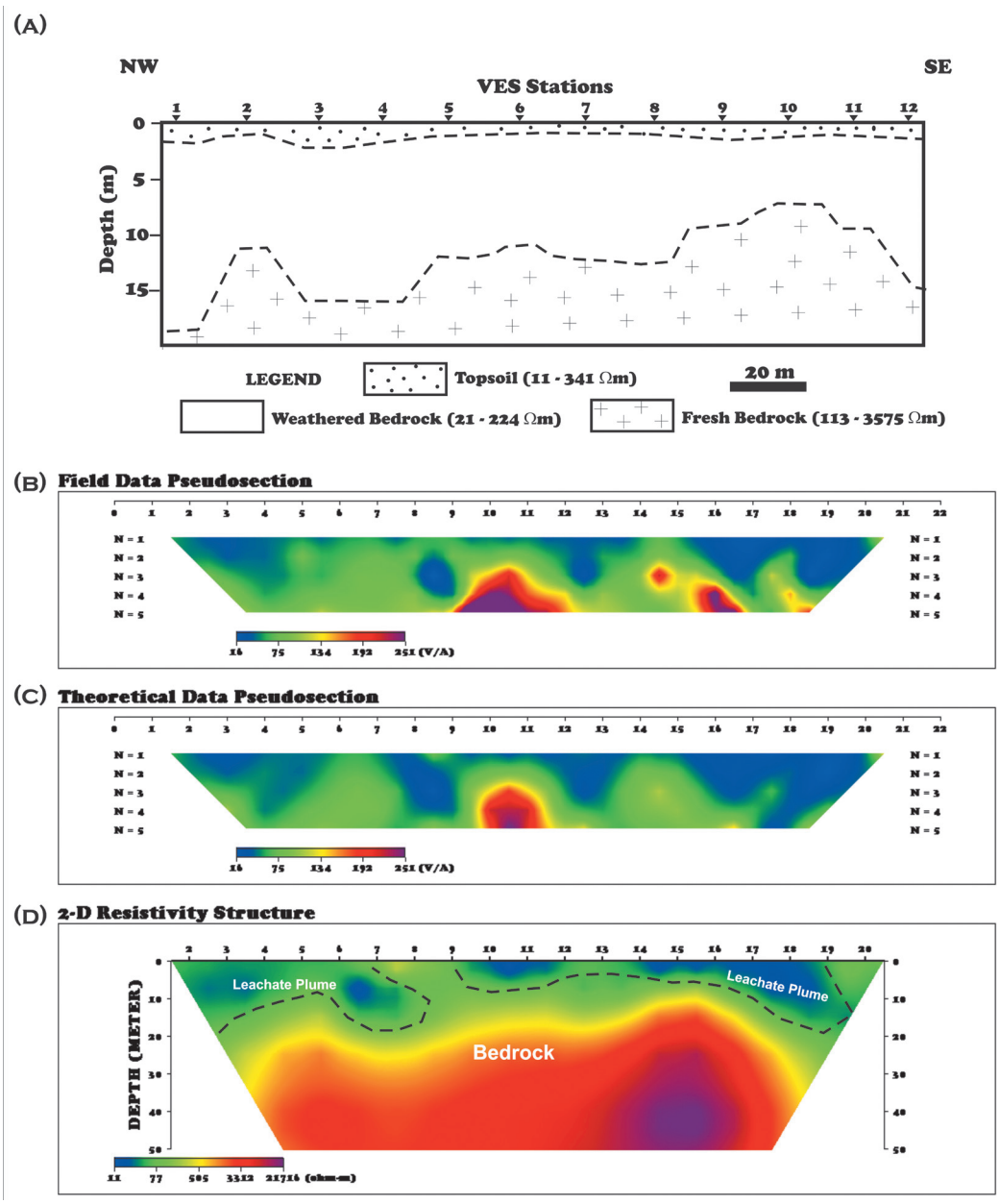


**Figure 3.** Showing (A) VES geoelectric image, (B) field pseudosection, and (C) theoretical pseudosection (D) 2-D inversion model along traverse.

1993). The VES geoelectric section (Figure 3A) is 220 m long and relates VES 1, 2, 3, 4, 5, 6, 7, 8, 9, 10, 11 and 12 in the NW-SE direction. Three distinct geoelectric layers can be identified on the section. The first layer with resistivity values varying between 11 and 341 Ωm and the layer thickness values between 1.0 and 2.3 m was associated with the topsoil. The second layer with resistivity values ranging between 21 and 224 Ωm and depth to base of the layer ranges between 8.5 and 20.6 m was referred as the weathered zone. This is usually the groundwater interval. The third layer was taken as the fresh bedrock with layer resistivity values range between 113 and 3575 Ωm. Figures 3B and 3C represent the observed dipole-dipole pseudo-section, and 2-D Inversion Model respectively. The 2-D resistivity structure reveals relatively low resistivity values in the range of 5 and 14 Ωm typical of contamination zones (Adepelumi *et al*., 2005; Urish, 1983; Bayowa *et al*., 2012) between stations 2 and 8 at a depth range between 3 and 12 m; stations 10 and 12 at about 5 m depth and between stations 14 and 19.5 at depth range between 5 to 15 m. At the depth of detection of the plumes, it is apparent that the groundwater is contaminated.

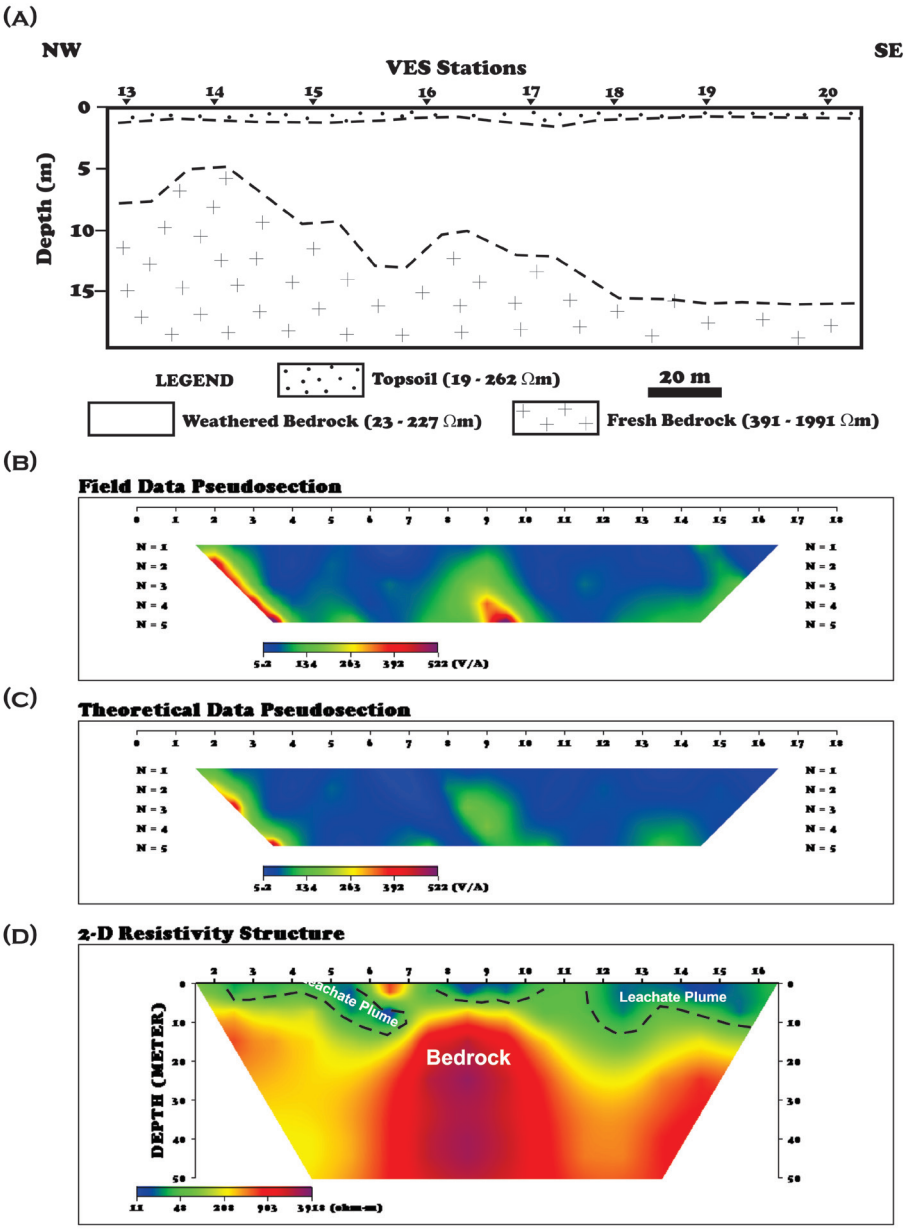


**Figure 4.** Showing (A) VES geoelectric image, (B) field pseudosection, and (C) theoretical pseudosection (D) 2-D inversion model along traverse 2.

*Traverse II ($T_2$)*

H and KH type curves were obtained on this Traverse in most cases (Table 1). This is similar to traverse I and indicates groundwater potential below it. Figure 4 relates the VES and 2D-Imaging results of the Traverse. Figure 4A is a VES geoelectric section that relates VES 13, 14, 15, 16, 17, 18, 19, and 20. The total length of this traverse is about 180 m. The VES geoelectric section shows three major geoelectric subsurface layers as in traverse I. The first layer with layer resistivity varying between 19 and 262 Ωm and thickness range between 0.7 and 1.3 m was associated with the topsoil. The second layer was considered as the weathered zone with resistivity values ranging between 23 and 227 Ωm and depth range between 2.2(1.3?) and 19.1(15?) m while the third layer was taken as the fresh bedrock with resistivity values between 391 and 1991 Ωm. Figures 4B and 4C are the observed dipole-dipole pseudosection, and 2-D Inversion Model along the traverse

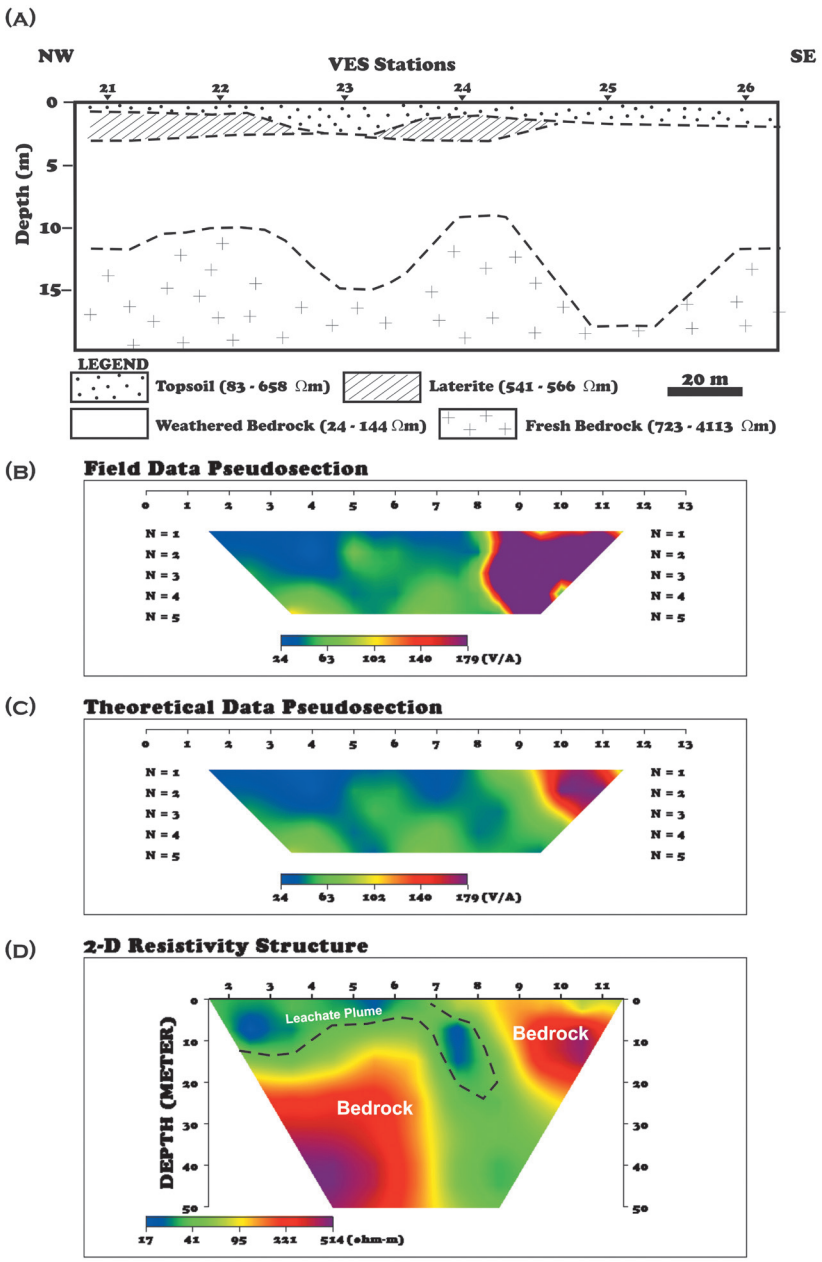


**Figure 4.** Showing (A) VES geoelectric image, (B) field pseudosection, and (C) theoretical pseudosection (D) 2-D inversion model along traverse 3.

respectively. The 2-D image indicates distinct low resistivity zones (Adepelumi *et al*., 2005; Urish, 1983; Bayowa *et al*., 2012) of possible contamination between stations 2 and 7 at about 10 m depth; stations 8 and 10 at a depth of 3 m and between stations 12 and 16 at a depth range between 0 and 8(11?) m.

*Traverse III ($T_3$)*

Only H and KH type curves were obtained beneath this traverse as indicated in Table 1. Figure 5A is the VES geoelectric section that relates VES 21, 22, 23, 24, 25 and 26 along the traverse. The section spans a distance of about 120 m and shows four possible subsurface layers. The first layer with layer resistivity range between 83 and 658 Ωm and thickness range between 0.9 and 2.5 m was associated with the topsoil. The second layer with resistivity values that range between 541 and 566 Ωm and depth values between 2.6 and 3.2 m was taken as representing laterite. The third layer with resistivity values that range between 24 and 144 Ωm and depth values between 2 and 16.6 m was associated with the weathered zone while the fourth layer with resistivity values range between 723 and 4113 Ωm was depicted as the fresh bedrock. Figures 5B and 5C show a field dipole-dipole pseudo-section and 2-D resistivity structure of the subsurface beneath Traverse 3. Exceptionally low resistivity values suspected to be contaminant leachate plumes (Adepelumi *et al*., 2005; Urish, 1983; Bayowa *et al*., 2012) are observed between stations 2 and 4 at a depth range between 0 and 15 m; stations 5 and 6 at a depth of about 5 m and; stations 6 and 8 at a depth beyond 30 m.

These results show that there is a high possibility that the underground water beneath the dumpsite is polluted. Moreover, the topsoil beneath the dumpsite is too thin to prevent percolation of leachates to underground water. Since the thickness of the weathered layer and the nature of the bedrock topography indicate that the study area is potentially a high groundwater accumulation and recharge zone, urgent steps must be taken to prevent probable water related diseases in the vicinity of the dumpsite.

## Conclusions

This study has employed Schlumberger VES and Dipole-Dipole electrical profiling techniques to map the surface and delineate possible contamination of the groundwater in the vicinity of an abandoned dumpsite in Ido-Osun, Southwestern Nigeria. The interpretation of the data has provided information as regards the subsurface geolectric layers, the bedrock topography, groundwater potential and possible groundwater contamination in the study area. Four geoelectric layers were identified and were depicted as the topsoil, the lateritic layer, the weathered layer, and the fresh bedrock. The geoelectric curve types indicate high groundwater potential in the area. The H-type is the most prevalent of all the multi-layer curves accounting for 48% of the total. The KH-type accounts for 45% and A-type curve accounts for about 7%. Distinct low resistivity zones corresponding to contamination plumes were delineated from the dipole sections. These low resistivity zones extend into the weathered bedrock and possibly suggest contamination of the groundwater in this layer. Groundwater abstraction should be done far away or subjected to adequate water treatment for the safety of the future residents in the vicinity of the abandoned dumpsite.

## Acknowledgement

The authors wish to acknowledge the use of the DIPRO software available in the Department of Geology, Obafemi Awolowo University, Ile-Ife, Nigeria.

## References

Abu-Zeid N., Bianchini G., Santarato G., Vaccaro C., 2004, Geochemical characterization and geophysical mapping of landfill leachates: The Marozzo Canal case study (NE Italy) : *Environmental Geology*, 45, 439–447.

Adediji A., Ajibade L.T., 2008, The Change Detection of Major Dams in Osun State, Nigera using Remote Sensing (RS) and GIS techniques. *Journal of Geography and Regional Planning*, 1, 6, pp 110 -115.

Adepelumi A.A., Ako B.D., Afolabi O., Arubayi J.B., 2005, Delineation of contamination plume around oxidation sewage-ponds in Southwestern Nigeria. *Environmental Geology*, 48, 8, pp. 1137-1146.

Ako B.D., Olorunfemi M.O., 1989, Geoelectric survey for groundwater in the Newer Basalts of Vom, Plateau State. *Journal of Mining and Geology*, 25, pp. 247-250.

Ariyo S.O., Enikanoselu E.M., 2007, Integrated use of Geoelectrical Imaging and Geochemical Analysis in the Environmental Impact Assessment of Egbe dumpsite in Ijebu-Igbo Area, Southwestern Nigeria. *Continental Journal of Earth Sciences*, 1, pp. 11-17.

Baba A., 2003, Geochemical Assessment of Environmental effects of ash from Yatagan (Mugla Turkey) Thermal power plant. Water, air, and soil Pollution, 144, pp 3-18.

Baba A., Tokgöz S., 1999, Impact of Izmir Harmandah; Sanitary Landfill area on Surface water and Groundwater: Water Congress in Izmir, pp 263-275.

Bayowa O.G., Falebita D.E., Olorunfemi M.O., Adepelumi A.A., 2012, Groundwater Contamination Prediction Using Finite Element Derived Geoelectric Parameters Constrained by Chemical Analysis around a Sewage Site, Southwestern Nigeria. *International Journal of Geosciences*, 3, pp 404-409.

Bernstone C., Dahlin T., 1997, DC Resistivity Mapping of old landfills: Two case studies. *European Journal of Environmental and Engineering Geophysics,* 2, 121–136.

Buselli G., Lu K., 2001, Groundwater Contamination Monitoring with Multichannel Electrical and Electromagnetic Methods. *Journal of Applied Geophysics,* 48, 11–23.

Butler J.J., Healey J.M, Zheng L, McCall W., Schulmeister M.K., 1999, Hydrostratigraphic Characterization of unconsolidated alluvial deposits with direct-push Sensor Technology. Kansas Geological Survey Open-File Report, 99-40.

Christoph G., Dermietzel J., 2000, The impact of a contaminated lignite seam on groundwater quality in the aquifer system of the Bitterfeld Region, modeling of groundwater contamination. Water, Air and Soil Pollution, 122, pp 421-431.

Ebraheem A.A.M., Senosy M.M., Dahab K.A., 1997, Geoelectrical and Hydrogeochemical Studies for Delineating Ground-water Contamination due to Salt-Water Intrusion in the Northern Part of the Nile Delta, Egypt. *Groundwater*, 35, 2, 216-222.

Langer M., 1998, Geoenvironmental Aspects of Waste Disposal. *Environment Geology*, 35, pp 1-2.

Lowrie W., 2007, Fundamentals of Geophysics. Cambridge University Press, UK, 383pp.

Naudet V., Revil A., Rizzo E., Bottero J.Y., Bégassat P., 2004, Groundwater redox conditions and conductivity in a contaminant plume from geoelectrical investigations, *Hydrol. Earth Syst. Sci.*, 8, 1, pp 8–22.

Olayinka A.I., Olorunfemi M.O., 1992, Determination of geoelectric characteristics in Okene Area and Implication for boreholes siting. *Journal of Mining and Geology*, 28, pp. 403-412.

Olorunfemi M.O., Fasuyi S.A., 1993, Aquifer types and the geoelectric/hydrogeologic characteristics of part of the central basement terrain of Nigeria (Niger State). *Journal of African Earth Sciences*, 16, 3, pp 309-317.

Olorunfemi M.O., Mesida E.A., 1987, Engineering Geophysics and its Application in Engineering Site Investigation (Case Study from Ile Ife area). *The Nigerian Engineer*, pp. 22, 2, 57-66.

Olorunfemi M.O., Olorunniwo M.A., 1985, Geoelectric parameters and aquifer characteristics of some parts of Southwestern Nigeria. *Geologia Applicata E. Idrogeologia*, 20, pp. 99-109.

Osun State Agricultural Development Programme (OSSADEP, 1997). The report of 1996 crop area and yield survey conducted by planning, monitoring and evaluation Department, Osun State Press, Osogbo, Nigeria, pp 11.

Rahaman M.A., 1988, Recent Advances in the study of the Basement complex of Nigeria. In : Oluyide, P. O., Mbonu, W. C., Ogezi A. E., Egbuniwe, I. G., Ajibade, A. C and Umeji A. C(eds.). Precambrian Geology of Nigeria, G. S. N. pp. 11-41.

Rao V.V.S.G., Ohar R.L., Subrahmanyam K., 2001, Assessment of Contaminant migration in groundwater from an Industrial development area, Medale District, Andhra Pradesh, India of Texts and Monographs, pp.649.

Roy A., Apparao A., 1971, Depth of Investigation in Direct Current Methods, *Geophysics*, 36, 5, pp. 943-959.

Schulmeister M.K., Butler J.J., Healey J.M., Zheng L., Wysocki D.A., McCall G.W., 2003, Direct-push electrical conductivity logging for high-resolution hydrostratigraphic characterization, *Ground Water Monitoring & Remediation,* 23, 3, 52-62.

Sharma P.V., 1997, Environmental and Engineering Geophysics, Cambridge University Press, Cambridge, 475 pp.

Telford W.M., Geldart L.P., Sheriff R.E., 1990, Applied geophysics: Cambridge University Press.

Urish D.W., 1983, The Practical Application of Surface Electrical Resistivity to Detection of Ground-Water Pollution. *Groundwater*, 21, 144–152. doi: 10.1111/j.1745-6584.1983.tb00711.

Van Nostrand R.G, Cook K.L., 1966, Interpretation of Resistivty Data. *Geological Survey Prof*. Paper 499, US Geological Survey.

Zonge K., Wynn J., Urquhart S., 2005, Resistivity, Induced Polarization and Complex Resistivity. In: Near Surface Geophysics, Butler, D. K (ed.). Society of Exploration Geophysics, pp 265-300.

Zume J.T., Tarhule A., Christenson S., 2006, Subsurface Imaging of an Abandoned Solid Waste Landfill Site in Norman, Oklahoma. *Groundwater Monitoring & Remediation*, 26, 2, pp. 62-69.

Geofísica Internacional (2015) 54-4: 353-362

Original paper

# Electrical resisitivity to detect zones of biogas accumulation in a landfill

César Augusto Moreira*, Thais Munhoz, Fernanda Cavallari and Lívia Portes Innocenti Helene

Received: November 26, 2014; accepted: August 08, 2015; published on line: October 01, 2015

**Resumen**

El biogas producido en rellenos sanitarios puede ser una fuente importante de energía en el futuro. Este gas, constituido por $CH_4$, $CO_2$ y vapor de agua, se forma por la descomposición de materia orgánica. Una de las limitaciones técnicas en la planeación de sistemas colectores de este gas es la forma de estimar la producción de metano en un relleno dado. En este trabajo se evalúa la relación entre el flujo de biogas medido en drenes de un relleno sanitario en Brasil con la resistividad eléctrica del material de relleno. La medición en perfiles con el método de Tomografía de Resistividad Eléctrica (TRE) y su inversion a modelos 2D de resistividad muestra una clara correlación entre zonas de alta producción de biogás con áreas de alta resistividad en profundidad. Estos resultados sugieren la posibilidad de usar el método de TRE como una herramienta diagnostica en la colocación de drenes de extracción de biogas en rellenos sanitarios..

Palabras clave: energía, metano, materia orgánica, tomografía de resistividad eléctrica (TRE).

**Abstract**

Biogas produced in sanitary landfills consists in a potential source, formed by degradation of organic matter, this gas is constituted by $CH_4$, $CO_2$ and water vapor. Sanitary landfills represent important depository of organic matter with great energetic potential in Brazil, although presently with inexpressive use. Estimates for production or maintenance of productive rates of $CH_4$ represent one of the main difficulties of technical order to the planning and continuity of collection systems for rational consumption of this resource. Electrical resistivity measurements are routinuously used in profiling oil wells for the determination of levels with accumulations of oil and gas, facing the contrast among fluids and rocks. This paper aims to evaluate eventual relationship among biogas flow quantified in surface drains of a waste cell in landfill, with characteristic patterns of in depth electrical resistivity. The integration of Electrical Resistivity Tomography (ERT) lines allowed for the generation of 3D blocks and a clear distinction among zones of high biogas production, quantified in surface drains, with areas of high resistivity in depth. The results suggest the possibility of use of the method in studies to place drains in areas promising to the collection of biogas for energetic generation in sanitary landfill.

Key words: energy, methane, organic matter, electrical resistivity tomography (ERT).

C. A. Moreira*
Department of Applied Geology
Geosciences and Exact Sciences Institute
Univ. Estadual Paulista
Av. 24-A, 1515
Bela Vista, 13506-900
Rio Claro, São Paulo State, Brazil
*Corresponding author:moreirac@rc.unesp.br

T. Munhoz
F. Cavallari
L. Portes Innocenti Helene
Geosciences and Exact Sciences Institute
Univ. Estadual Paulista (UNESP)
Bela Vista, 13506-900
Rio Claro, São Paulo State, Brazil

## Introduction

The use of renewable resources as a source of clean and sustainable energy gains increasing importance internationally, facing growing energy demands driven by population growth and improved quality of life in developing countries (Smill, 2008). This demand causes inflation in prices of major energy sources like petroleum and coal, as well as increased rates of emission of greenhouse gases (EIA, 2014).

This scenario stimulates the search for alternative energy sources that go from expressionless features to options with growing importance. Renewable sources such as biomass are environmentally sustainable and technically viable, either for direct generation of electricity and heat, or conversion to methane production (IEA, 2011).

Biogas is a natural form of biogenic matter formed from the conversion of biomass through the action of a group of microorganisms when metabolically active (Wellinger *et al*., 2013). This product consists in a gas mixture resulting from the anaerobic degradation of organic matter contained, for example, in landfill solid waste and industrial waste and wastewater. In this context, this substrate represents the available biomass for fermentation (Themelis & Ulloa 2007).

In this scenario, the landfills have significant relevance as depository of large amounts of substrate capable of conversion into biogas (Nozhevnikova *et al.*, 1993; Deublein & Steinhauser 2008). The biogas from landfill has on average between 45% and 55% methane, the major flammable gas and of potential energy use, besides varying amounts of carbon dioxide and water vapor (Tchobanoglous *et al*., 1993; Kjeldsen *et al*., 2002; Xiaoli *et al*., 2010)

The planning of capture plants and energy use of biogas in landfills is initiated by feasibility studies that consider the market for commercialization of energy, infrastructure required for generation and distribution of energy and the potential for methane production of the desired area (Deublein & Steinhauser, 2008; Wellinger *et al*., 2013). This last item depends on estimates of the volume of substrate with potential for conversion into biogas, besides the analysis of physicochemical conditions about the favorability to the process (Manna *et al*., 1999; Kumar *et al*., 2004; Talyan *et al*., 2007; Kamalan *et al*., 2011; Pawtowska, 2014).

The extraction of biogas has a series of vertical wells distributed in various locations of the landfill, which may be constructed as layers of waste disposal are placed, in a system of ramps and soak or subsequently drilled at the end of waste discharge operations (Christensen *et al*., 2011; Pawtowska, 2014). Alternative systems consist of horizontal pipes installed at various depth levels, during the waste disposal, interconnected to horizontal systems.

In any of these systems, efficiency in biogas collection is determined by the permeability of the landfill covering material and the mass of waste (Christensen *et al*., 2011). In the first case, the use of low permeability materials such as clay soils or membranes enables increased efficiency of the collection system in the wells in face of minimizing points of release to the atmosphere.

The second case, as the waste setting occurs by compacting, consumption of organic material or variations in moisture content, occurs a large variation in permeability in the mass of waste, conditions that can generate or eliminate zones of biogas accumulation. At this moment, the application of diagnostic methods to the accumulation of biogas in landfills can provide a substantial increase in the efficiency of the collection system, with the drilling of wells in new areas of accumulation and elimination of points of low biogas flow or contamination by the input of atmospheric oxygen.

The geophysical gathers a group of indirect methods of investigation, some of which are sensitive to the physical properties characteristic to areas of accumulation of gases in the subsurface. This tool is widely used in studies of environmental diagnosis in cases such as investigation of contaminants in soil and groundwater from landfills (Ustra *et al*., 2011; Belmonte-Jiménez *et al*., 2012; Moreira *et al*., 2013; Moreira *et al*., 2014).

Although there are several studies that describe the use of geophysical methods in environmental diagnosis of landfills, most of these works mainly focus on the characterization of the area with percolation of leachate. However, few studies aim to determine relationships among electrical resistivity, natural electrical potential, biological, and physicochemical processes and their relationship to the production of leachate and biogas in landfill (Georgaki *et al*., 2008; Moreira *et al*., 2011).

In this sense, the present study evaluates the potential application of DC Resistivity as a tool for characterization of areas with accumulation of biogas, by means of measurements of electrical resistivity in unsaturated waste layer and crossing with direct measurements of the flow of biogas, in a deactivated waste cell at the landfill in the municipality of Rio Claro (Brazil).

## Materials and methods

*Study Area*

The area of studies consists of landfill of solids residues of the municipality of Rio Claro, São Paulo State, Brazil, distant about 180km from the state capital (Figure 1). The beginning of activities dates from 2001, in an area of approximately 98,000m$^2$ destined for disposal of solid waste, with a daily average of 190 tons and a monthly average of 5,000 tons. In July 2012, the landfill was expanded by the installation of a new cell, currently in use.

The area presents a relief with gentle slope and descending towards the northeast, consisting of sandy soils and sandy clay soils produced by alteration of sandstones belonging to the Rio Claro Formation, covered by siltstones and mudstones gathered in Corumbataí Formation.

The construction scheme of the landfill comprises the local topography and consists of opening individual cells with 200m long and 50m wide, for the excavation of rock types from Rio Claro Formation and from the top of Corumbataí Formation from northeast to southeast direction, with gradients of about 1% to northeast. The landfill has basal and side impermeabilization sealing with a blanket of HDPE 2mm thick. A network to collect and drain the leachate leads the flow by gravity to the terminal boxes, and then to aeration lagoons for treatment.

The waste is dumped directly into cells by tipper trucks of urban collecting, later leveled to horizontal landings by action of bulldozers, daily covered by soil/sediment stored after excavation of the cell, with plastic, rubber, paper and other materials are distributed randomly, together with organic matter (Figure 2A). At this stage, vertical drains are installed for plumbing and atmospheric dissipation of biogas generated by the decomposition process of organic matter in waste, constantly alternated as new levels are built.

The final level is covered by a layer of about 1m of soil/clay pellet, with a slope of 2% for surface water runoff (Figure 2B). Dikes marginal to the limits of the upper level are

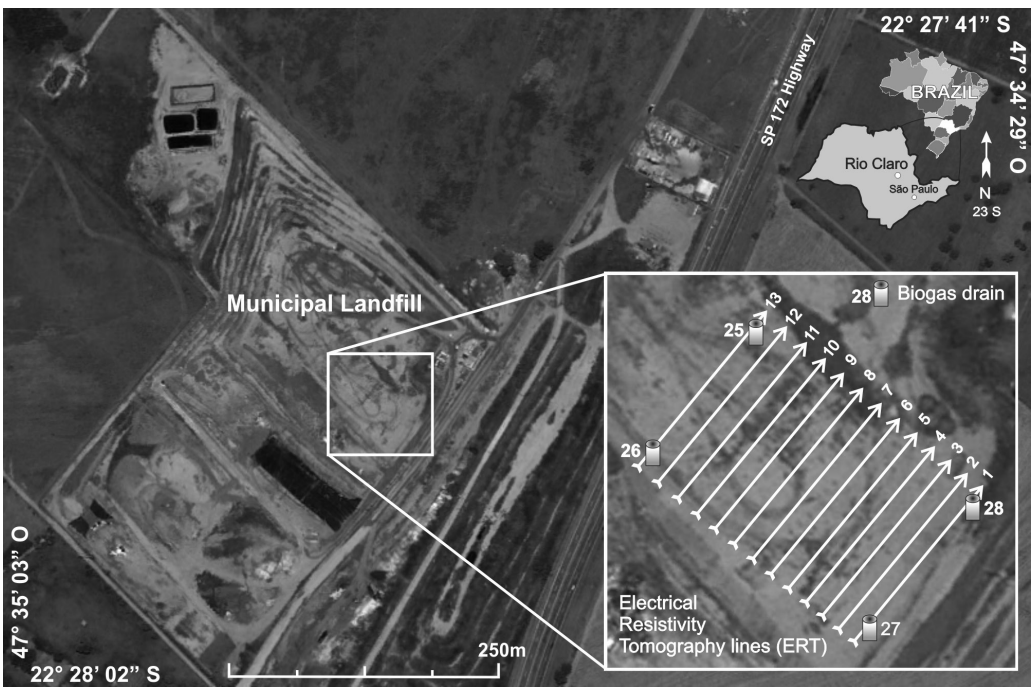


**Figure 1**. Location of the area of studies with position of the lines of data acquisition and drains for measuring the flow of biogas.

built, to direct the flow of rainwater by laminar flow and attenuation processes of lateral erosion (Figure 2C). Drains are ended by steel tubes coated by concrete pipes for burning biogas and dissipation of the generated heat (Figure 2D). Drains are constantly lit for consumption of the biogas by burning in an attempt to prevent accumulation in large scale and minimize the risk of explosion.

Relevant aspects in generating biogas at landfills are represented by forms of packaging waste and operational procedures, content of organic matter in the overall composition of the residue, which can stimulate anaerobic processes. The moisture content is something crucial to the development and metabolism of bacteria, such as agent to transport the nutrients and as a facilitator for colonization of new areas within the landfill scope (Deublein & Steinhauser, 2008; Christensen *et al*., 2011). These factors, combined with physic-chemical conditions, temperature and access to nutrients, directly influence the survival of microorganisms and biogas generation.

The understanding of the genesis of biogas enables some important considerations on the action of processes of anaerobic degradation of organic matter and their effects on physical properties change in the mass of waste.

Biogeochemical reactions are initiated immediately after the coverage of waste in landfills. Organic compounds are oxidized in aerobic processes in shallow locations where aeration is by contribution of atmospheric oxygen or infiltration of rainwater, similar to combustion reactions, generating $CO_2$ and water vapor, both quickly dissipated (Pohland & Gould, 1986).

However, the effect of chemical and biological processes is enhanced by anaerobic digestion in three main stages (Themelis & Ulloa, 2007). At first, there occurs hydrolysis of complex organic matter by the action of fermentative bacteria in soluble molecules. Then, these molecules are converted into simple organic acids such as acetic acid, propionic acid, butyric acid and ethanol, besides $CO_2$ and $H_2$. In the third stage the generation of $CH_4$ by methanogenic bacteria, by breaking acids in $CH_4$ and $CO_2$ or by the reduction of $CO_2$ and $H_2$ occurs.

This exothermic reaction for anaerobic decomposition releases a small amount of heat and produces a gas with average levels of 54% $CH_4$ and 46% $CO_2$. The biogas produced in landfills also contains water vapor near the saturation point, and small amounts of $NH_4$, $H_2$, $H_2S$ and other minor constituents. The

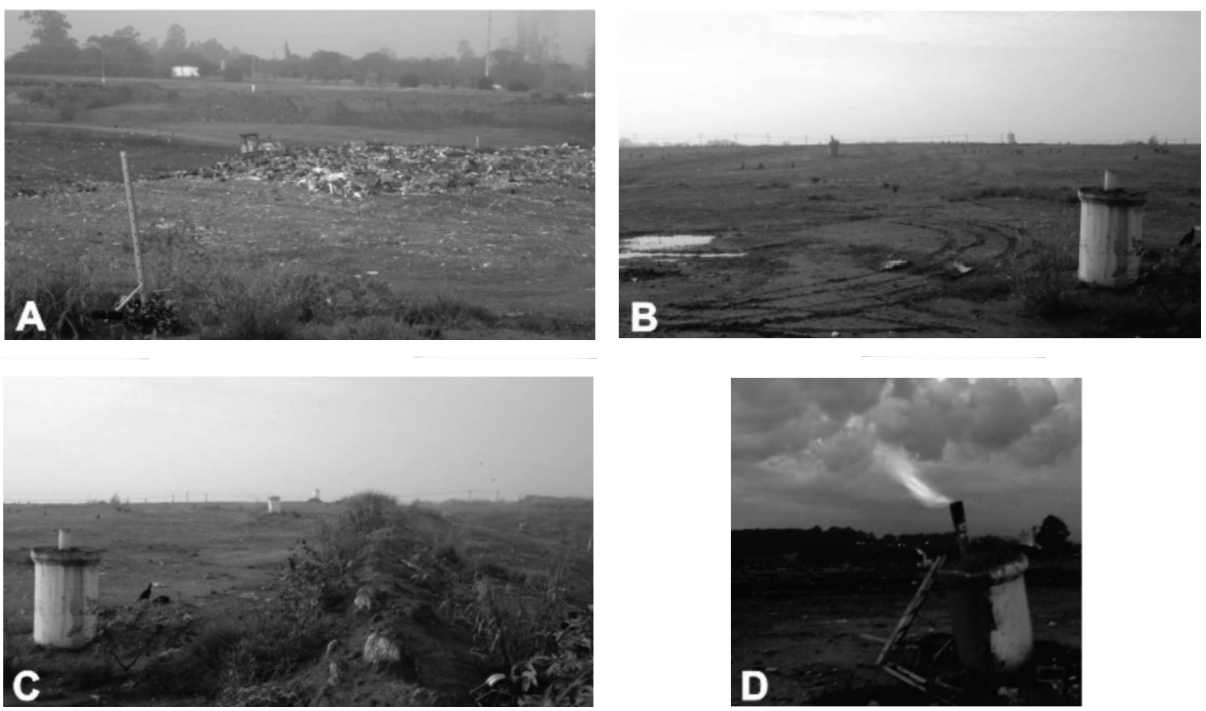


**Figure 2.** A) Waste disposal in active cell. B) Partial view of studied cell. C) Guidance of drains crossed by line 2. D) Drain number 28 with burning of biogas.

maximum amount of biogas can be produced by anaerobic decomposition can be estimated (Equation 1).

$$C_6H_{10}O_4 + 1{,}5H_2O \Rightarrow 3{,}25CH_4 + 2{,}75CO_2 \quad (1)$$

This exothermic reaction releases a small amount of heat and produces a gas consisting of 54% of the $CH_4$ and 46% of the $CO_2$. The biogas produced in landfills also contains water vapor near the saturation point, addition of small amounts of $NH_4$, $H_2$, $H_2S$ and others compounds (Wellinger *et al.*, 2013).

*Methods*

The biogas flow is determined from velocity measurements in the drains, with the aid of a galvanized pipe with standard diameter of 100mm, and a digital thermal anemometer with an accuracy of 0.01m/s.

The procedure initially involved extinguishing the combustion of biogas at the end of the drain hose, coupling of the galvanized pipe to canalize the biogas and introduction of a telescopic handle of the thermo anemometer into a side hole of the tube, located 1m from its upper extremity. This routine was adopted for the protection of the measurement probe from the influences of wind or any air movement that could exert influence on the measurements of biogas velocity, besides standardizing a piping with a single diameter for flow calculation.

Subsequently, was applied DC Resistivity method for geophysical acquisition data, which uses electrodes fixed on the surface of the ground, connected to the measuring instrument via a cable assembly (Keller & Frischknecht, 1966; Telford *et al*., 2004).

Was adopted the Schlumberger arrangement, which consist in the alignment of a series of electrodes and the selection of four electrodes on each measure, where a pair of external electrodes for current transmission and the other internal pair of voltage readings. The lateral movement of this device along with the constant distancing of current electrodes with respect voltage electrodes enables lateral investigations and at various depths, that is, a two-dimensional product.

Were conducted 13 lines of electrical resistivity tomography (ERT) with individual length of 60m, 1.5 m spacing between electrodes and readings at 22 investigation in depths. The Terrameter LS resistivity meter, manufactured by ABEM (Sweden), consists in a single transmission and reception automatic system, calibrated in field to injection of 60mA.

The arrangement of lines in the study area emphasized the proximity of drains emission biogas in an attempt to check the resistivity in their respective areas of influence (Figure 1).

The field assessed measurements were processed in the software Res2dinv and resulted in sections of resistivity in terms of distance x depth, with logarithmic graphical scale and intervals of interpolation of values in color. This is a program that automatically determines a two-dimensional model of the subsurface, from chargeability or resistivity data obtained from ERT (Griffiths & Barker 1993). This optimization aims to reduce the difference between the apparent resistivity values, calculated and measured in the field, by adjusting the resistivity of the block model, which difference is expressed by the error RMS (Root Mean Square) (Loke and Barker 1996).

The data generated after the 2D inversion were gathered in a single file, later used as a database for generating pseudo-3D models and depth maps (Figures 2, 3 and 4). This process was developed in Oasis Montaj platform where 2D data obtained in Res2Dinv program were interpolated and modeled using the kriging method, for enhancement of extreme values in a model of pseudo-3D blocks, where ERT lines were positioned.

**Results and discuccions**

The electrical resistivity measurements were processed in the software Res2dinv and resulted in sections of resistivity in terms of distance x depth, with logarithmic graphical scale and intervals of interpolation of values in color (Figure 3).

The 2D model used in the program divides the pseudo-section into rectangular blocks, which will represent the pseudo-section by the adjustment of the field measurements. This optimization aims to reduce the difference between the apparent resistivity values, calculated and measured in the field, by adjusting the resistivity of the block model, which difference is expressed by the error RMS (Root Mean Square) (Loke and Barker, 1996).

The data generated after the 2D inversion were gathered in a single file, later used as a database for generating pseudo-3D models and depth maps (Figures 3, 4 and 5). This process was developed in Oasis Montaj platform where 2D data obtained in Res2Dinv program were

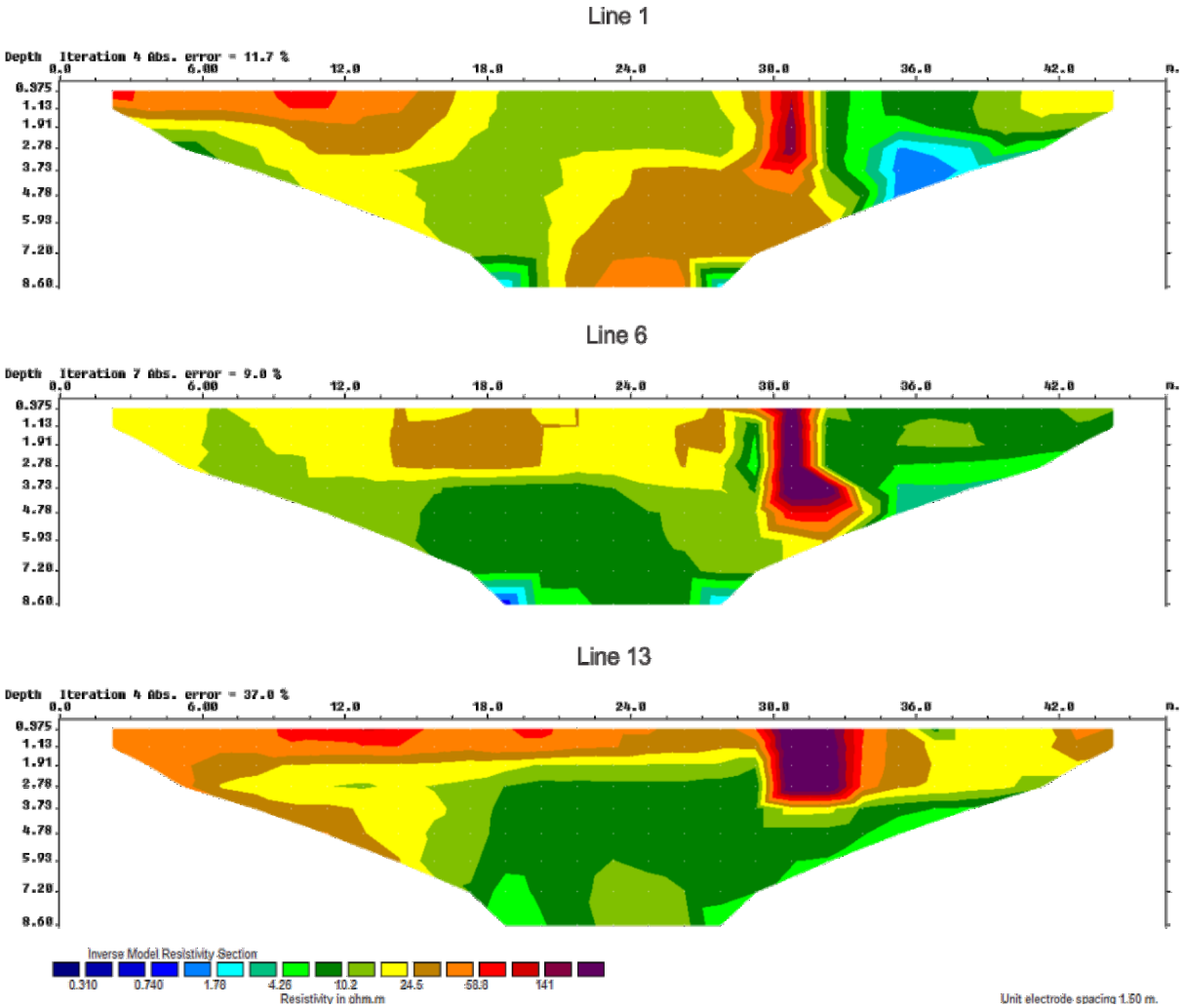


**Figure 3.** Inversion model section for the line 1, line 6 and line 13.

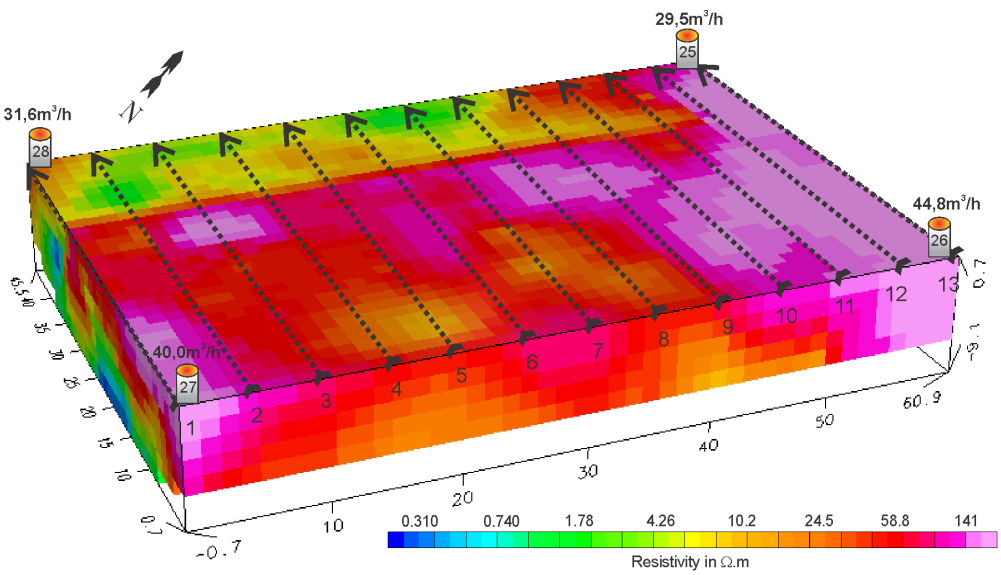


**Figure 4.** Pseudo 3D model of the electrical resistivity, with position of ERT lines, biogas drain with respectively flow (in m³/h).

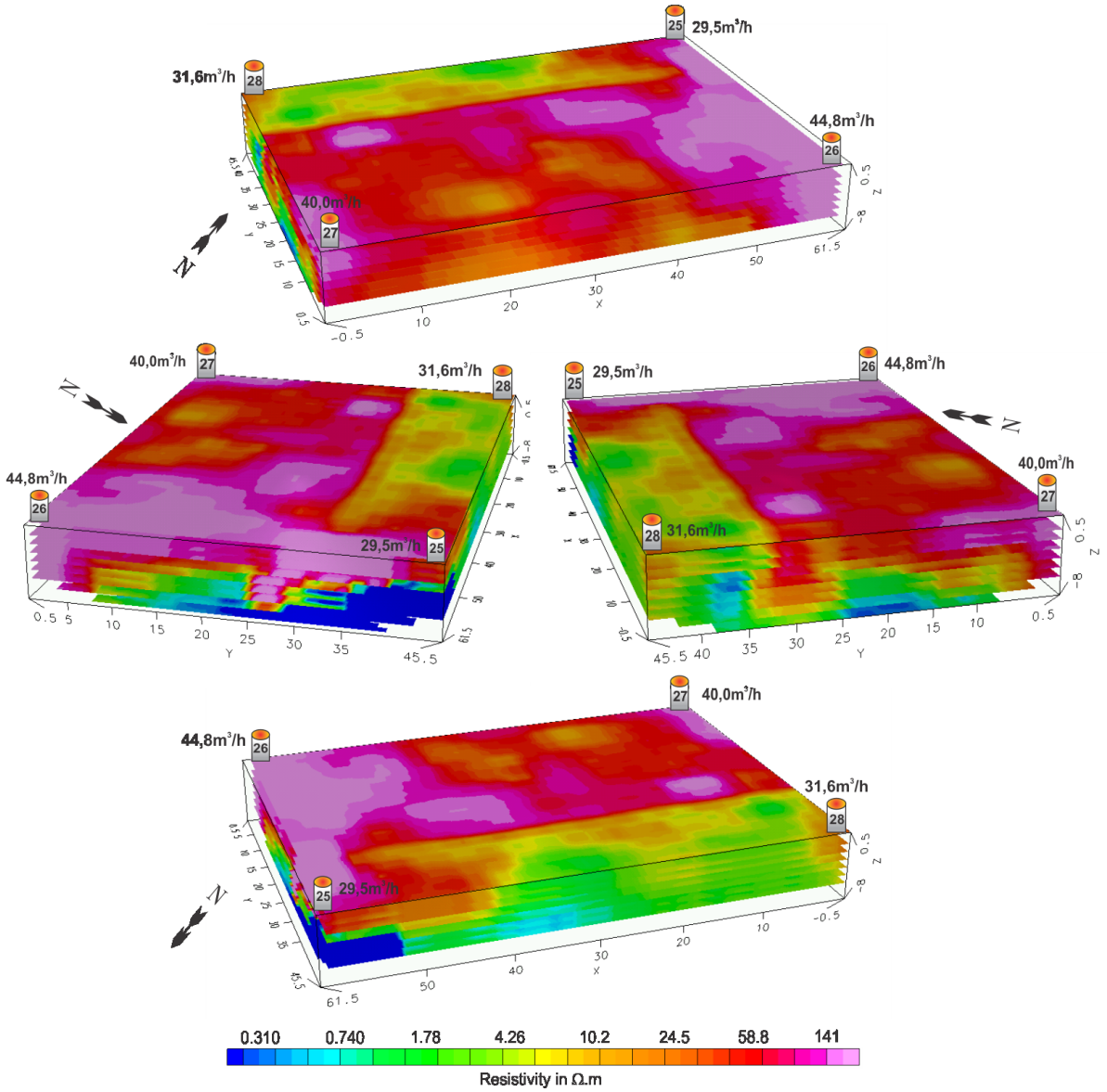


**Figure 5.** Isosurface levels of the electrical resistivity in various viewing perspective, with biogas drain and respectively flow (in $m^3/h$).

interpolated and modeled using the kriging method, for enhancement of extreme values in a model of pseudo-3D blocks, where ETR lines were positioned.

Even on a relatively small area (60x40m), drains with a constructive profile, catchment area of gas and similar lengths, the data obtained show a wide variation in the biogas flow. Covering material of the landfill area consists of soil from excavation and opening of waste discharge cells characterized by clay matrix, released on waste and subsequently compressed by steamroller.

Although arranged in horizontal layers with thickness of 5m, the great heterogeneity of the waste in compositional terms, should necessarily lead to settlements differentiated over the time due to factors such as consumption of organic matter or rearrangement of material by seasonal moisture changes due to rain or drought seasons.

Such conditions can cause the generation of fractures in the coating material and the fugitive emission of part of the biogas produced, differential permeability and possible accumulation in specific areas. In this scenario

13 lines of electrical resistivity tomography, grouped into pseudo-3D models, with placement of drains biogas and their respective flow rates were performed (Figure 4).

The results enable a 3D view of the geophysics data and their relations with the flow of biogas and the special arrangement of the drains. The depth reached in models of 2D inversion was 9,1m, maintained in the 3D block.

A preliminary analysis from an aerial view of the 3D block shows an area of high resistivity (141W.m) between the drains 25 and 26, besides another isolated area of high resistivity positioned in the surroundings of drain 27 (Figure 4). An elongated and continuous strip between the drains 25 and 28, limited to the end of lines 1 and 11, is characterized by low resistivity values (24.5W.m), and comprises the area around the drain 28.

The 3D visualization of this product in different special positions allows for greater inferential about the resistivity areas (Figure 5).

For the drain 26, characterized by increased flow in the study area (44.8m$^3$/h), its catchment area in the vicinity and its continuity until 9m depth are fully characterized by high resistivity values (141W.m).

In contrast, the drain 28 had the lowest flow (29.5m$^3$/h), crosses depths levels with large variations in resistivity. In the first 2m of depth, there occur high resistivity values (141W.m), which brusquely fall to very low values from 4m depth (0.3W.m).

The drain 27 is characterized by an elevated flow (40.0m$^3$/h) and similarly to the drain 26 crosses an area of high resistivity values. However, below a depth of 7m there is a reduction in resistivity patterns, which gradually pass from 141W.m to values near 58W.m.

The flow tube 28 presented slightly higher flow than the lowest flow and in similarity to the drain 25, presents large variations in resistivity with the increase in depth. The first 3m depth are characterized by values ranging from 24W.m and 10W.m with gradual reduction in resistivity with increasing depth until values near 1.78W.m.

The joint analysis of the results indicate a strong correlation between high resistivity values and drains with larger flows of biogas, while there is the prevalence of low resistivity values in regions of lower flow drains. The uptake in areas of high resistivity along the entire depth of the drains in depth is another factor that affects the high flow rate. As levels of resistivity below 141W.m occur or become predominant, there occurs a concomitant decrease in the flow of biogas.

In this sense, the areas of high resistivity should characterize zones of accumulation of biogas, which predominance in mass residues in void spaces rather than the accumulation of manure, result in an increased resistivity, attributed to the insulating character of the gases to the passing of electric current.

This principle is adopted in geophysical profiling in studies of hydrocarbons, where physical parameters such as electrical resistivity and spontaneous potential are routinely employed in investigations of exploratory drill holes or for detailing of oilfields, due to the possibility of estimating lithological parameters such as permeability, porosity, grain size, rock types, besides the presence of oil or gas (Asquith & Gibson, 1982).

**Conclusion**

Measures in the drains describe a wide variation in biogas flow in a relatively small area, possibly due to issues related to settlement by fouling, decomposition of organic matter and accommodation of waste, changes in the pattern of permeability and generation of zones of accumulation of gases.

This latter aspect was subject to evaluation by means of analyzing measurements of electrical resistivity for various levels of depth and laterally among the lines of data acquisition. Biogas is characterized as an electrical insulator due to its physical state, i.e., areas where there is accumulation of biogas, as part of the waste must be characterized by high resistivity values. Measures of biogas flow corroborate this effect, resulting in a correlation between high flow rates and high resistivity values.

In contrast, degradation of organic matter also produces leachate, due to the loss of moisture in the process. In this sense, the intervals of low resistivity may reflect areas of leachate accumulation, characterized by high amounts of dissolved salts. In addition, it should be considered contributions to increased moisture from infiltration of rainfall at certain times.

The high heterogeneity of the waste, with plastic and other high resistivity materials randomly distributed, and the continuous process of accommodation of materials result in constant changes in permeability, with generation of new areas of accumulation of biogas and extinction of others (Metcalfe & Farquhar 1987; Nastev et al. 2001).

The results of this study demonstrate the effectiveness of the DC resistivity in determining areas of accumulation of gases in landfills, besides the possibility of continuous monitoring of biogas capture systems with a history of change of flows. However, the intrinsic complexity to waste disposed in landfills in terms of composition and compaction, are conditions of great influence in electrical resistivity measurements.

Eventual variations related to changes in the permeability and transmissivity of gases can be estimated by measurements of electrical resistivity, whose analysis and comparison with available flowrates, enables the location of new potentially effective points, to drilling and installing drains for collection of biogas. This procedure may help in optimizing the processes of energy production from burning biogas from landfill, besides the possibility of application in the detection of areas of potential occurrence of fugitive emissions, which result in the escape of gases to the atmosphere.

**References**


Asquith G.B., Gibson C.R. 1982, Basic Well Log Analysis for Geologists. Oklahoma, American Association of Petroleum Geologists, 234 pp.

Belmonte-Jiménez S., Jimenez-Castañeda M.E., Pérez-Flores M.A., Campos-Enríquez J., Reyes-López J.A., Salazar-Peña L., 2012, Characterization of a leachate contaminated site integrating geophysical and hydrogeological information. Geofísica Internacional, 51, 4, 309-321.

Deublein D., Steinhauser A., 2008, Biogas from waste and renewable resources. Mörlenbach, Wiley-VCH Verlag, 450pp.

Georgaki I., Soupios P., Sakkas N., Ververidis F., Trantas E., Vallianatos F., Manios T., 2008, Evaluating the use of electrical resistivity imaging technique for improving $CH_4$ and $CO_2$ emission rate estimations in landfills, *Science of the Total Environment*, 389, 522-531.

Griffiths D.H., Baker R.D., 1993, Two-dimensional resistivity imaging and modeling in areas of complex geology, *Journal of Applied Geophysics*, 29, 2, 211-226.

International Energy Agency – IEA, 2011, Renewable Energy: Policy Considerations for deploying renewables. Paris, IEA, 76pp.

International Energy Agency – IEA, 2014, Energy Technology Perspectives 2014. Paris, IEA, 382pp.

Kamalan H., Sabour M., Shariatmadari N., 2011, A review on available landfill gas models. *Journal of Environmental Science and Technology*, 4, 79-92.

Keller G.V., Frischknecht F.C., 1966, Electrical methods in geophysical prospecting. Pergamon Press, Oxford, 562pp.

Kjelden P., Barlaz M.A., Rooker A.P., Baun A., Ledin A., Christensen T.H., 2002, Present and long-term composition of MSW landfill leachate: a review. Critical Reviews in Environmental Science and Technology, 32, 297-336.

Kumar S., Gaikwad S.A., Shekdar A.V., Kshirsagar P.S., Singh R.N., 2004, Estimation method for national methane emission from solid waste landfills. *Atmospheric Environmental*, 38, 3481-3487.

Loke M.H., Baker R.D., 1996, Rapid least-squares inversion of apparent resistivity pseudosections by quasi-Newton method, *Geophysical Prospecting*, 44, 131-152.

Manna L., Zanetti M.C., Genon G., 1999, Modeling biogas production at landfill site. Resources, *Conservation and Recycling*, 26, 1-14.

Metcalfe D.E., Farquhar G.J., 1987, Modeling gas migration through unsaturated soils from waste disposal sites. Water, Air and Soil Pollution, 32, 247-259.

Moreira C.A., Braga A.C.O., Hansen M.A. F., 2011, Time estimative of the leachate production in control landfill by electrical resistivity measuring, Revista Brasileira de *Geociências*, 41, 3, 549-557.

Moreira C.A., Braga A.C.O., Godoy L.H., Sardinha D.S., 2013, Relationship between age of waste and natural electric potential generation in Sanitary Landfill, *Geofísica Internacional*, 52, 4, 375-383.

Moreira C., Castro M., Gonsalez A., Cavallari F., Munhoz T., Pereira A., 2014, Comparative Analysis between Biogas Flow in Landfill and Electrical Resistivity Tomography in Rio Claro City, Brazil. *Journal of Geological Research*, Article ID 845906, http://dx.doi.org/10.1155/2014/845906

Nastev M., Therrien R., Lefebvre R., Gélinas P., 2001, Gas production and migration in landfill and geological materials. *Journal of Contamination Hydrology*, 52, 187-211.

Nozhevnikova A.N., Lifshitz A.B., Lebedev V.S., Zavarzin G.A., 1993, Emission of methane into the atmosphere from landfill in the former USSR. *Chemosphere*, 26, 401-417.

Pawlowska M., 2014, Mitigation of landfill gas emissions. CRC Press/Balkema, London, 118pp.

Pohland F.G., Gould J.P., 1986, Co-disposal of municipal refuse and industrial waste sludge in landfills, *Water Science Technology*, 18, 12, 177-192.

Smil V., 2008, Energy in Nature and Society: General Energetics of Complex Systems. The MIT Press, London, 495pp.

Talyan V., Dahiya R.P., Anand S., Sreekrishnan T.R., 2007, Quantification of methane emission from municipal solid waste disposal in Delhi. Resources, *Conservation and Recycling*, 50, 240-259.

Tchobanoglous G., Theisen H., Vinil S., 1993, Integrated solid waste management. Engineering principles and management issues. Irwin MacGraw-Hill, New York, 978pp.

Telford W.M., Geldart L.P., Sheriff R.E., 2004, Applied Geophysics. Cambridge University Press, New York, 774pp.

Themelis N.J., Ulloa P.A., 2007, Methane generation in landfills, *Renewable Energy*, 32, 1243-1257.

Ustra A.T., Elis V.R., Mondelli G., Zuquette L.V., Giacheti H.L., 2011, Case study: a 3D resistivity and induced polarization imaging from downstream a waste disposal site in Brazil, *Environmental Earth Sciences*, 66, 763-772.

Xiaoli C., Ziyang L., Takayuki T., Nakayama H., Ying Z., Xiaoyan C., Komiya T., Ishizaki T., Youcai Z., 2010, Characteristics of environmental factors and their effects on CH4 and CO2 emissions from a closed landfill: An ecological case study of Shanghai. Waste Management, 30, 446-451.

Wellinger A., Murphy J., Baxter D., 2013, The biogas handbook: science, production and applications. Woodhead Publishing Limited, Cambridge, 501pp.

Geofísica Internacional (2015) 54-4: 363-386

Original paper

# Papanoa, Mexico earthquake of 18 April 2014 ($M_w$7.3)

UNAM Seismology Group
(with contribution from Universidad Autónoma Metropolitana, Azcapotzalco, Mexico D.F.)

Received: January 13, 2015; accepted: July 07, 2015; published on line: October 01, 2015

**Resumen**

El sismo de Papanoa rompió la interfase de la placa al noroeste de la brecha sísmica de Guerrero. En esta región, los grandes sismos anteriores ocurrieron en 1943 ($M_S$ 7.4), 1979 ($M_w$7.4) y 1985 ($M_w$7.5). El terremoto se registró en la región cercana a la fuente por varios acelerógrafos. Daño severo se reportó en Papanoa (donde *PGA* regisrado en una de las componentes horizontales en un sitio blando fue de ~ 0.9 g) y otras ciudades costeras cercanas. También se sintió con fuerza en la Ciudad de México, donde los movimientos de tierra fueron comparables a los registrados durante los sismos de 1979 y de 1985.

Con un análisis cuidadoso de datos cercanos a la fuente, incluyendo la polarización de la onda *P*, se obtiene un epicentro en 17.375 ºN, 101.055 ºW, cerca de la costa y de la localidad de Papanoa. La duración efectiva del movimiento del suelo en las estaciones costeras cercanas a la fuente, al NW del epicentro, es 10 a 15 s, mientras que es de 20 a 35 s en las estaciones del SE, lo que demuestra la directividad de la ruptura hacia Zihuatanejo. Tres (en algunos casos sólo dos) emisiones de radiación de alta frecuencia son visibles en los acelerogramas. Los registros de campo cercano muestran que el deslizamiento fue pequeño durante los primeros 2-3 s de la ruptura que, posteriormente, fue seguido de dos o tres subeventos más grandes en cascada. La inversión del deslizamiento a partir de ondas de telesísmicas, junto con los datos GPS de un par de sitios cercanos a la fuente, revela que la ruptura consistió principalmente de dos subeventos. El primero estuvo centrado cerca del hipocentro y tuvo un radio de ~ 15 km. El segundo evento, más o menos de la misma dimensión que el primero, se centró ~ 25 km al SSE de Zihuatanejo. Un análisis previo de tres eventos de deslizamiento lento (SSE) en la región (2001-2002; 2006; 2009-2010) había revelado que esta región tiene un acoplamiento alto (> 0.5) en el período inter-SSE, con un déficit de deslizamiento cerca de cuatro veces mayor que en la brecha sísmica NW de Guerrero (Radiguet *et al*., 2012). Parece que el deslizamiento grande correspondiente al primer subevento del sismo de 2014 experimentó un deslizamiento acumulado de ~ 20 cm durante los SSE, lo que sugiere que el deslizamiento sísmico y los SSE pueden compartir la misma zona de la interfase. Alternativamente, el deslizamiento durante el SSE puede haber ocurrido en un área que rodea la region del deslizamiento grande, lo que parece un modelo físicamente más plausible.

Los epicentros de las réplicas ($M \geq 3.5$), que se produjeron en las próximas 36 horas, definen un área rectangular de ~ 40 km × 70 km, orientada ~ N75ºE; cerca de la mitad de esta región se encuentra en tierra. Esta zona encierra la región de deslizamiento obtenida en la inversión. Más de la mitad de la zona de réplicas se sobrepone con la del sismo de 1979 y una pequeña fracción con la del sismo 21 de septiembre 1985. Como sólo conocemos la distribución del deslizamiento del sismo de 2014, no se sabe si las dos regiones de gran deslizamiento también se deslizaron de

Instituto de Geofísica
Universidad Nacional Autónoma de México
Circuito de la Investigación Científica s/n
Ciudad Universitaria
Delegación Coyoacán, 04510
*México D.F. México*

Servicio Sismológico Nacional
Universidad Nacional Autónoma de México
Circuito de la Investigación Científica s/n
Ciudad Universitaria
Delegación Coyoacán, 04510
*México D.F. México*

Instituto de Ingeniería
Universidad Nacional Autónoma de México
Circuito de la Investigación Científica s/n
Ciudad Universitaria
Delegación Coyoacán, 04510
*México D.F. México*

*Departamento de Sismología*
Instituto de Geofísica
Universidad Nacional Autónoma de México
Circuito de la Investigación Científica s/n
Ciudad Universitaria
Delegación Coyoacán, 04510
*México D.F. México*
**Corresponding autor: krishnamex@yahoo.com*

manera similar durante los sismos anteriores.
El sismo fue seguido por dos sismos moderadamente grandes que se produjeron el 8 de mayo ($M_w$6.5) y 10 de mayo ($M_w$6.1). Los epicentros de estos eventos caen cerca de Tecpan, dentro de la brecha sísmica NW de Guerrero (que se extiende de 100 ºW a 101 ºW), fuera de la zona de réplicas del sismo de Papanoa. No ha ocurrido un gran sismo en esta zona de la brecha, entre Papanoa y Acapulco, desde los acontecimientos de 1899 ($M_S$7.5) y 1911 ($M_S$7.6). Sin embargo, la sismicidad en la región (en niveles de $M_w \geq 5$) parece normal. Se han identificado pocos sismos moderados de duración inusualmente grande y con radiación de alta frecuencia deficiente cerca de la trinchera. En contraste con la region de Papanoa - Zihuatanejo, en este segmento se tiene un acoplamiento inter-SSE, desde unos 10 km al interior hacia el mar, muy bajo (< 0.2) y el déficit de deslizamiento es aproximadamente una cuarta parte del de la región Papanoa- Zihuatanejo (Radiguet *et al*., 2012). Como consecuencia, el período de recurrencia esperado de grandes sismos puede ser relativamente largo, de acuerdo con la sismicidad de la región Papanoa-Acapulco.

Palabras clave: sismo de Papanoa, movimientos fuerte, evento de deslizamiento lento, brehas sísmica de Guerrero.

**Abstract**

Papanoa earthquake broke the plate interface NW of the Guerrero seismic gap. In this region, previous large earthquakes occurred in 1943 ($M_S$ 7.4), 1979 ($M_w$7.4) and 1985 ($M_w$7.5). The earthquake was recorded in the near-source region by several accelerographs. Severe damage was reported in Papanoa (where *PGA* of ~ 0.9 g was recorded on one of the horizontal components at a soft site) and other nearby coastal towns. It was also felt strongly in Mexico City where the ground motions were comparable to those recorded during the 1979 and 1985 events.
A careful analysis of the near-source data, including *P*-wave polarization, yields an epicenter at 17.375 ºN, 101.055 ºW, close to the coast, near the town of Papanoa. Effective duration of ground motion at near-source coastal stations to the NW of the epicenter is 10-15 s, while it is 20-35 s to the SE, demonstrating rupture directivity towards Zihuatanejo. Three (in some cases only two) bursts of high-frequency radiation are visible in the accelerograms. Near-field records show that the slip was small during the initial 2-3 s of rupture which, subsequently, cascaded in two or three larger subevents. Slip inversion using teleseismic waves, along with GPS data from a couple of near-source sites, reveals that the rupture mainly consisted of two subevents. The first one was centered close to the hypocenter and had a radius of ~ 15 km. The second subevent, roughly of the same dimension as the first, was centered ~ 25 km SSE of Zihuatanejo. Previous analysis of three slow slip events (SSEs) in the region (2001-2002; 2006; 2009-2010) had revealed that this region had a high inter-SSE coupling ratio (> 0.5) with a slip deficit about four times greater than in the adjacent NW Guerrero seismic gap (Radiguet *et al*., 2012). It seems that the large slip patch corresponding to the first subevent of the 2014 earthquake experienced a cumulative slip of ~ 20 cm during the SSEs, suggesting that seismic and SSE slip may share the same area of the interface. Alternatively, the SSE slip may have occurred over an area surrounding the large slip patch, a physically more plausible model.
Epicenters of aftershocks ($M \geq 3.5$), which occurred in the next 36 hours, define a rectangular area of ~ 40 km × 70 km, oriented ~ N75ºE; about half of this area lies onshore. This area encloses the inverted slip region. More than half of the aftershock area overlaps with that of the 1979 earthquake and a small fraction with that of the 21 September 1985 earthquake. As we only know the slip distribution of the 2014 earthquake, it is not known if the two large-slip patches had also slipped similarly during the previous earthquakes.
The earthquake was followed by two moderately large events that occurred on 8 May ($M_w$6.5) and 10 May ($M_w$6.1). The epicenters of these events fall near Tecpan, within the NW Guerrero seismic gap (which extends from 100 ºW to 101 ºW), outside the aftershock area of the Papanoa earthquake. No large earthquake has occurred in this part of the gap, between Papanoa and Acapulco, since the events of 1899 ($M_S$7.5) and 1911 ($M_S$7.6). However, seismicity in the region (at $M_w \geq 5$ level) appears normal. A few moderate earthquakes of unusually large duration and deficient high-frequency radiation have been identified near the trench. In contrast to the Papanoa – Zihuatanejo region, in this segment the inter-SSE coupling ratio from ~ 10 km inland towards sea is very low (< 0.2) and the slip deficit is about one-fourth that of the Papanoa- Zihuatanejo region (Radiguet *et al*., 2012). As a consequence, the expected recurrence period of large/great earthquakes may be relatively long, in agreement with the seismicity of the Papanoa-Acapulco region.

Key words: Papanoa earthquake, strong motion, slow-slip event, seismic gap of Guerrero.

## Introduction

Seismic activity was very intense along the Guerrero segment of the Mexican subduction zone between 1899 and 1909. During this period seven large/great earthquakes occurred on the plate interface between ~ 99 ºW and 101 ºW [24 Jan. 1899, $M_S$7.5; 15 Apr. 1907, $M_S$7.7, $M_w$7.9; 26 Mar. 1908, $M_S$7.6, $M_w$7.5; 27 Mar. 1908, $M_S$7.0, $M_w$7.2; 30 Jul. 1909; $M_S$7.3, $M_w$7.5; 31 Jul. 1909, $M_S$6.9, $M_w$7.0; 16 Dec. 1911, $M_S$7.6, $M_w$7.6] (Figure 1) (Appendix A). Instrumental locations of these earthquakes are very poor. The damage and felt reports along the Guerrero coast of Mexico of some of these events are not extensive enough to delineate their rupture areas with confidence. The exceptions are the earthquakes of 1907 and 1909 whose rupture areas were near the towns of San Marcos (~ 99.2 ºW) and Acapulco (~ 100 ºW), respectively (Appendix A). Thus, there is little doubt that the plate interface near Acapulco and SE of it broke during some of the events of the 1899-1911 sequence. The damage reports also suggest, *albeit* less conclusively, that 1899 and 1911 earthquakes ruptured the interface NW of Acapulco between 100 ºW and 101 ºW.

The segment between ~ 99 ºW and 100 ºW experienced large earthquakes on 11 May 1962 ($M_S$7.0, $M_w$7.2), 19 May 1962 ($M_S$6.7, $M_w$7.2), 28 Jul. 1957 ($M_S$7.5, $M_w$7.7), and 25 Apr. 1989 ($M_w$6.9) (Figure 1). However, no large earthquake ($M_w \geq 7.0$) has occurred between 100 ºW and 101 ºW at least since 1911. Immediately to the NW of 101 ºW, the plate interface ruptured in 22 Feb. 1943 ($M_S$7.5, $M_w$7.4), 14 Mar. 1979 ($M_w$7.4), and 21 Sep. 1985 ($M_w$7.5) (Figure 1). Based on this seismic history, the segment from ~ 99 ºW to 101 ºW was designated a seismic gap and was called the Guerrero seismic gap (Singh *et al*., 1981). The fact that the occurrence of large earthquakes is clearly documented between ~ 99 ºW and 100 ºW but is uncertain between ~ 100 ºW and 101 ºW, it is convenient to divided the gap in two segments: the NW segment extending from ~ 100 ºW to 101°W, henceforth called the NW Guerrero gap, and the SE segment from 99 ºW to 100 ºW, henceforth denoted as the SE Guerrero gap (Ortiz *et al*., 2000). Since recurrence period of large earthquakes along the Mexican subduction zone is about 30 to 60 years (Singh *et al*., 1981), the SE Guerrero region may also be considered a mature seismic gap.

Anticipation of large/great earthquakes in the region led to the installation of Guerrero Accelerographic Array in 1985 (Anderson *et al*., 1986, 1994). Soon after the completion of the array, the Michoacán earthquakes of 19 and 21 September1985 ($M_w$8.0, 7.5) ruptured the plate interface NW of the seismic gap. The earthquake of 19 September 1985 caused unprecedented damage and death in Mexico City, which led to increased concern about the occurrence of similar earthquakes in Guerrero. As a consequence, the accelerographic and seismic networks in the region were improved and strengthened, and a seismic alert system for Mexico City, triggered by earthquakes in the gap, became operational. A seismic network was operated during 1987-1993 to monitor the seismicity and to map the geometry of the subducted Cocos plate beneath the region (Suárez *et al*., 1990). In a collaborative effort among Caltech, U.C. Los Angeles and UNAM, called the MesoAmerican Subduction Experiment (MASE), a portable array of 100 broadband seismographs, spaced 5 km apart, was operated between Acapulco and Tampico during 2005-2007 (Pérez-Campos *et al*., 2008). Analysis of the data produced by the permanent networks, and temporary and portable arrays has resulted in a much improved knowledge of seismicity and seismotectonics of the region, including the geometry of the subducted Cocos plate (e.g., Suárez *et al*., 1990; Singh and Pardo, 1993; Pardo and Suárez, 1995; Pérez-Campos *et al*., 2008; Song *et al*., 2009; Husker and Davis, 2009; Pacheco and Singh, 2010). Seismicity and focal mechanisms in the Guerrero segment, based on local and regional data, reveal that the Cocos plate subducts below Mexico at a shallow angle, reaching a depth of 25 km at a distance of 65 km from the trench (~ 5-10 km inland from the coast). An unbending of the slab begins at this distance. The slab becomes horizontal at a distance of ~ 120 km at a depth of 40 km. Earthquakes and focal mechanisms shown in Figure 1b, based on Table 1 of Pacheco and Singh (2010), summarizes the seismicity and seismotectonics of the region: (a) a relatively wide band (~ 60-65 km) of shallow–dipping thrust events which extends from near the trench up to the coast, (b) a narrow band of events about 15-25 km inland in the depth range of 25-40 km, mostly exhibiting downdip compression, (c) a hiatus in the inslab seismicity from about 85 to 160 km from the trench and a resumption of normal-faulting earthquakes which, finally, cease at a distance of ~ 240 km. There is also evidence of a thin (~ 3-5 km) ultraslow velocity, high-pore pressure fluid layer at the top of the subducted oceanic crust of the slab (Song *et al*., 2009; Kim *et al*., 2010).

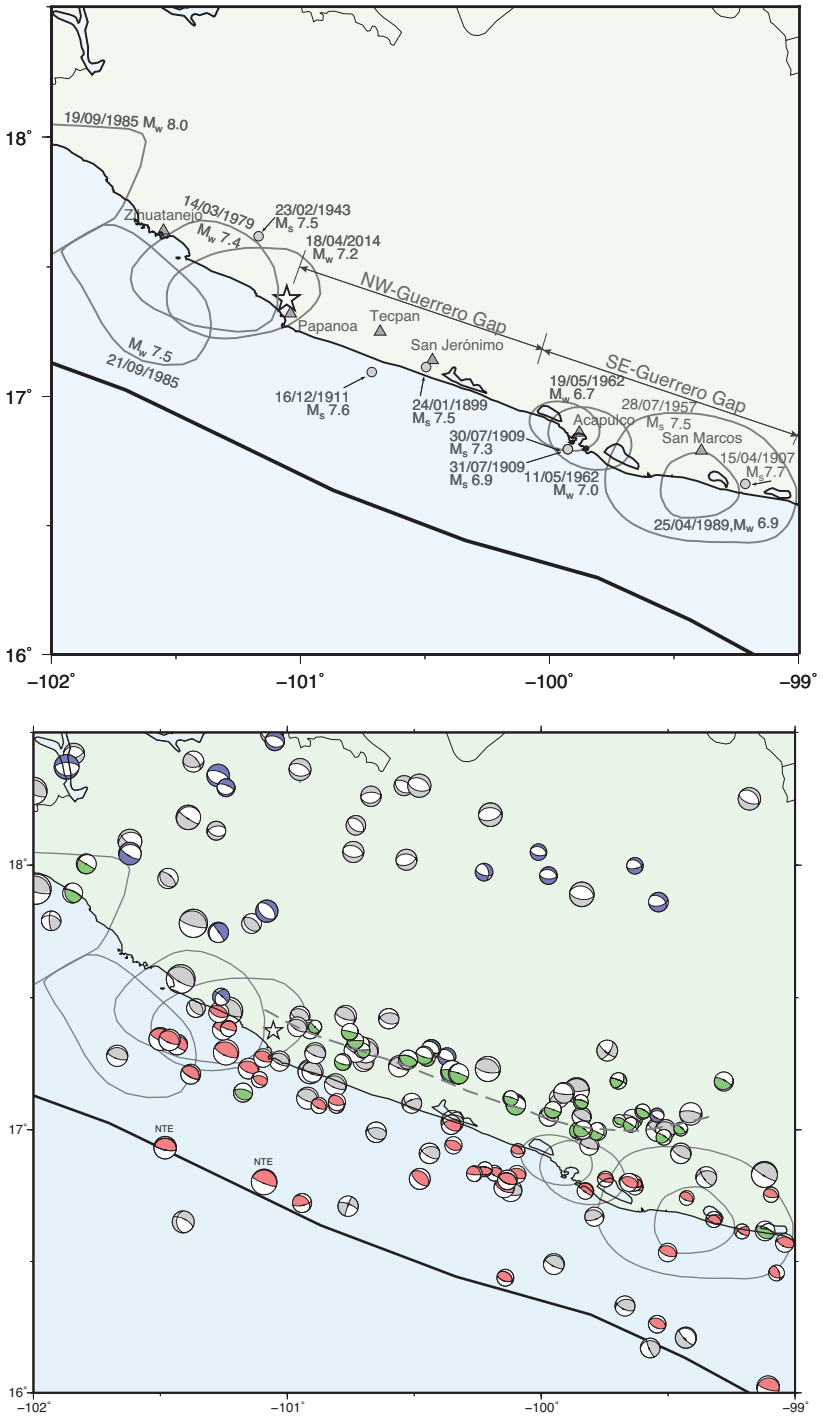


**Figure 1.** (a) Tectonic setting and epicenter or estimated rupture areas of large earthquakes in and near Guerrero segment of the Mexican subduction zone. The epicenters of 1899-1911 earthquakes have large uncertainty (Appendix A). Earthquakes of 1908 fall outside the area covered by the map. Lack of large earthquakes since at least 1911 between ~100 ºW – 101 ºW defines the NW Guerrero seismic gap. Except for the doublet of 1962 (MS7.1, 7.1) and the earthquake of 1989 (Mw6.9), no large/great event has occurred inthe segment between ~99 ºW – 100 ºW since 1957. This segment is designated as the SE Guerrero seismic gap. (b) Focal mechanisms of well-located earthquakes using local and regional data (adopted from Pacheco and Singh, 2010) are shown at their epicenters in red (shallow-dipping thrust), green (steeply-dipping thrust), and blue (normal fault). Epicenters and mechanisms of earthquakes in grey are taken from global CMT catalog; the locations of these events are not well determined from local and regional data. Dashed green line defines the transition between shallow-dipping interplate and steeply-dipping intraslab earthquakes. NTE: near-trench earthquakes with deficient high-frequency radiation and large centroid delay time.

**Table 1.** Source parameters of the 18 April 2014, Papanoa, Mexico earthquake.

| Source | Lat., °N | Lon., °W | Depth, km | Strike, ° | Dip, ° | Rake, ° | $M_0$, Nm |
|---|---|---|---|---|---|---|---|
| This study | 17.375 | 101.055 | 15* | - | - | - | - |
| SSN | 17.182 | 101.195 | 18.0 | - | - | - | - |
| Regional *W*-phase+ | 17.35 | 101.230 | 21.5 | 300 | 23 | 95 | $8.58\times10^{19}$ |
| NEIC | 17.397 | 100.972 | 10 | - | - | - | - |
| USGS, CMT | 17.397 | 100.972 | 10 | 312 | 23 | 114 | $7.72\times10^{19}$ |
| USGS, *W*-phase, CMT | 17.397 | 100.972 | 21.5 | 302 | 20 | 99 | $8.49\times10^{19}$ |
| Global CMT | 17.55 | 101.25 | 18.9 | 303 | 18 | 98 | $1.00\times10^{20}$ |

* Depth fixed.
+ Based on a real-time algorithm implemented at Institute of Geophysics, UNAM, which uses regional waveforms recorded on SSN broadband stations. The depth was fixed in the inversion and a grid search was performed for the centroid location.

The region is also equipped with a sparse distribution of continuous GPS stations. This network has detected the occurrence of large, slow seismic events (SSEs) in the region with a periodicity of ~ 4 years: in 1997-1998, 2001-2002, 2006, and 2009-2010 (e.g., Lowry *et al*., 2001; Kostoglodov *et al*., 2003; Iglesias *et al*., 2004; Yoshioka *et al*., 2004; Kostoglodov *et al*., 2010; Radiguet *et al*., 2011; Radiguet *et al*., 2012). In these episodes the slow slip in NW Guerrero was not only confined to the near-horizontal segment of the plate interface but extended to the updip portion of the slab up to ~ 10 km inland from the coast, at least for the 2006 event (Radiguet *et al*., 2011; Cavalié *et al*., 2013). The source inversion shows that part of the slip area may have extended offshore. Radiguet *et al*. (2012) and Cavalié *et al*. (2013) report that, due to such aseismic energy release, the secular slip deficit in the seismogenic zone of the NW Guerrero seismic gap is one fourth of the adjacent segments, suggesting that this may be the reason for longer recurrence period in the segment. The most recent SSE in the region began in January, 2014. The 18 April 2014 Papanoa earthquake ($M_w$7.3) occurred during this SSE episode.

In the context of the SSEs and other related phenomena (e.g., tectonic tremors) observed in the region, and the concern over the seismic potential of the Guerrero seismic gap, a detailed study of the Papanoa earthquake acquires special interest. In this paper, we present an analysis of the earthquake and the subsequent seismic activity in the region based, mostly but not exclusively, on local and regional data.

## Earthquake of 18 April 2014

*Local recordings and the location of the earthquake*

In and near the epicentral region, there were two permanent broadband stations (ZIIG and CAIG) belonging to Servicio Sismológico Nacional (SSN, Mexican Seismological Service), which are also equipped with accelerometers and GPS receivers, and four accelerographic stationsbelonging to the Institute of Engineering, UNAM (PET2, SLU2, NUX2, and SUCH) (Figure 2). In addition, there were four accelerographic stations (GR01, GR02, GR13, GR14), belonging to the Mexican seismic alert system (SASMEX), which recorded the event. SASMEX data could not be used in location and in quantitative analyses since these accelerograms did not have absolute time and the quality of recordings was relatively poor. The broadband seismograms at ZIIG and CAIG were clipped during the mainshock. We used accelerograms at these stations in our analysis.

The location of the earthquake presented usual problems associated with large coastal earthquakes in Mexico. It was difficult to pick *S* wave corresponding to the first *P* wave on local recordings. The density of stations is

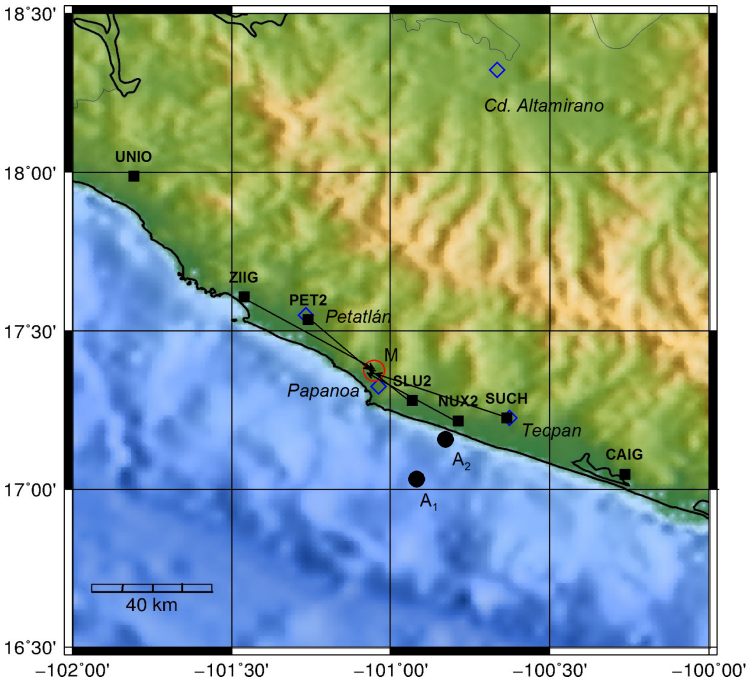


**Figure 2.** Permanent stations in the epicentral region. Azimuths of the hypocenter of the mainshock with respect to stations ZIIG, PET2, SLU2, SUCH, and NUX2, determined from P-wave polarization, are shown. The location of the mainshock and the aftershocks 8 May (Mw6.5) and 10 May (Mw6.1) are shown by circles and are marked M, A1, and A2, respectively.

still relatively sparse and crustal structure too poorly known for precise location of the event with only the arrival times of *P*-wave. *P*-waves of this earthquake on local seismograms were emergent. Thus, to locate the earthquake we used both *P*-wave arrival time and azimuth of the source at stations ZIIG, PET2, SLU2, NUX2, and SUCH (Figure 2). We measured the azimuth by plotting the horizontal displacement polarization during the first 3 s of *P* wave (Figure 3). The convergence of the azimuths points to a source near the town of Papanoa (Figure2). We fixed the depth at 15 km and searched for a location in the neighborhood of the convergence area which, using the crustal model employed by SSN, gave the minimum *P*-wave arrival-time *rms* error. This location is given in Table 1 along with those reported by other agencies. We note that the GCMT epicenter is 28 km to N47ºW of the epicenter obtained from local data (Figure 2).

*Some observations from local recordings*

Figure 4 shows plots of acceleration, velocity, and displacement traces at local stations from NW of the epicenter (UNIO, ZIIG, PET2) to the SE (SLU2, NUX2, SUCH, CAIG). The velocity and displacement traces were obtained from direct integration of the accelerograms. The traces begin at the arrival of *P* wave. As expected, the static displacements at most stations are unreliable. This is illustrated in Figure 5 where the displacements at ZIIG from double integration of acceleration traces and 1-s GPS data are compared (GPS station ZIHU is collocated with the seismographic station ZIIG). The figure demonstrates the need for collocation of accelerograph and GPS receiver if we wish to retrieve true ground displacement valid from infinite period to high frequencies. The static displacement at Tecpan GPS site was negligible as was also the case at CAIG.

Figure 4 includes plots of $I_i(t) = \int a_i^2(t)dt$, where the integration is performed beginning at the arrival of $P$ wave up to the end of the accelerogram, and $i$ refers to the component of the accelerogram. The plots list the "effective" duration of each component, defined here as the time window that includes 5 to 95% of $I_i(t)$.

Some source characteristics can be inferred from the visual inspection and preliminary analysis of local recordings:

1. The effective durations on the horizontal components at UNIO, ZIIG, and PET2 (to the NW of epicenter) range between 10 to 15 s while it is between 20 to 35 s at SLU2, NUX2, SUCH, and CAIG (stations to the SE of the epicenter). This suggests that the rupture propagated towards NW. Negligible static displacement field at Tecpan shows that the rupture did not extend till this town.

2. Three bursts of high-frequency radiation are visible in the acceleration traces at SLU2, NUX2, and SUCH. Two bursts are also seen at PET2. At ZIIG and UNIO the two bursts are not very clear.

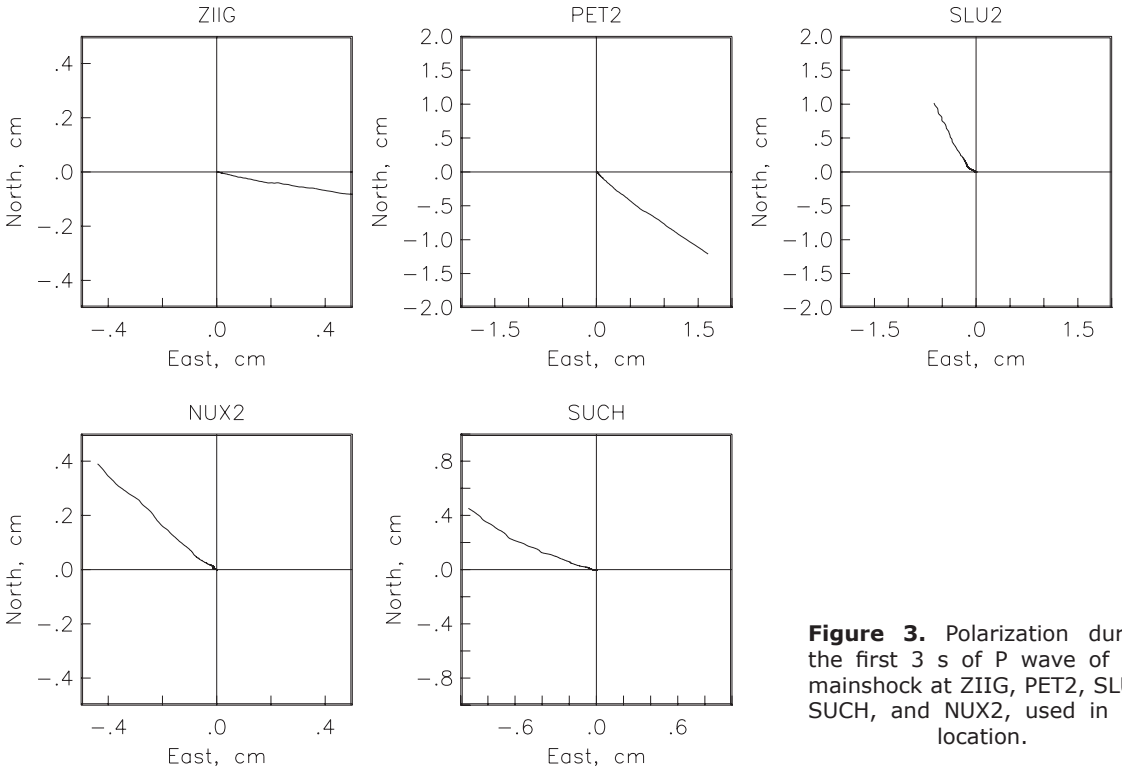


**Figure 3.** Polarization during the first 3 s of P wave of the mainshock at ZIIG, PET2, SLU2, SUCH, and NUX2, used in the location.

3. The displacement traces at SLU2, NUX2, and SUCH are dominated by a single, simple *S*-pulse. The displacements at these stations corresponding to the two later high-frequency bursts are relatively small. *S*-waves from the second and third bursts at these stations arrive ~ 7 s and 20 s after the *S* wave from the first burst. The displacement traces at PET2 and ZIIG consist of three, closely-spaced *S*-pulses. A simple working model, consistent with the observations, may consist of three sources, the first involving larger slip than the other two. The first source is located near the hypocenter ~ 20 km NW of SLU2,near the town of Papanoa (Figure 2). The second source is located roughly 10 km from the first source towards PET2. The third source is located between PET2 and ZIIG. Because of the proximity of the second and third sources, and larger slip during the first source, their corresponding *S* pulses are seen at PET2 and ZIIG. However, the latter two sources are relatively far from SLU2, NUX2, and SUCH. Hence, the first pulse dominates the record.

4. A subsidence of ~ 4 cm at ZIIG (Figure 5) suggests that if the rupture propagated up to this station then the slip on the fault probably did not extend more than about 8 km inland of this station. This conjecture is based on Okada's model (Okada, 1992; Figure 3 of Singh *et al*., 2012).

*Slip on the fault from inversion of teleseismic seismograms with some constrain from local GPS data*

Results from slip inversion, based on teleseismic data, were reported soon after the earthquake by NEIC and C. Mendoza (personal communication, 2014). NEIC inversion uses the NEIC hypocenter (17.6 °N, 100.7 °W, *H* = 24 km; Table 1). It shows two patches of slip: a compact, approximately circular area of ~10 km radius centered at the hypocenter and a diffused second patch with maximum slip occurring ~ 35 km to the WSW of the first patch. The moment rate function includes a third pulse which begins about 27 s after the first pulse and lasts for ~ 16 s. The slip distribution obtained by C. Mendoza, who uses 17.55 °N, 100.82 °W, *H* = 24 km as the hypocenter, is similar to that reported by NEIC. Since the locations used by NEIC and C. Mendoza are 45 km to N56ºE and 32 km to the N52ºE, respectively, with respect to the location estimated here, the slip areas obtained in these inversions are shifted inland accordingly.

In our inversion we applied the same simulated-annealing, wavelet domain waveform inversion algorithm as used by NEIC (Ji *et al.*, 2002a, b) to invert teleseismic body and surface waves for the slip on the fault plane. We used a total of 29 *P*-waves, 34 *S*-waves,

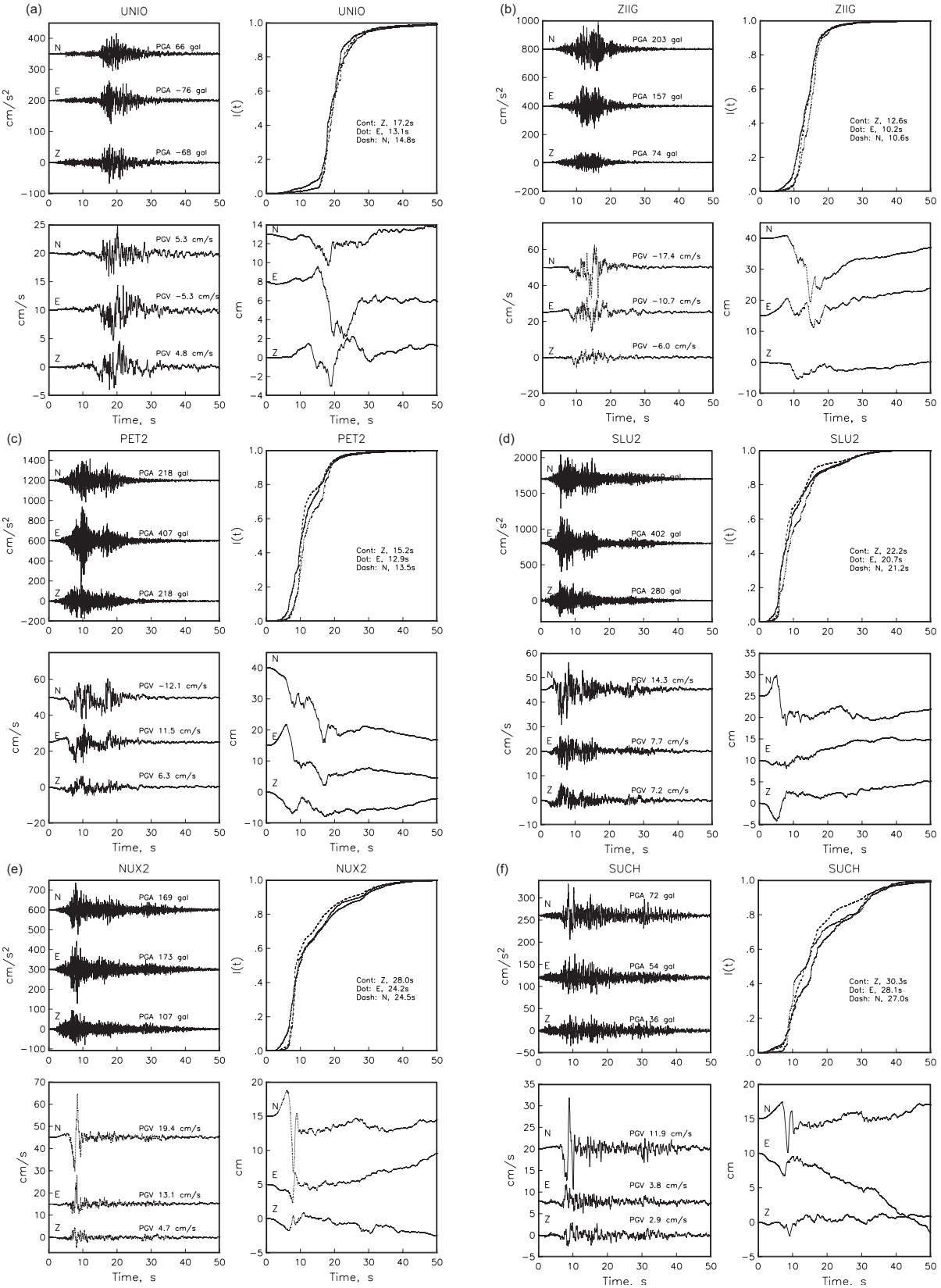


**Figure 4.** Acceleration, Arias intensity, velocity, and displacement at (a) UNIO, (b) ZIIG, (c) PET2, (d) SLU2, (e) NUX2, (f) SUCH, and (g) CAIG. Displacement was obtained from double integration of base-line corrected acceleration, without applying any filter.

29 Rayleigh waves and 29 Love waves. In addition, we included the static displacement measured by the GPS instruments of the SSN at ZIIG (Figure 5) and Tecpan (TCPN, which was taken as zero) in the inversion. We used the hypocenter location and origin time determined in this study (Table 1) as well as that reported initially by the SSN (Table 1). We inverted for the magnitude, direction and duration of slip at each 10 × 10 km$^2$ subpatch of the fault. The slip-rate function of each fault was parameterized by an asymmetric cosine function (Ji *et al.*, 2002a). The timing of the initial slip in each patch was constrained to follow a rupture velocity of 2-3 km/s. First the body-wave arrivals were aligned on theoretical travel times based on a 1D Earth model. However, we found large apparent time shifts between observed and calculated seismograms, caused by the 3D structure of the Earth. The systematic variation of these shifts with azimuth is probably also responsible for the large mislocation of the hypocenter by global agencies, mentioned above. To minimize the effect of unmodeled 3D structure on the result, we manually aligned the body-wave phases on the first observable arrival in the seismogram. At stations where we could not identify the first arrival, we aligned them to be consistent with neighboring stations. The distribution of slip on the fault plane determined by the inversion, projected to the surface of the earth, is shown in Figure 6a and b. The figure also shows computed and observed static field at Zihuatanejo (ZIIG) and Tecpan (TECP). Observed and synthetic seismograms are compared in Figure 6c. The observations are well fit by the synthetics. The total seismic moment obtained from the modeling is 8.32×10$^{19}$ Nm ($M_w$7.2).

There are two significant regions of slip, one near the hypocenter and the other ~ 40 km to WSW (Figure 6a). The first slip area is similar to that reported by NEIC and C. Mendoza but the second one is more concentrated than in the other two studies. The location of this area suggests that it probably corresponds to the third burst of high-frequency energy, seen in the accelerograms at SLU2, NUX2 and SUCH. The region of the second emission of high-frequency energy is not resolved in the inversion.

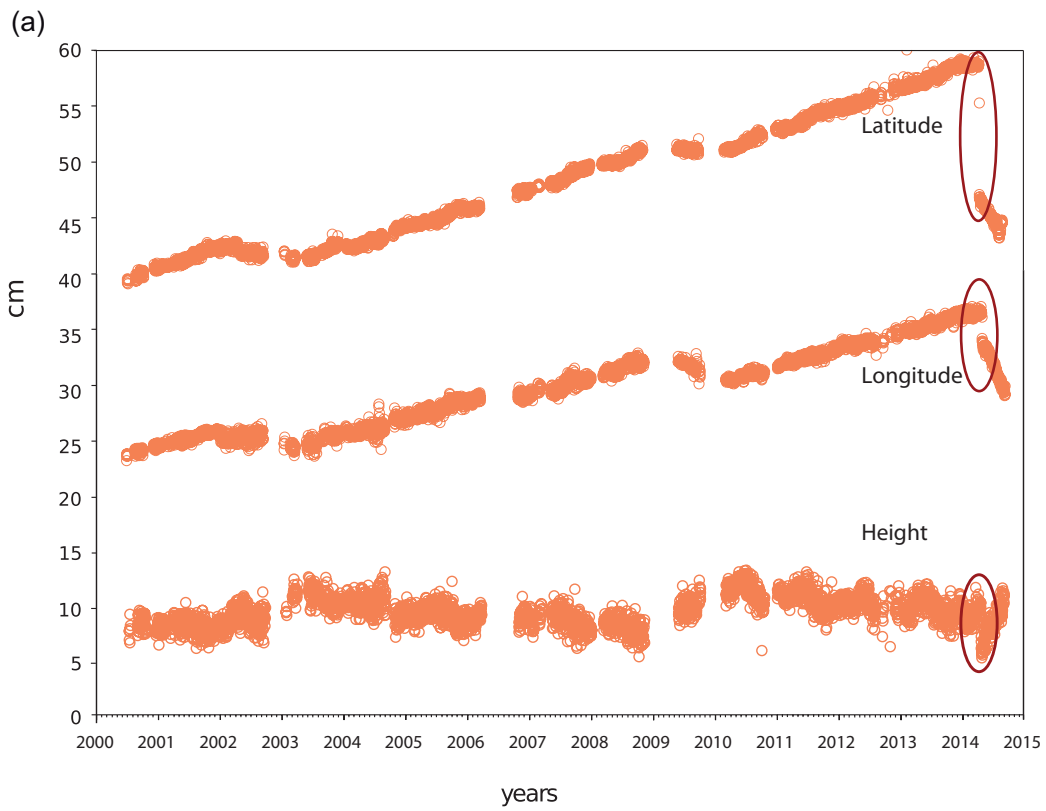


**Figure 5.** (a) GPS time series at ZIHU for the period 2000 – August 2014 (sampling 0.03 Hz). The ellipses enclose co-seismic displacement for the 18 April 2014 earthquake. Post-seismic displacement associated with the event is clearly visible.

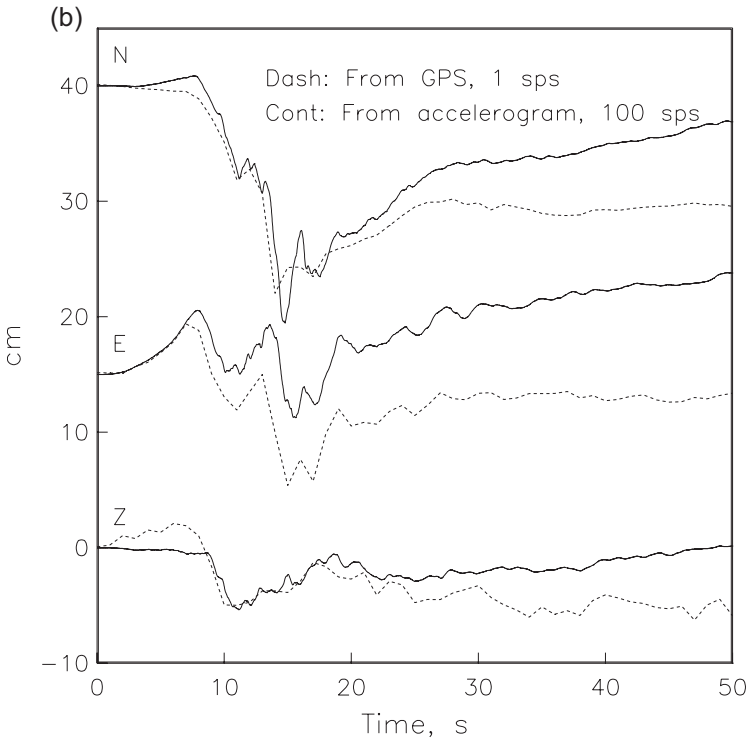


**Figure 5.** (b) Coseismic displacement at ZIIG from double integration of acceleration traces (sampling 100 Hz) and at ZIHU from 1-sec GPS data (ZIIG and ZIHU are collocated).

A comparison between the slip models obtained using the hypocenter determined in this study (Figure 6a) *versus* that reported initially by SSN (Figure 6b), shows that the relative location of the slip patches to the hypocenter and each other remains similar. However, the absolute location varies significantly. This shows how critical an accurate hypocenter location is.

*Aftershocks of the 18 April 2014 earthquake*

Following the earthquake, the Institutes of Geophysics and Engineering of UNAM installed a portable network of three broadband seismographs and two accelerographs in the epicentral zone. This network became operational within about 24 hours. Analysis of the data from this network is in progress. In this report we present location of the aftershocks based only on the permanent seismic network. We located 108 aftershocks ($2.4 \leq M \leq 5.2$), which occurred within 36 hours of the mainshock. In locating the earthquake we also used the azimuth of the source obtained from *P*-wave polarization. Keeping the depth free or fixing it at 15 km only slightly changed the epicentral locations. The aftershocks (from our preferred depth-free locations) define an area of ~ 40 km × 70 km, with major length oriented N75ºE, situated between Papanoa and Zihuatanejo (Figure 6). This area encloses the inverted slip region. However, there were few aftershocks in the area of large slip corresponding to the first subevent. Aftershocks suggest that the rupture reached inland and extended ~ 30 km updip from the hypocenter. About 50 % of the aftershock area lies onshore. Generally, the aftershock and slip distributions are consistent with each other. A large fraction of the 2014 aftershock area overlaps with that of the 1979 earthquake (Figure 6a). A small part also falls in the aftershock area of the 21 September 1985 earthquake.

The slip contours during SSEs of 2001-2002, 2006, and 2009-2010 (adopted from Radiguet *et al*., 2012) are shown in Figures 7a, 7b, and 7c along with the aftershock areas of large earthquakes in the region. The figure shows that the area of large slip during first subevent of the 2014 earthquake (located inland, Figure 6a) had previously slipped 6 - 10 cm, ~ 2 cm, and 6 – 10 cm during these previous SSE episodes.

The two largest aftershocks occurred on 8 May ($M_w$6.5) and 10 May ($M_w$6.1). During 8 May earthquake a bridge in Tecpan collapsed. The earthquake was strongly felt in Mexico City. The source parameters of these events are listed in Table 2. A careful analysis of spectral ratios of the recordings of these aftershocks shows

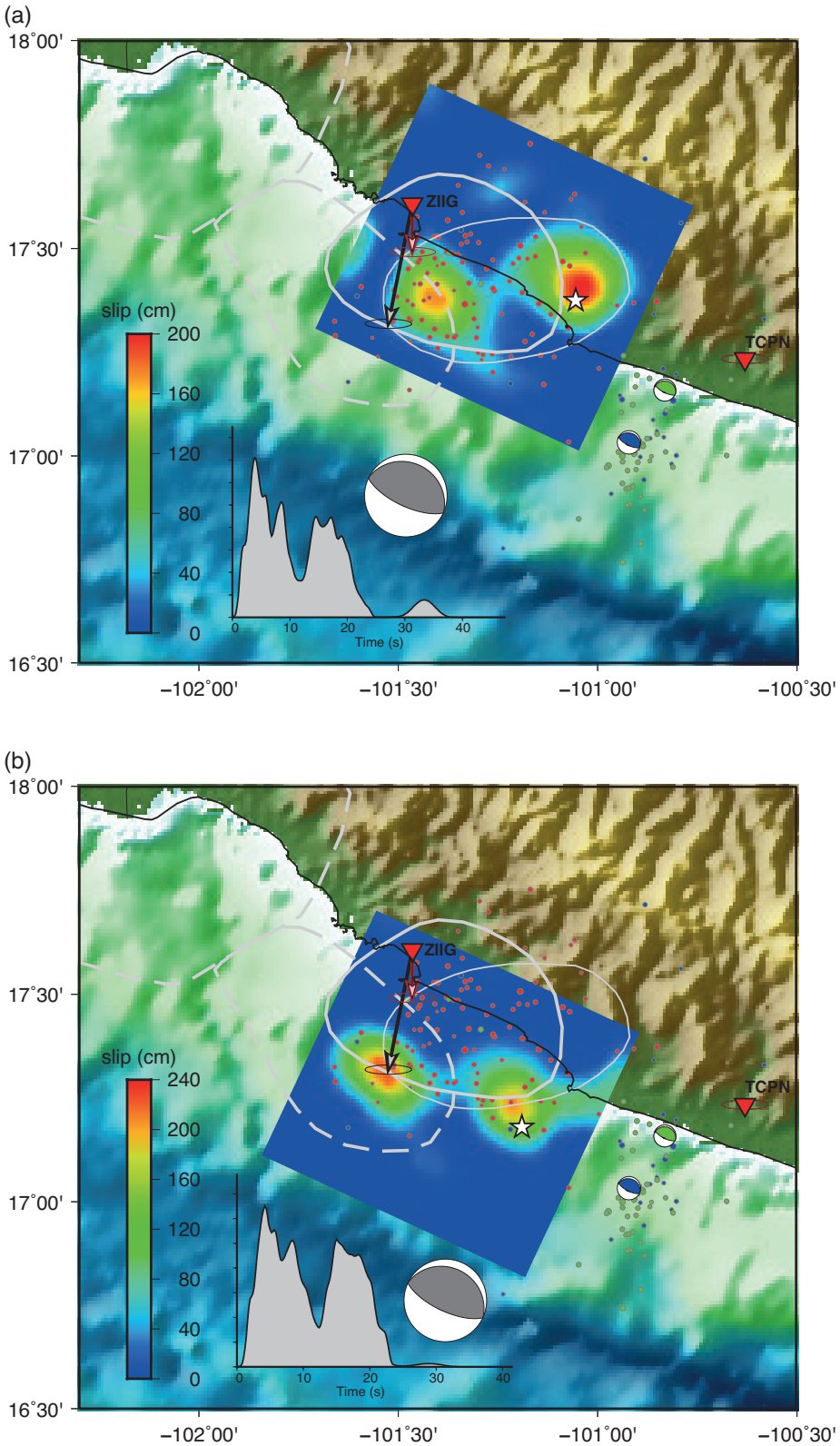


**Figure 6.** (a) Slip of the fault from inversion of teleseismic body and surface waves, and static field at ZIIG and Tecpan using hypocentral location from this study (Table 1). Circles: aftershocks (see text). Source time function for the solution is shown. (b) Same as (a) but using hypocentral location initially reported by SSN.

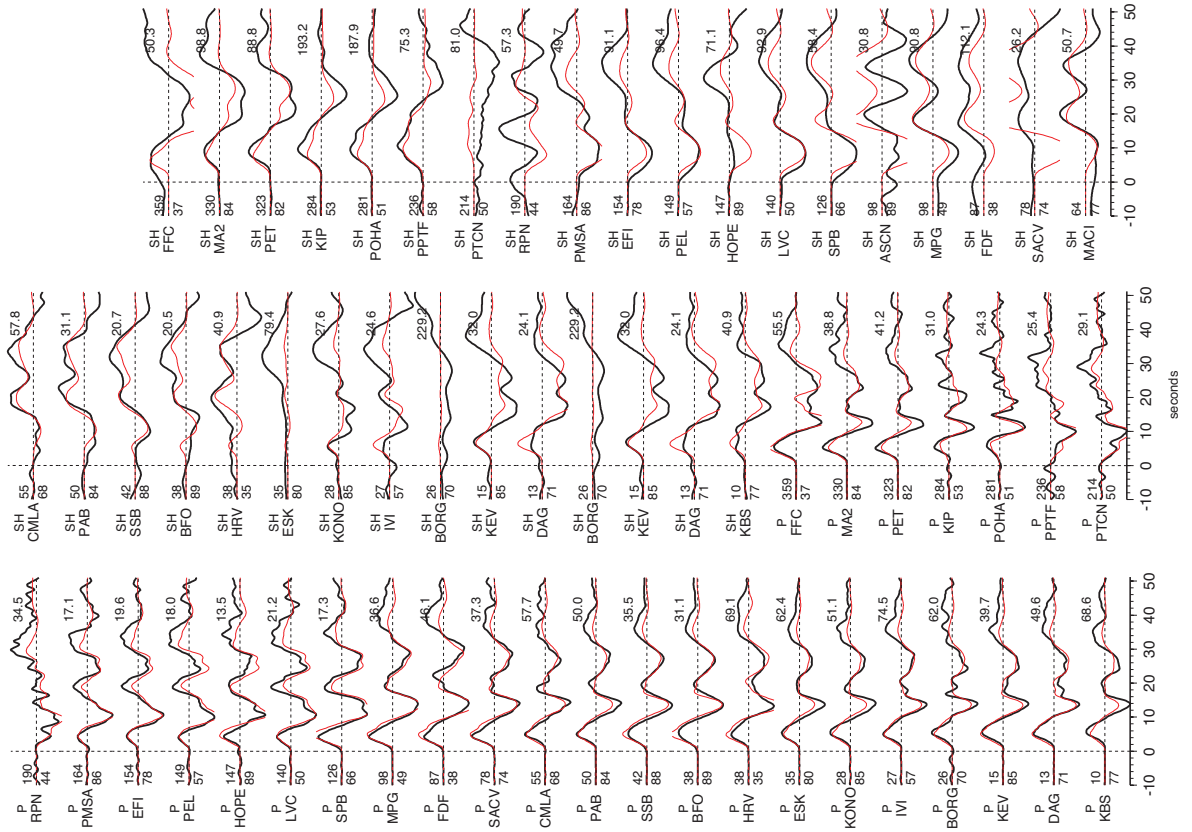


**Figure 6.** (c) Comparison of observed and synthetic teleseismic seismograms corresponding to the inversion using hypocentral location from this study.

that the rupture during the 8 May earthquake propagated SE, towards Acapulco, whereas the opposite occurred during the 10 May event. For the sake of brevity, we abstain from presenting a detailed analysis here. These aftershocks generated their own aftershock sequences. As seen in Figure 6, the location of these events and their aftershocks are separated from the aftershock and slip areas of the mainshock. Clearly these two large aftershocks occurred in the NW Guerrero seismic gap.

## SSE of 2014 and the Papanoa earthquake

As mentioned earlier, a slow slip event was in progress in Guerrero at the time of the Papanoa earthquake. Location of some selected GPS stations and the corresponding GPS time series

**Table 2.** Source parameters of the aftershocks of 8 May 2014 (Mw6.5) and 10 May 2014 (Mw6.1)

| Date; Hr:Min:Sec | Lat., °N | Lon., °W | Depth, km | $M_0$, Nm | $M_w$ | Strike, o | Dip, o | Rake, o | Source |
|---|---|---|---|---|---|---|---|---|---|
| 08/05/14; 17:00:16.0 | 17.033 | 100.922 | 18F | $9.64\times10^{18+}$ | $6.6^{+}$ | $297^{+}$ | $11^{+}$ | $89^{+}$ | This study |
| 08/05/14; 17:00:22.1 | 17.300 | 100.690 | 23.2 | $6.67\times10^{18}$ | 6.5 | 289 | 21 | 83 | Global CMT |
| 10/05/14; 07:36:01.4 | 17.159 | 100.831 | 24.0 | $2.19\times10^{18+}$ | $6.2^{+}$ | $296^{+}$ | $10^{+}$ | $94^{+}$ | This study |
| 10/05/14; 07:36:06.8 | 17.300 | 100.730 | 20.9 | $1.86\times10^{18}$ | 6.1 | 283 | 19 | 76 | Global CMT |

are shown in Figures 8a and 8b, respectively. Clearly, slip during the 2014 SSE extended to the north at least until IGUA (Iguala) and to the south upto the coastal stations of CAYA, COYU, ACYA, and TCPN. A visual examination of the traces in Figure 8b suggests that the SSE may have started near ACYA. As expected, large coseismic displacement caused by the 2014 Papanoa earthquake is observed at station ZIHP (see, also, Figure 5) and PAPA which lie above the rupture area. It is also visible at sites outside the epicentral zone, e.g., at TCPN, CAYA, and IGUA. Curiously, ZIHP shows small, if any, displacement during the SSE prior to the earthquake. This may also be true for PAPA, although the data was lost during the critical time period. It seems very likely that the region of seismic slip during the mainshock did not experience slow slip during the 2014 SSE prior to the rupture. Whether 2014 earthquake was triggered by the 2014 SSE must await mapping of the slip evolution in time and space which is currently in progress.

## Radiated seismic energy and source spectrum

Seismic energy, $E_s$, for the mainshock was estimated from teleseismic ($8.5 \times 10^{14}$ J, $M_e$ = 7.03) and regional data ($3.1 \times 10^{15}$ J, with corresponding energy magnitude $M_e$ = 7.43) independently. For the first, we follow Boatwright and Choy's (1986) methodology as modified by Pérez-Campos and Beroza (2001) and Pérez-Campos *et al*. (2003).This includes a stronger attenuation correction for subduction earthquakes and a generic site correction for hard rock sites (Boore and Joyner, 1997). For the regional estimation, we followed Singh and Ordaz (1994), and included a site correction suggested by Pérez-Campos *et al*. (2003). Difference between these two estimates, a factor of 3.6, is reflected in the source spectra obtained from each set of data (Figure 9b). The teleseismic spectrum is depleted at high frequencies with respect to the regional spectrum. One possible explanation is that some energy is being trapped in the hanging wall (Brune, 1996), resulting in larger values of $E_s$ for the regional estimates and lower values of $E_s$ for stations in an azimuthal range of 0-150º than for stations within a range of 260-360º (Figure 9a). If we use regional stations within 260-360º of azimuth, we obtained an average $E_s = 1.08 \times 10^{15}$ J ($M_e$ = 7.12), only a factor of 1.3 from the teleseismic estimate. Another possible explanation is directivity. Although understanding the cause of the discrepancy between teleseismic and regional estimates of $E_s$ has important implication in ground motion prediction, it is beyond the scope of this paper.

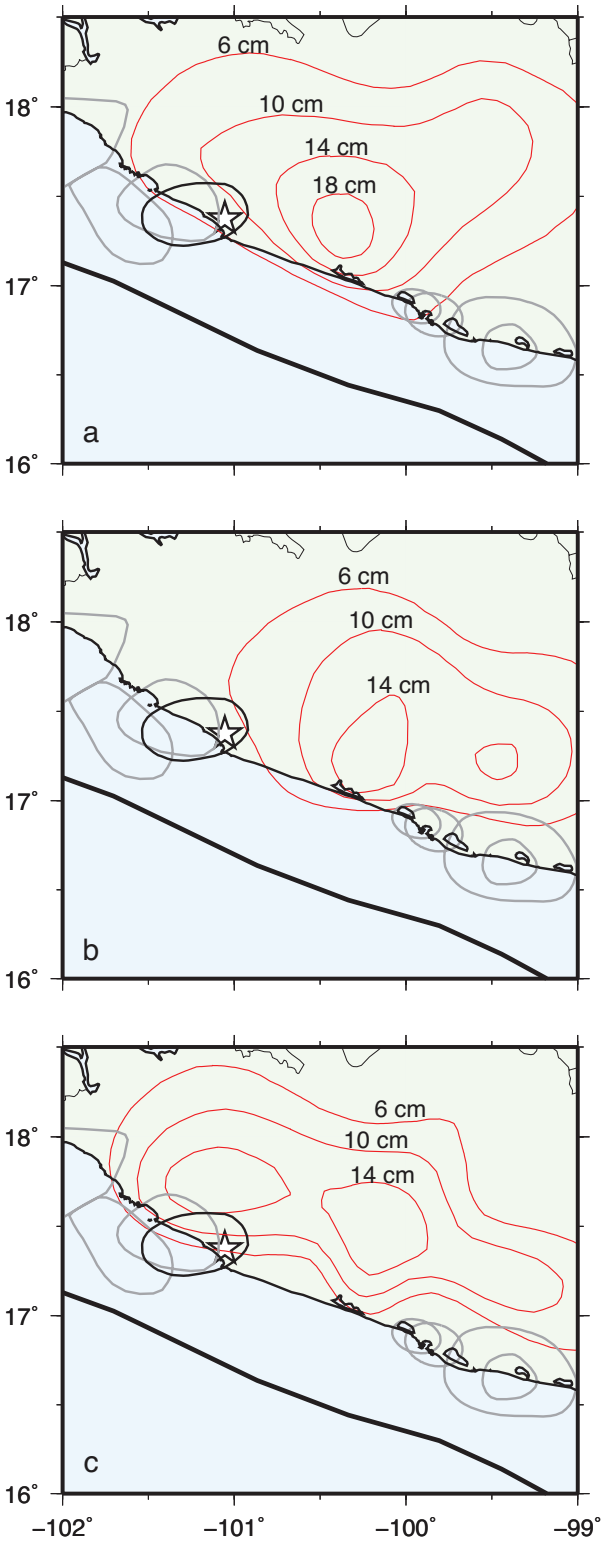


**Figure 7.** Slip contours (thin lines) during seismic slip events of (a) 2001-2002, (b) 2006, and (c) 2009-2010 adopted from Radiguet *et al*. (2012) for geometry B of the plate interface. The aftershock areas of large earthquakes in the region are shown by thick contours. Star denotes the epicenter of the 2014 earthquake.

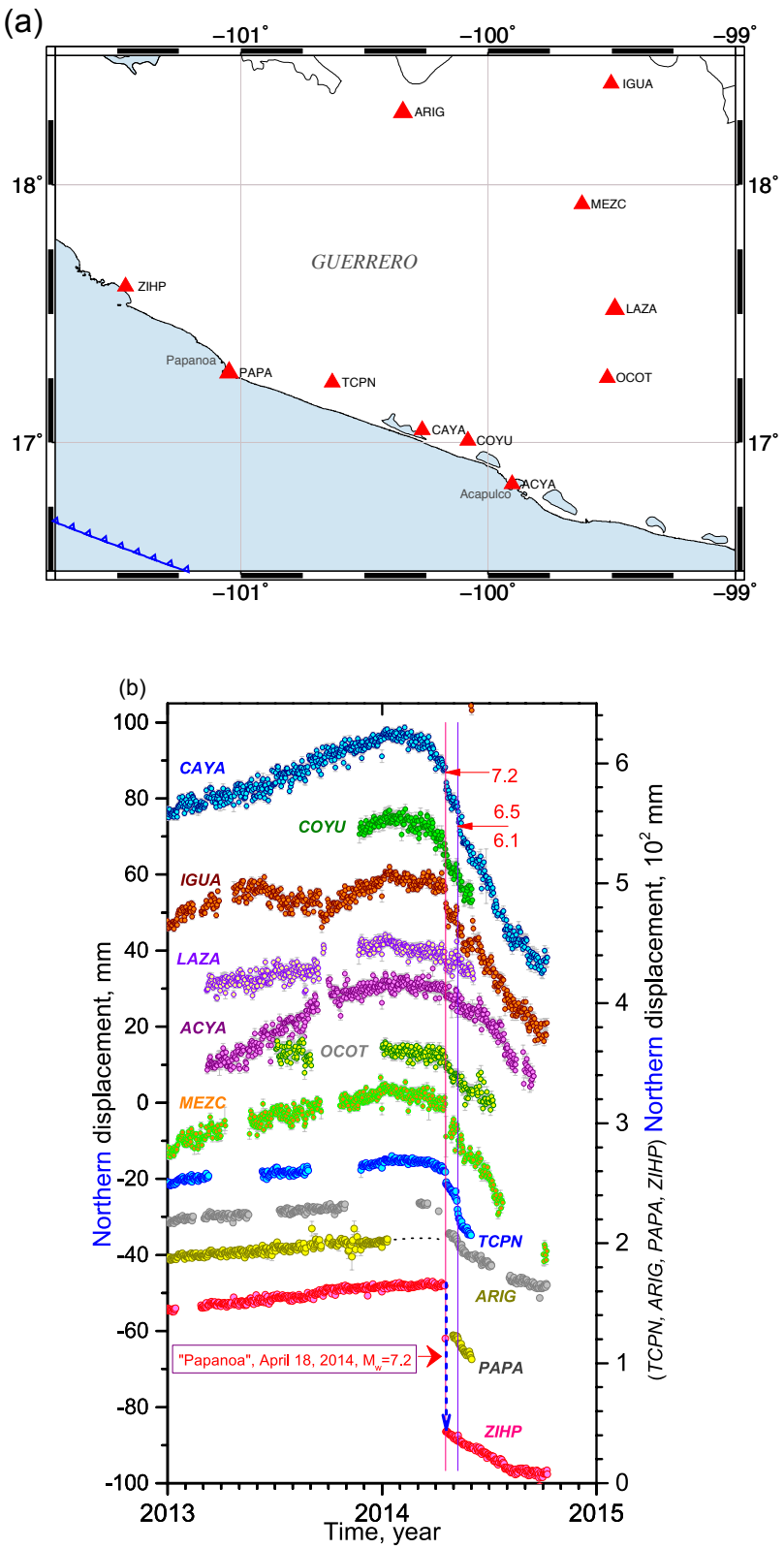


**Figure 8.** (a) Map showing location of some GPS sites in Guerrero. (b) Northern displacement beginning 2013 at sites shown in (a). Vertical lines indicate origin times of 18 April 2014 Papanoa earthquake and its largest aftershock of 8 May. Beginning of SSE in January of 2014 is visible at most stations, except at ZIHP and perhaps also at PAPA.

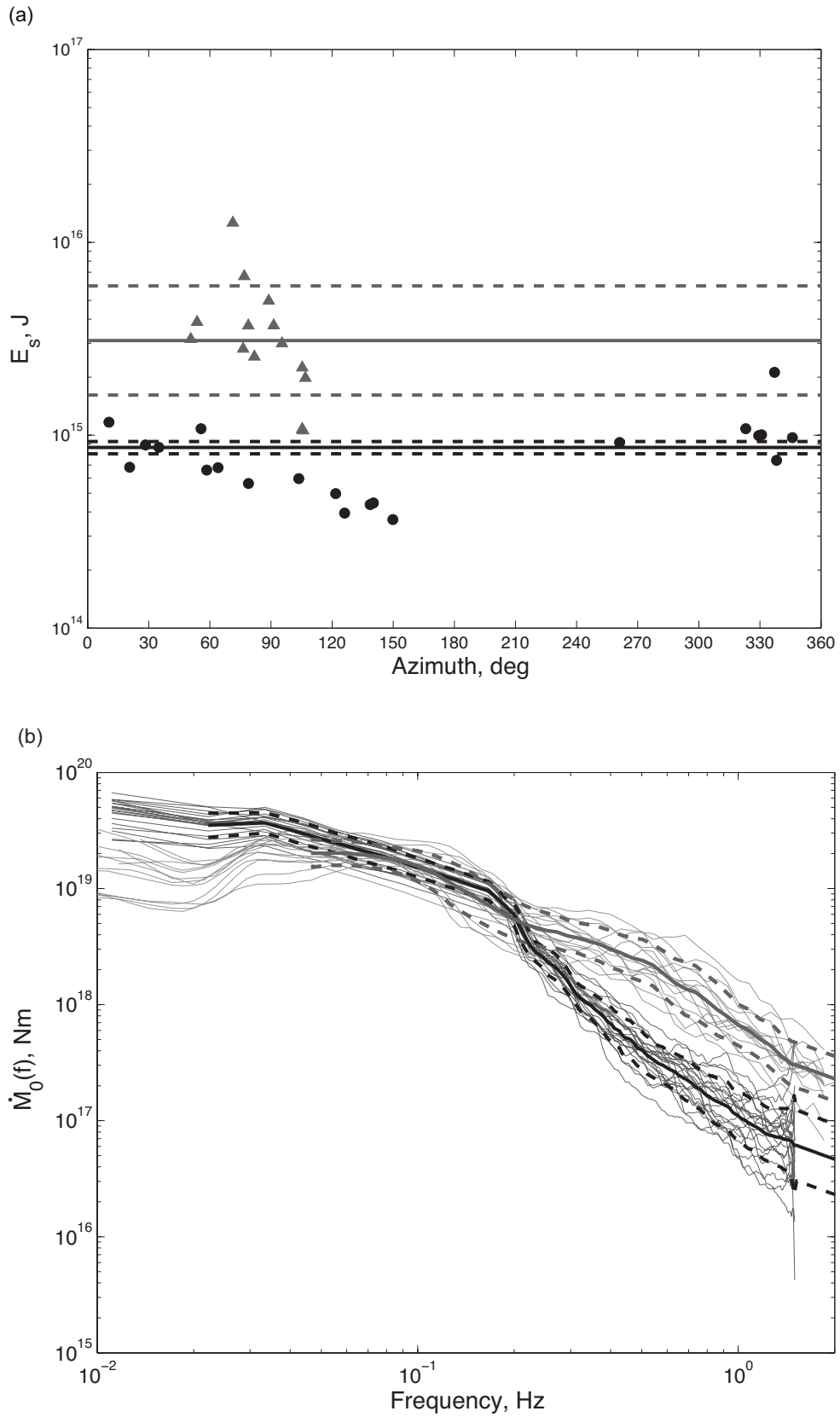


**Figure 9.** (a) Seismic energy, $E_s$, estimated with teleseismic data (black dots) and regional data (triangles). (b) Source spectra from teleseismic data (black lines) and regional data (gray lines).

**Strong ground motions in Mexico City**

The earthquake was strongly felt in Mexico City and caused general panic. The damage, however, was minor. Several walls collapsed and cracks were reported in some facades. The city suffered partial power outage. It is interesting to compare ground motions in Mexico City during this earthquake with those recorded during other recent large earthquakes. We illustrate this comparison at CU and SCT, representative sites of hill- and lake-bed zones, respectively.

Accelerograms of Mexican earthquakes recorded on CU campus of UNAM are available since 1964. *PGA* ($\mathrm{PGA} = [(A_n^2 + A_e^2)/2]^{1/2}$), where $A_n$ and $A_e$ are peak accelerations on NS and EW components, respectively) during the Papanoa earthquake was 13.7 gal, the fourth largest produced by interplate subduction earthquakes since 1964. The other three earthquakes were: 19 September 1985 Michoacán, $M_w$8.0 (30 gal); 14 March 1979 Petatlán, $M_w$7.4 (18.3 gal); and 21 September 1985 Michoacán-Guerrero, $M_w$7.5 (13.9 gal). Figure 10a shows the median Fourier spectra of the two horizontal components. The spectral amplitudes of all four events are about the same above 2 Hz. However, the 19 September 1985 earthquake has significantly higher spectral level below 2 Hz, followed by the 1979 earthquake. The spectra of the earthquakes of 21 Sep. 1985 and 2014 are similar above 0.4 Hz and the *PGA* values are almost same.

SCT station, located in the lake-bed zone, did not exist in 1979 and the accelerograph malfunctioned during the 21 Sep. 1985 earthquake. Figure 10b shows median Fourier spectra of four interplate earthquakes with largest recorded *PGA* at SCT. These events are: 19 Sep. 1985 Michoacán, $M_w$8.0 (132.1 gal); 25 Apr. 1989 San Marcos, $M_w$6.9 (38.8 gal); 18 Apr. 2014, $M_w$7.3 (31.3 gal); and 14 Sep. 1995, Copala, $M_w$7.3 (29.5 gal). The spectral level of the 19 Sep. 1985 is higher than for the other events. 1989 earthquake has slightly higher spectral level between 0.2 and 0.6 Hz than the other two events, which have very similar spectra as well as *PGA* values.

We recall that during the 1979 earthquake a building of Iberoamericana University in the lake-bed zone collapsed. *PGA* during this earthquake at CU was 18 gal. The earthquake of 1989 caused some damage to the city. During the 1989 earthquake the *PGA* values were 12 and 39 gals at CU and SCT, respectively. This suggests that some damage to Mexico City from an interplate earthquake may be expected if *PGA* values at CU and/or SCT exceed ~ 15 and

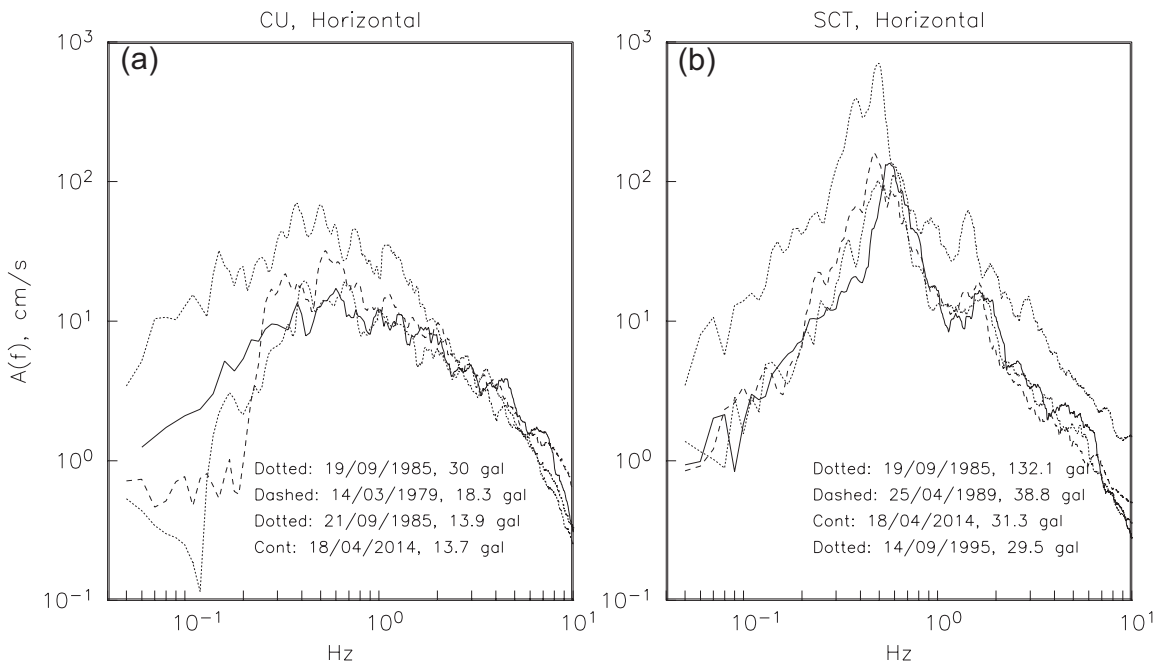


**Figure 10.** (a) Fourier acceleration spectra (median of the two horizontal components) at CU, a hill-zone site, during four interplate earthquakes with largest PGA values recorded at the station since 1964. PGA values are given in the figure. (b) Same as (a) but at SCT, a lake-bed zone site.

40 gal, respectively. It is worth remembering that these values at CU and SCT during the disastrous 19 September 1985 earthquakes were 30 and 132 gals, respectively.

## Damage and Iso-Acceleration Contours

The earthquake caused significant damage to Papanoa and other coastal towns in the epicentral zone. The highest *PGA* (geometric mean of the two horizontal components) of 1138 gal was recorded at a soft site in Papanoa. At hard sites the recorded *PGA*s were ≤ 420 gal (Figure 4). Figure 11 shows PGA contours of the earthquake. These contours were obtained from the recorded data using a Bayesian interpolation technique. We note that the maximum contour roughly coincides with the maximum slip (Figure 6a). The figure also shows municipalities where significant structural damage occurred and which received federal funds for recovery and reconstruction of the affected population.

## Attenuation of strong motion with distance

Figure 12 shows plot of ground motion parameters - *PGA* and pseudo-acceleration response spectra (5 % damping), *Sa*, at $f$ = 5, 1, and 0.5 Hz - as a function of $R$, the closest distance from the rupture area. With few exceptions (marked in the figure), the stations are situated at hardrock sites. The expected motions from ground-motion prediction equations (GMPEs) developed by Arroyo *et al*. (2010), shown by dashed curves (median and ± 2$\sigma$), match well with the observations, giving us confidence in the applicability of these relations.

## Discussion and conclusions

The earthquake of 2014 ruptured a segment of the plate boundary between Papanoa and Zihuatanejo, leaving intact the NW Guerrero seismic gap, which extends from Acapulco to Papanoa (~100 ºW– 101 ºW). More than half of the aftershock area of the earthquake overlaps with that of the 1979 earthquake and a small fraction of it with that of the 21 September 1985 earthquake. The aftershock area of the 1985 earthquake is somewhat uncertain as it generated relatively few aftershocks and also because of the contamination from the aftershocks of the great Michoacán earthquake ($M_w$ 8.0) which had occurred ~36 hours earlier (UNAM Seismology Group, 1986). Due to a dense deployment of portable seismographs in the epicentral zone, the 1979 aftershock area is well defined (e.g., Valdés-González *et al*., 1998). Unfortunately, the slip distribution during these previous earthquakes is not

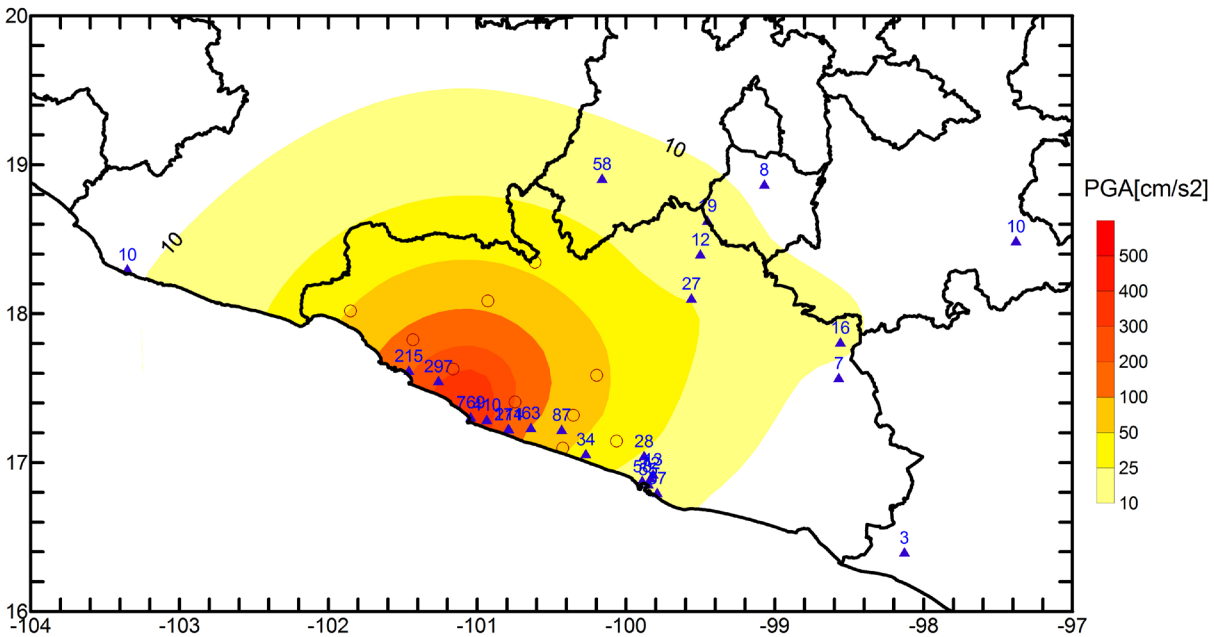


**Figure 11.** PGA iso-contour for rock sites during the Papanoa earthquake. Triangles: recording stations. Circles: municipalities where considerable structural damage was observed.

known. For this reason, a critical issue that cannot be resolved is whether one or both patches that slipped during the 2014 event also broke during 1979 and/or 1985, or whether the major slip during 2014 occurred over areas that had not slipped during the previous two earthquakes. In view of the aftershock areas of the three earthquakes, the width of the seismogenic zone in the region may be ~ 70 km, extending ~ 25 km inland.

The adjacent segment, the NW Guerrero gap, has not experienced a large/great earthquake since 1911. Episodic slow slip earthquakes (SSEs) reported in the region occur not only on the subhorizontal part of the plate interface but appear to extend updip up to about 10 km inland from the coast. Large slip during the first subevent of the Papanoa earthquake occurred on a patch of the plate interface which had slipped 6 – 10 cm, ~ 2 cm, and 6 – 10 cm during previous SSE episodes of 2001-2002,

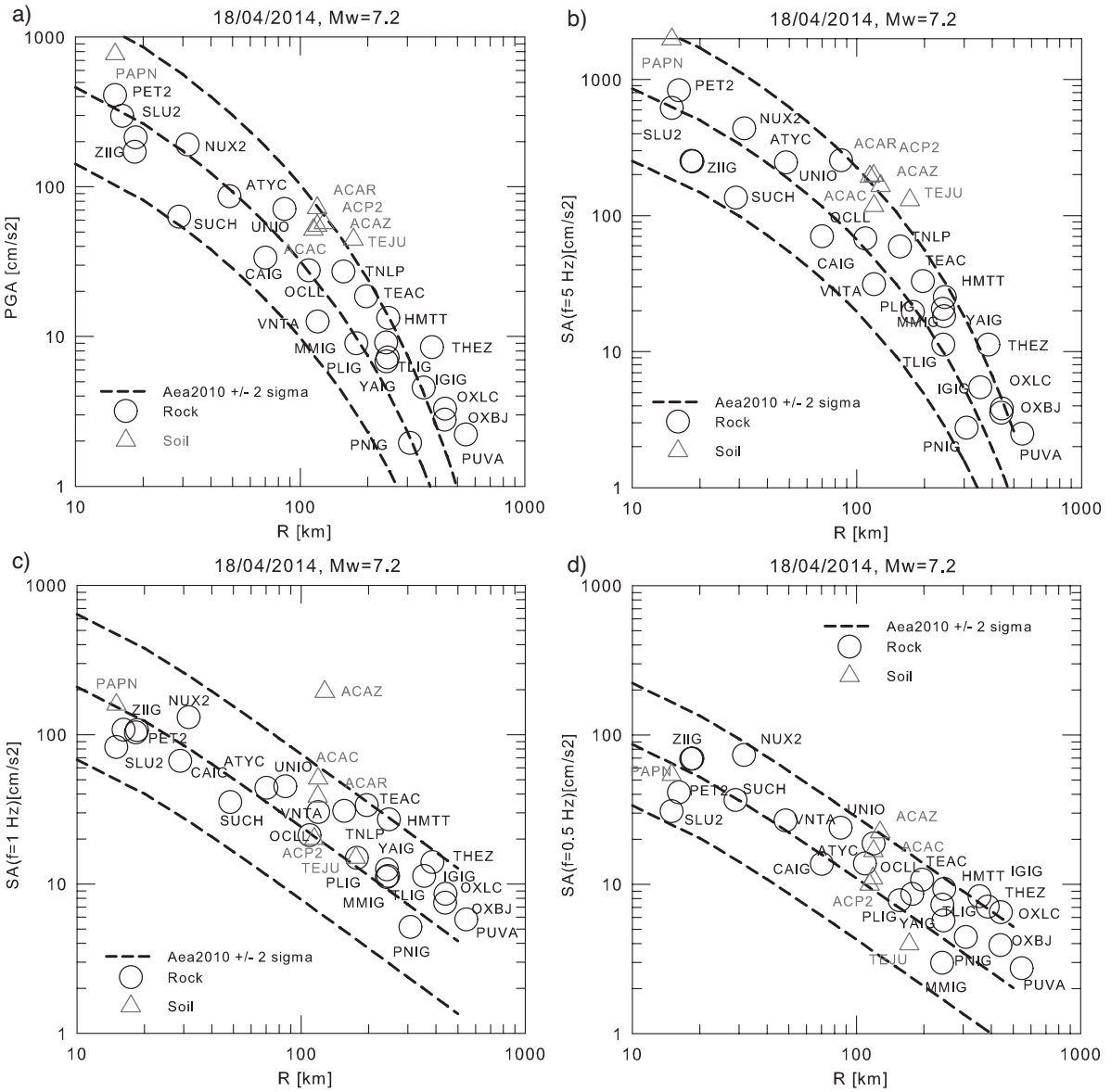


**Figure 12.** PGA and pseudo-acceleration response spectra (5% damping), Sa, at f = 5, 1, and 0.5 Hz, as a function of R (closest distance to rupture area), observed during the Papanoa earthquake. PGA and Sa values correspond to the geometrical mean of the two horizontal components. Predictions from Arroyo *et al.* (2010) (denoted as Aea2010) shown by dashed curves (median and ± 2σ) match well with the observations. Note that only the intra-event part of sigma is considered.

2006, and 2009-2010, respectively (Radiguet *et al*., 2012) (Figure 7). The inverted slips on/near the patch during the SSEs are mostly controlled by the GPS station at Zihuatanejo (ZIHU) and are probably not well resolved. If, however, the slip on the patch during the SSEs is real, then it implies that slow and fast slip can occur over the same area of the interface during SSEs and earthquakes, respectively.

Mechanical models of earthquakes under rate- and state-dependent (R&S) laws show that rapid (unstable) and aseismic slip is primarily governed by velocity-weakening (VW) and velocity-strengthening (VS) fault constitutive regimes, respectively (e.g., Lapusta *et al*., 2000; Liu and Rice, 2007; Kaneko *et al*., 2010). Since the aseismic slip apparently spread over the first asperity of the Papanoa earthquake during earlier SSE episodes, it suggests that this segment is mainly characterized by VS properties. However, while unstable rupture propagation (with rapid slip) may occur over VS segments due to dynamically driven weakening processes (Noda and Lapusta, 2013), it cannot spontaneously initiate in those segments. To reconcile the observations with a physical model, we propose that the area which ruptured during the first subevent was a VW patch (an asperity) surrounded by a conditionally stable and larger VS zone where slow slip during the SSEs occurs. This R&S mechanism has successfully explained the mechanism of repeating earthquakes (Chen and Lapusta, 2009), where slow slip in VW patches arises as a consequence of aseismic movement in the surrounding VS fault.

We note that the aftershock areas (presumably also the slip areas) of 1979 and 2014 earthquakes begin about ~ 35 km downdip from the trench (Figure 6a). Seismically, the interface from the trench up to a distance of ~35 km downdip appears similar to that of the adjacent NW Guerrero gap (Figure 1b). In both regions there is little seismicity at $M$ > 5 level in this portion of the interface, except for a sequence of near-trench earthquakes which were recorded on 18 April 2002. The mainshock ($M_w$6.7), which was located near the trench of the NW Guerrero gap, produced many aftershocks. The principal aftershock ($M_w$5.9) was also located near the trench but updip of the 1979 and 2014 aftershock areas. The two events are denoted NTE in Figure 1b. These moderate earthquakes were deficient in high-frequency radiation of seismic energy (Iglesias *et al*., 2003). The mainshock had extraordinarily large centroid delay time for its magnitude, about 30 s (Figure 4 of Duputel *et al*., 2013). It also generated a small tsunami. These characteristics point to a tsunami earthquake. [The only other region along the Mexican subduction zone where similar near-trench earthquakes have been documented is off the coast of Pinotepa Nacional (Iglesias *et al*., 2003).] Thus, the shallow interface near the trench updip of the aftershock areas of 1979 and 2014 earthquakes as well as the NW Guerrero seismic gap seems to be in the domain of tsunami earthquakes or of stable sliding. The interface further downdip upto ~ 35 km from the trench may be aseismically stable, or conditionally stable so that it slips seismically when accelerated and dynamically weakened by rupture of adjacent seismic patches (Noda and Lapusta, 2013).The interface from 35 to 80 km of the trench in Papanoa – Zihuatanejo region clearly differs from the region of NW Guerrero. In the former region, although aseismic (slow) slip seems to reach the coast (~65 km from the trench), this seismically active portion of the interface clearly has highly locked VW asperities, so that the inter-SSE coupling ratio is relatively high (>0.5). In the latter region (i.e., within the seismic gap), the strain is mostly released during SSEs, the inter-SSE coupling ratio is very small (< 0.2), and slip deficit is one-fourth of that in the former region (Radiguet *et al*., 2012). However, as suggested by the two largest aftershocks ($M_w$6.5 and $M_w$6.1) that occurred in the NW segment of the gap about 20 km away from the mainshock (Figure 6a), this portion of the interface may be conditionally stable with isolated unstable asperities, such as the ones depicted by the green and blue epicenters. Actually, the absence of aftershocks between this area and the main rupture zone may probably reflect aseismic afterslip accommodation on the plate interface that eventually triggered the $M_w$6.5 and $M_w$6.1 sequence.

The earthquake caused significant damage to Papanoa and other coastal towns. The peak iso-acceleration contour coincides with area of large-slip. The earthquake was strongly felt in Mexico City but caused only minor damage. The recorded ground motions in the city were similar to those produced by the 1979 and 1985 earthquakes. It is reassuring to note that the ground motion prediction equations developed for Mexico explain the observed ground motion parameters quite well.

## Acknowledgements

UNAM Seismology Group includes all researchers and technicians of Institute of Geophysics and Institute of Engineering, UNAM who work in the field of seismology and engineering seismology. In case of a significant

earthquake in Mexico, the Group informally coordinates its efforts in data collection from autonomous stations, field deployment of seismographs and accelerographs, analysis of the data, and elaboration of a preliminary report. The credit of the work is shared by all.

We thank Civil Protection authorities of the State of Guerrero, Centro de Instrumentación y Registros Sísmicos (CIRES) and Centro Nacional de Prevención de Desastres (CENAPRED) for making available to us the recordings of the mainshock. The research was supported by PAPIIT-UNAM projects IB101812, IN111314, IN113814, IN110514, and Conacyt project 178058. We also thank Andrea Walpersdorf and Nathalie Cotte for the GPS displacement time series.

**References**

Abe K., 1981, Magnitude of large shallow earthquakes from 1904 to 1980. *Phys. Earth. Planet. Interiors,* 27, 72- 92.

Abe K., Noguchi S.I., 1983, Revision of magnitudes of large shallow earthquakes, 1897–1912. *Phys. Earth. Planet. Interiors* 33, 1, 1-11.

Anderson J.G., Bodin P., Brune J.N., Prince J., Singh S.K., Quaas R., Onate M., 1986, Strong Ground Motion from the Michoacan, Mexico, Earthquake. *Science* 233, 4768, 1043-1049. DOI:10.1126/science.233.4768.1043.

Anderson J.G., Singh S.K., Espindola J.M., Yamamoto J., 1989, Seismic strain release in the Mexican subduction thrust. *Phys. Earth. Planet. Interiors* 58, 4, 307-322.

Anderson J.G., Brune J.N., Prince J., Quaas R., Singh S.K., Almora D., Bodin P., Oñate M., Vásquez R., Velasco J.M., 1994, The Guerrero accelerograph network. *Geofísica Internacional* 33, 341-372.

Arroyo D., Garcia D., Ordaz M., Mora M.A., Singh S.K., 2010, Strong ground-motion relations for Mexican intreplate earthquakes. *J. Seismol.*, DOI 10.1007/s10950-010-9200-0.

Boatwright J., Choy G.L., 1986, Teleseismic estimates of the energy radiated by shallow earthquakes. *J. Geophys.Res.* 91, B2, 2095-2112.

Boore D.M., Joyner W.B., 1997, Site amplifications for generic rock sites. *Bull. Seismol. Soc. Am.* 87, 2, 327-341.

Böse E., Villafaña A., García y García J., 1908, El temblor del 14 de abril de 1907. *Parergones del Instituto Geológico de México* II, 4, 5, 6, 135-258.

Brune J.N., 1996, Particle motions in a physical model of shallow angle thrust faulting. *Proceedings of the Indian Academy of Sciences-Earth and Planetary Sciences* 105, 2, 197-206.

Cavalié O., Pathier E., Radiguet M., Vergnolle M., Cotte N., Walpersdorf A., Kostoglodov V., Cotton F., 2013, Slow slip event in the Mexican subduction zone: Evidence of shallower slip in the Guerrero seismic gap for the 2006 event revealed by the joint inversion of InSAR and GPS data. *Earth Planet. Sc. Lett.* 367, 52–60.

Chen T., Lapusta N., 2009, Scaling of small repeating earthquakes explained by interaction of seismic and aseismic slip in a rate and state fault model. *J. Geophys. Res.,* 114, B01311.

Duputel Z., Tsai V.C., Rivera L., Kanamori H., 2013, Using centroid time-delays to characterize source durations and identify earthquakes with unique characteristics. *Earth Planet. Sc. Lett.* 374, 92-100, DOI 10.1016/j.epsl.2013.05.024.

Figueroa J., 1970, Catalogo de sismos ocurridos en la República Mexicana. Report No. 272, Instituto de Ingeniería, U.N.A.M., México.

García Acosta V., Suárez Reynoso G., 1996, *Los sismos en la historia de México*, tomo I. UNAM-CIESAS-Fondo de Cultura Económica, México, 718.

Gutenberg B., 1956, Great earthquakes 1896-1903.*Transactions, American Geophysical Union,* 37, 608-614.

Gutenberg B., Richter C.F., 1954, *Seismicity of the Earth and Associated Phenomena*, 2nd edition, Princeton University Press, Princeton, New Jersey, 310 pp.

Husker A., Davis P.M., 2009, Tomography and thermal state of the Cocos plate subduction beneath Mexico City. *J. Geophys. Res.,* 114, B04306 doi: 10.1029/2008JB006039.

Iglesias A., Singh S.K., Pacheco J.F., Alcántara L., Ortiz M., Ordaz M., 2003, Near-trench Mexican earthquakes have anomalously low peak accelerations. *Bull. Seism. Soc. Am.* 93, 2, 953–959,

Iglesias A., Singh S.K., Lowry A.R., Santoyo M., Kostoglodov V., Larson K.M., Franco-Sánchez S.I., 2004,The silent earthquake of 2002 in the Guerrero seismic gap, Mexico (Mw=7.6): Inversion of slip on the plate interface and some implications. *Geofísica Internacional,* 43, 3, 309-317.

Ji C., Wald D.J., Helmberger D.V., 2002a, Source description of the 1999 Hector Mine, California, earthquake, Part I: Wavelet domain inversion theory and resolution analysis. *Bull. Seismol. Soc. Am.,* 92, 1192-1207.

Ji C., Wald D.J., Helmberger D.V., 2002b, Source description of the 1999 Hector Mine, California, earthquake, Part II: Complexity of slip history. *Bull. Seismol. Soc. Am.* 92, 1208-1226.

Kaneko Y., Avouac J.P., Lapusta N., 2010, Towards inferring earthquake patterns from geodetic observations of interseismic coupling. *Nature Geoscience,* 3, 363-369.

Kim Y., Clayton R.W., Jackson J.M., 2010, Geometry and seismic properties of the subducting Cocos plate in central Mexico. *J. Geophys. Res.,* 115, B06310, doi:10.1029/2009JB006942.

Kostoglodov V., Singh S.K., Santiago J.A., Larson K.M., Lowry A.R., Bilham R., 2003, A large silent earthquake in the Guerrero seismic gap, Mexico. *Geophys. Res. Lett*., 15, doi:10.1029/2003GL017219.

Kostoglodov V., Husker A., Shapiro N.M., Payero J.S., Campillo M., Cotte N., Clayton R., 2010, The 2006 slow slip event and nonvolcanic tremor in the Mexican subduction zone. *Geophys. Res. Lett*. 37, doi: 10.1029/2010GL045424.

Lapusta N., Rice J., Ben-Zion Y., Zheng G., 2000, Elastodynamic analysis for slow tectonic loading with spontaneous rupture episodes on faults with rate- and state-dependent friction. *J. Geophys. Res.,* 105, 23765–23789.

Liu Y., Rice J.R., 2007, Spontaneous and triggered aseismic deformation transients in a subduction fault model. *J. Geophys. Res.* 112, B09404, doi:10.1029/2007JB004930.

Lowry A.R., Larson K.M., Kostoglodov V., Bilham R., 2001, Transient fault slip in Guerrero, southern Mexico. *Geophys. Res. Lett.* 28, 3753– 3756.

Muñoz Lumbier M., 1935, Geografía sísmica (con aplicaciones a la República Mexicana). Contribución a la carta mundial de calamidades. Talleres Gráficos de la Nación, Secretaría de la economía Nacional, México.

Noda H., Lapusta N., 2013, Stable creeping fault segments can become destructive as a result of dynamic weakening. *Nature* 493, 518–521, doi:10.1038/nature11703.

Okada Y., 1992, Internal deformation due to shear and tensile faults in a half-space. *Bull. Seismol. Soc. Am.* 82, 2, 1018-1040.

Ortiz M., Singh S.K., Kostoglodov V., Pacheco J., 2000, Source areas of the Acapulco-San Marcos, Mexico earthquakes of 1962 (M 7.1; 7.0) and 1957 (M 7.7), as constrained by tsunami and uplift records. *Geofísica Internacional,* 39, 4, 337-348.

Pacheco J.F., Singh S.K., 2010, Seismicity and state of stress in Guerrero segment of the Mexican subduction zone. *J. Geophys. Res.* 115, B01303, doi: 10.1029/2009JB006453.

Pardo M., Suárez G., 1995, Shape of the subducted Rivera and Cocos plates in southern Mexico: seismic and tectonic implications. *J. Geophys. Res.,* 100, B7, 12,357-12,373.

Pérez-Campos, X., and G. C.Beroza (2001), An apparent mechanism dependence of radiated seismic energy. *J. Geophys. Res.* 106, No. B6, 11,127-11,136.

Pérez-Campos X., Singh S.K., Beroza G.C., 2003, Reconciling teleseismic and regional estimates of seismic energy. *Bull. Seismol. Soc. Am.,* 93, 5, 2123-2130.

Pérez-Campos X., Kim Y.H., Husker A., Davis P.M., Clayton R.W., Iglesias A., Pacheco J.F., Singh S.K., Manea V.C., Gurnis M., 2008, Horizontal subduction and truncation of the Cocos Plate beneath central Mexico. *Geophys. Res. Lett.* 35, 18, L18303.

Radiguet M., Cotton F., Vergnolle M., Campillo M., Valette B., Kostoglodov V., Cotte N., 2011, Spatial and temporal evolution of a long term slow slip event: The 2006 Guerrero Slow Slip Event. *Geophys. J. Int.* 184, 2, 816-828.

Radiguet M., Cotton F., Vergnolle M., Campillo M., Walpersdorf A., Cotte N., Kostoglodov V., 2012, Slow slip events and strain

accumulation in the Guerrero gap, Mexico. *J. Geophys. Res.* 117, 4, B04305.

Singh S.K., Dominguez T., Caştro R., Rodriguez M., 1984, P waveform of large, shallow earthquakes along the Mexican subduction zone. *Bull. Seismol.Soc. Am.,* 74, 6, 2135-2156.

Singh S.K., Astiz L., Havskov J., 1981, Seismic gaps and recurrence periods of largeearthquakes along the Mexican subduction zone: A reexamination. *Bull. Seismol. Soc. Am.,* 71, 827-843.

Singh S.K., Ordaz M., 1994, Seismic energy release in Mexican subduction zone earthquakes. *Bull. Seismol. Soc. Am.* 84, 5, 1533-1550.

Singh S.K., Pardo M., 1993, Geometry of the Benioff zone and state of stress in the overriding plate in central Mexico. *Geophys. Res. Lett.* 20, 14, 1483-1486.

Singh S.K., Pérez-Campos X., Iglesias A., Melgar D., 2012, A method for rapid estimation of moment magnitude for early tsunami warning based on coastal GPS networks. *Seismol. Res. Lett.,* 83, 3, 516-530.

Singh S.K., Suárez G., Domínguez T., 1985, The Oaxaca, Mexico, earthquake of 1931: lithospheric normal faulting in the subducted Cocos plate. *Nature,* 317, 6032, 56-58.

Song T.-R.A., Helmberger D.V., Brudzinski M.R., Clayton R.W., Davis P., Pérez-Campos X., Singh S.K., 2009, Subducting slab ultra-slow velocity layer coincident with silent earthquakes in southern Mexico. *Science* 324, 5926, 502-506.

Suárez G., Monfret T., Wittlinger G., David C. 1990, Geometry of subduction and depth of the seismogenic zone in the Guerrero gap, Mexico. *Nature,* 345, 6273, 336-338.

UNAM Seismology Group, 1986, The September 1985 Michoacan earthquakes: Aftershock distribution and history of rupture. *Geophys. Res. Lett.,* 13, 573-576.

Valdés-González C., Novelo-Casanova D.A., 1998, The western Guerrero, Mexico, seismogenic zone from the microseismicity associated to the 1979 Petatlan and 1985 Zihuatanejo earthquakes. *Tectonophysics,* 287, 271-277.

Yoshioka S., Mikumo T., Kostoglodov V., Larson K.M., Lowry A.R., Singh S.K., 2004, Interplate coupling and a recent aseismic slow slip event in the Guerrero seismic gap of the Mexican subduction zone, as deduced from GPS data inversion using a Bayesian information criterion. *Phys. Earth. Planet. Interiors,* 146, 3, 513-530.

## Appendix A

### Notes on large earthquakes in Guerrero, 1989-1911

Seven large earthquakes occurred along the Guerrero segment of the Mexican subduction zone between 1899 and 1911. Location and magnitude of these events reported in different catalogs differ significantly. Here we very briefly summarize some relevant information regarding each of these events and give our preferred location and magnitude in Table A1. Unless otherwise mentioned, our preferred surface-wave magnitude, $M_S$, is the one listed in the catalog of large shallow earthquakes of Abe and Noguchi (1983) who reevaluated $M_S$ of earthquakes for the period 1899-1912. This catalog is based on calibration of undamped Milne seismographs and original worksheets of Gutenberg and Richter (see Abe and Noguchi, 1983 for details). Anderson *et al*. (1989) estimated seismic moment of large earthquakes in the period 1907-1957 from Wiechert seismograms recorded at Uppsala. Table A1 also lists moment magnitude, $M_w$, if available. The felt and damage reports, with emphasis on the coastal areas, are very briefly mentioned below. These are extracted from García Acosta and Suárez Reynoso (1996) who provide an exhaustive description of earthquakes in Mexico. Our preferred locations are subjective, relying mostly upon the description of damage and felt reports.

*14 January 1899, 23:43.* The earthquake was strongly felt in the entire state of Guerrero. It was very strongly felt in Tecpan, destroying 33 houses, prefecture, city hall, and schools. It was also felt very strongly in Zihuatanejo where the sea inundated the coast by 35 m. Based on limited intensity data, Singh *et al*. (1981) had previously assigned the event an epicenter of 17.1 ºN, 100.5 ºW and a magnitude of 7.9. Gutenberg (1956) reported the location as 17 ºN, 98 ºW (with estimated limit of error of ± 5º) and a unified magnitude *m* of 7.8. $M_S$ listed in the catalog of Abe and Noguchi (1983) is 7.5, which, as mentioned earlier, is our preferred magnitude. Since the epicenter of 17.1 ºN, 100.5 ºW (Singh *et al*., 1981) is consistent with the extensivedamage reports compiled by García Acosta and Suárez Reynoso (1996); we think that this location is reasonably accurate.

*15 April 1907, 06:08*. An excellent, detailed study on this earthquake was published by Böse *et al*. (1908).The earthquake was felt over an extensive area of the republic. It caused severe damage in many towns of Guerrero, especially in Acapulco, San Marcos, Chilapa, and Chilpancingo. The sea inundated the coast in Acapulco. The epicenter listed in Gutenberg and Richter (1954) is 17 ºN, 100 ºW. The epicentral zone outlined by Böse *et al*. (1908) is consistent with the epicenter of 16.7 ºN, 99.2 ºW reported by Figueroa (1970). This is also our preferred location. Our preferred $M_S$ is 7.7 reported by Abe and Noguchi (1983). $M_w$ of this earthquake, estimated by Anderson *et al*. (1989), is 7.9.

*26 March 1908, 23:03*. Extensive damage was reported along coastal towns of Ometepec and Pinotepa Nacional, near the border of the States of Guerrero and Oaxaca.It was also felt strongly in San Marcos and Acapulco, and inland towns of Tierra Colorada, Chilapa, Tlapa, Ayutla, and Chilpancingo. There is no mention of tsunami in Acapulco. Gutenberg and Richter (1954) reported a depth of 80 km, an epicenter at 18 ºN, 99 ºW, and magnitude *M* of 7.8. Abe (1981) estimated $m_B$7.7. The depth and location, if true, suggest an intraslab earthquake. However, seismograms of this earthquake at Uppsala and Göettingen are similar to other Mexican interplate events and bear no resemblance with those of known intraslab Mexican earthquakes (e.g., 1931 Oaxaca earthquake, see Singh *et al*., 1985). We conclude that this earthquake was a shallow thrust event located SE of Acapulco. Our preferred epicenter is 16.3 ºN, 98.5 ºW. $M_S$ and $M_w$, estimated from European Wiechert seismograms, are7.6 and 7.5, respectively (see Singh *et al*., 1984; Anderson *et al*., 1989).

*27 March 1908, 03:45*. Felt and damage reports suggest that it was an aftershock of the 26 March 1908 earthquake. It is difficult to estimate whether its epicenter was to NW or SE of the mainshock. We arbitrarily assign the same location as the mainshock: 16.3 ºN, 98.5 ºW. $M_S$7.0, $M_w$7.2.

*30 July 1909, 10:51*. Very strong earthquake felt in Acapulco, Chilpancingo, and Chilapa, causing damage and injuries. In Acapulco the earthquake was accompanied by sound. One report mentions that the sea retreated about 50 m. According to Muñoz Lumbier (1935), however, the sea invaded the land in Acapulco,i.e., the land subsided. As described by Muñoz Lumbier (1935), the sea had still not returned to the pre-earthquake level by 1935. If so, then it suggests that the slip on the plate interface probably did not extend farther inland than ~ 10 km from the coast. We note that during 11 May and 19 May 1962 earthquakes ($M_S$ 6.9, 6.7) the tide gauge record in Acapulco shows an uplift of the coast. Gutenberg and Richter (1954) reported the epicenter location as

17.0 ºN, 100.5 ºW and $M_{GR} = 7^3/_4$.The epicenter listed in Figueroa (1970) is 16.8 ºN, 99.9 ºW, near Acapulco, which agree well with felt and damage reports and, hence, is our preferred location. $M_S$7.3, $M_w$7.5.

*31 July 1909, 19:18*. Strongly felt in Acapulco causing some damage. Reports mention that the sea receded 30 m. Most probably a large aftershock of the earthquake of the day before. The location given by Figueroa (1970) is 16.6 ºN, 99.5 ºW. We assign it the same epicenter as the earthquake of 30 Jul. 1909: 16.8 ºN, 99.9 ºW. $M_S$6.9, $M_w$7.0.

*16 December 1911, 19:14*. Felt strongly in Acapulco, Tecpan de Galeana and San Luis de la Loma. Epicenter listed in Gutenberg and Richter (1954) is 17.0 ºN, 100.5 ºW with $M_{GR}$7.5. The location given by Figueroa (1970) is 16.9 ºN, 100.7 ºW. Our preferred epicenter is 17.1 ºN, 100.7 ºW. $M_S$7.6, $M_w$7.6.

**Table A1.** Large, shallow earthquakes between 1899 and 1911 in the Guerrero segment of the Mexican subduction zone. A is the amplitude of ground motion in micron during 20 s surface waves at Uppsala.

| Yr Mo Day | Hr | Location | | Magnitude | *A*, Uppsala |
|---|---|---|---|---|---|
| | | Lat.,ºN | Lon., ºW | | *μ* |
| 1899 01 24 | 23:43 | 17.1 | 100.5 | 7.5 ($M_S$) | - |
| 1907 04 15 | 06:08 | 16.7 | 99.2 | 7.7 ($M_S$)<br>7.9 ($M_w$) | 283 |
| 1908 03 26 | 23:03 | 16.3 | 98.5 | 7.6 ($M_S$)<br>7.5 ($M_w$) | 259 |
| 1908 03 27 | 03:45 | 16.3 | 98.5 | 7.0 ($M_S$)<br>7.2 ($M_w$) | 66 |
| 1909 07 30 | 10:51 | 16.8 | 99.9 | 7.3 ($M_S$)<br>7.5 ($M_w$) | 120 |
| 1909 07 31 | 19:18 | 16.8 | 99.9 | 6.9 ($M_S$)<br>7.0 ($M_w$) | 26 |
| 1911 12 16 | 19:14 | 17.1 | 100.7 | 7.6 ($M_S$)<br>7.6 ($M_w$) | - |